On-Chip UV/VIS Optical Spectrometer

by

Tuba Sarwar

A dissertation submitted in partial fulfillment
of the requirements for the degree of
Doctor of Philosophy
(Electrical and Computer Engineering)
in the University of Michigan
2023

Doctoral Committee:

Professor Pei-Cheng Ku, Chair
Professor Jeffrey A. Fessler
Professor Zetian Mi
Assistant Professor Qing Qu
Professor Max Shtein
Associate Professor Zhaohui Zhong

Tuba Sarwar

tsarwar@umich.edu

ORCID iD: 0000-0002-6110-882X

Dedication

This dissertation is dedicated to my loved ones:

- my parents, whose enduring support enabled me to accomplish this endeavor,
- my husband, who kept my spirits and motivation high,
- my elfish but adorable child, Rayyan, whose love and warmth made my journey easier.

Acknowledgements

I would like to express gratitude to all the people, whose phenomenal support has steered me through my Ph.D. experience. Without the generous support, encouragement, and assistance of these unsung heroes, this endeavor would not have been possible. I am extremely grateful to my advisor, Professor Pei-Cheng Ku for his wisdom, persistence, optimism, and unlimited support throughout my Ph.D. His invaluable advice and insight have carried me through all the stages of completing this dissertation. The meetings, discussions, and all the conversations we had, were vital in stimulating me to think outside the box. His insight allowed me to view problems from multiple perspectives. He provided a positive work environment to grow as a scientist and offered innumerable collaboration opportunities to work with the interdisciplinary group. These experiences enriched me professionally. Thank you Professor for giving me the opportunity in the first place to pursue my Ph.D. at the University of Michigan where I learned so much and met so many incredible people.

I would also like to extend my heartfelt thanks to my dissertation committee members, Professors Zetian Mi, Jeffery A. Fessler, Max Shtein, Zhaohui Zhong, and Qing Qu for their constructive comments, and insightful feedback on this thesis. My deepest appreciations particularly go to Professor Qing Qu and his group for their collaborative support, especially, Can Yaras, Pengyu Li, and Xiang Li with whom I have worked so closely on the machine learning part of this project. I am grateful to Professors Zetian Mi and Pallab Bhattacharya for teaching me the principles of optoelectronics, which lays essential foundations of this dissertation, and for helping me build my confidence. I would like to acknowledge the generous support of the Punjab

Endowment Education Fund for providing me partial funding to aid my studies and for letting me be a part of this wonderful wolverine community. I would also like to acknowledge with much appreciation the crucial role of the facilities and staff of the Lurie Nanofabrication Facility at the University of Michigan for smooth running of my research and their active help and co-operation whenever needed.

My sincere gratitude also goes to my lab mates for their support, scientific insights, and stimulating discussions. Thank you, Juhyeon Kim, for teaching and helping me with the MIT Electromagnetic Equation Propagation software (MEEP) simulations. I appreciate all your input and suggestions on this part. Thank you Nathan Dvořák for being my coffee mate and a supportive colleague. I will always cherish the time we spent together. I must reserve a special thanks to former postdoctoral researcher Dr. Kunook Chung for providing his thoughtful advice and suggestions on fabrication part throughout my research work

Last, but not least, I would like to thank my family for encouraging me to chase my dreams. I could never have achieved anything in life without the unconditional love, care, and tolerance of my parents, and siblings through every stage of my life. I am greatly indebted to my husband for always being supportive of my career goals. He has been actively involved in my research from my first day here and provided his insightful technical knowledge, suggestions, and expertise on the fabrication process of this work. Without his tremendous understanding, encouragement, moral and emotional support, this project would not have been the same. My warmest thanks go to my son Rayyan for being the pillar of support & putting up with me being in the office, lab, or studying at home, ignoring his requests to spend time with him. Thanks for never complaining and for being so mature for your age understanding that this was for our better future. You have been amazing and I will now give you my laptop as I promised.

Table of Contents

List of Figures

List of Appendices

APPENDIX

Abstract

Optical spectroscopy is one of the most widely used analytical techniques in science and engineering. Miniaturizing an optical spectrometer can allow for a portable and handheld system and lead to new opportunities for the Internet of Things (IoT) and lab-on-a-chip applications. Visible-light spectrometers have broad applications in UV-VIS, fluorescence, and chemi-/electro-luminescence spectroscopy. A spectrometer is a highly complex system consisting of optical, mechanical, and image processing units. Miniaturizing such a system is a nontrivial task involving the ability to integrate multiple material platforms and careful planning of performance tradeoffs, such as spectral resolution, sensitivity, system size, and cost. Among various approaches, spectrometers based on reconstructive algorithms shift the complexity of processing spectral information from physical components to software computations. With the steady growth of computational power per watt-dollar, this approach has become increasingly promising in constructing an extremely compact spectroscopic system.

In this work, a low-profile reconstructive spectrometer with only the thickness of the semiconductors and an operating range spanning the visible wavelength spectrum is reported. This spectrometer concept is based on wavelength-selective semiconductor photodiodes monolithically integrated on a chip area of 0.16 mm^2. The absorption properties of individual photodiodes were tuned via local strain engineering in compressively strained Indium Gallium Nitride/Gallium Nitride (InGaN/GaN) multiple quantum well heterostructures. By varying the diameters of individual nanopillars, the cutoff wavelengths of absorption were varied across the chip. The

intrinsic wavelength selectivity is insensitive to the incident angle of light. The built-in GaN pn junction enabled a direct photocurrent measurement.

In this dissertation, we first proposed and demonstrated a proof-of-concept spectrometer based on 14 photodiodes, without any external optics or spectral filtering components, in the wavelength range of 450 – 590 nm. Using a non-negative least square (NNLS) algorithm enhanced by orthogonal matching pursuit (OMP), the spectrum of a test light source was reconstructed.

Secondly, we monolithically integrated a GaN-based LED with the spectroscopic chip. An optical blocking structure was used to suppress the LED-photodetector interference and was shown to be essential for spectroscopic functionality. A proof of concept using a reflection spectroscopy configuration was experimentally conducted to validate the feasibility of simultaneously operating the LED excitation light source and the photodiodes. Spectral reconstruction using an NNLS algorithm enhanced with OMP was shown to reconstruct the signal from the reflection spectroscopy. No external optics, such as collimation optics and apertures were used.

Thirdly, we discussed the spectrometer design conditions enabling an ultrathin form factor to increase the light-harvesting efficiency. We proposed and demonstrated a simple strategy, utilizing the well-established sapphire substrate patterning process to greatly enhance the absorption efficiency while maintaining a large acceptance angle for the incident light. We also demonstrate that spectroscopic performance can be significantly enhanced with this strategy.

Finally, we demonstrated a reconstructive spectrometer consisting of 16 spectral encoders to deliver a decent spectral reconstruction performance in the wavelength range of 400 – 650 nm. The accuracies of spectral peak positions and intensity ratios between peaks were found to be 0.97% and 10.4%, respectively. No external optics such as collimation optics and apertures were used, enabled by angle-insensitive light-harvesting structures, including an array of cone-shaped

back-reflector fabricated on the underside of the sapphire substrate. The small chip area and a computationally efficient spectral reconstruction algorithm make the proposed spectrometer especially suitable for wearable applications.

Chapter 1 Introduction

1.1 Introduction to Spectroscopy

Optical spectroscopy is one of the most important and widely utilized scientific techniques. A spectrometer measures an optical signal's spectrum, i.e., the relative power spectral density $P(\lambda)$ at different wavelengths λ. The spectral analysis of the light that is transmitted, emitted, reflected, or absorbed by a material or structure provides signature information about its physical and chemical properties [1,2]. For example, in chemical analysis, the composition and concentration of a sample solution are measured from the absorbed light by the solution [3,4]. Similarly, the thickness of a thin film can be determined by investigating the light reflected from it [5]. With impressive performance to characterize a versatile range of samples precisely, optical spectrometers have found many applications in almost every branch of science and technology. These applications have important impacts in the fields of physics, chemistry, biomedicine, food engineering, environmental monitoring, quality control, and the life sciences [6–14].

1.2 Spectroscopic System Configuration

A conventional optical spectrometer typically consists of the following key elements [15]:

1. A light source to emit electromagnetic radiation.
2. An entrance slit through which light enters the spectrometer. This narrow slit determines the amount of light that can be measured by the spectrometer.
3. Collimated optics to produce a collimated light beam.

4. A dispersive optical element (DOE) to resolve the power of input light at different wavelengths.
5. A focusing mechanism to focus the dispersed light onto the plane of the detector.
6. One or more detectors to measure the intensity of light. Exit slit can be eliminated if a linear photodetector array is used.
7. An area to allow free-space light propagation. Dispersion of the spectral components at the photodetector plane depends on the distance light is allowed to travel after deflecting from the dispersive element. This free space also maintains required optical path lengths in between the collimated and focusing optics to condition the optical signal of the incident and refracted light beam. Optical path length helps to control the interference and diffraction of light as it propagates.

Generally, spectrometers are categorized based on their underlying operating mechanisms such as diffraction, interference, or Fourier transform. Figure 1-1 shows a schematic of a traditional spectroscopic system in which a diffraction grating is used to separate different light bands by different angles. A set of focusing optical elements focuses the light coming from all directions at specified wavelengths. Sometimes, an exit slit is also used to project a small portion of spectrum on one detector element at a time, such as in the Czerny−Turner monochromator configuration [16]. A mechanical scanning setup is thus needed to rotate the grating and acquire the full range of spectral lines. Such a system has a large footprint to accommodate the collimation and focusing optics.

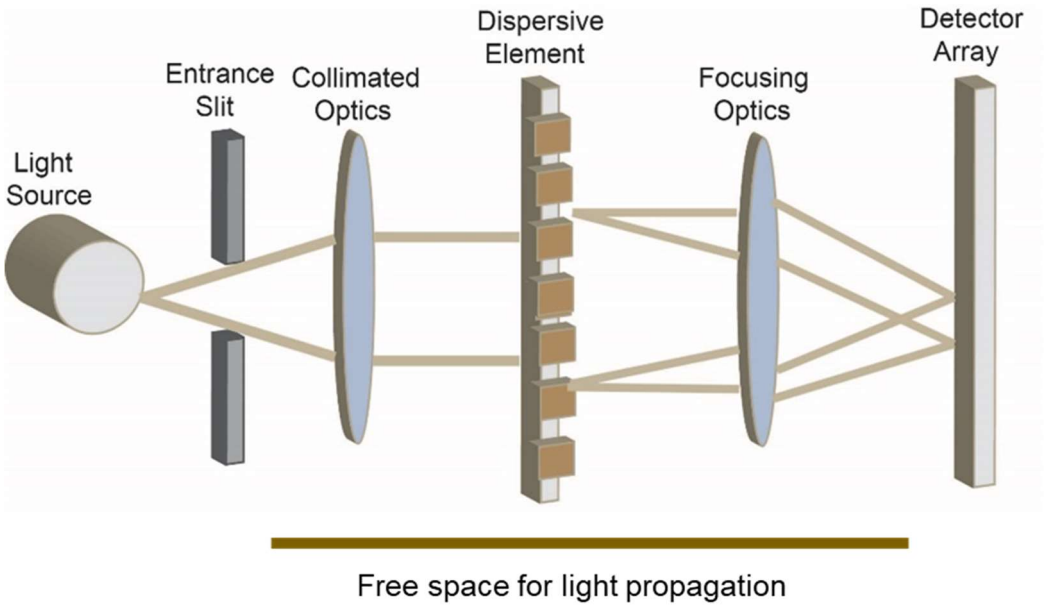

Figure 1-1: Configuration of a standard optical spectrometer consisting of a dispersive optical element, detector array, collimation, and focusing optics. A single detector can also be used if the dispersive optical element is installed on a motorized rotation stage.

In addition, the Czerny−Turner monochromator's spectral resolution generally increases with a larger system size to establish sufficient optical path differences between two wavelengths. This type of spectrometer requires a precise alignment of various optical paths [17,18]. The complex alignment of sensitive optical parts adds sophistication to these benchtop spectrometer systems and restricts their use only in laboratories with test site settings. But once aligned, it can achieve excellent performance in terms of spectral resolution and sensitivity.

1.3 Miniaturization of Spectroscopic Systems-Motivation of this Work

One area that is of great interest in recent years is miniaturized, low-cost, and easy-to-use spectrometers. The reduced footprint of spectrometers can enable their use for wearable and

mobile applications, which are highly desirable in the field of biochemical sensing, health diagnostics, cosmetics industry, planetary exploration, quality control, machine vision, agriculture, internet of things, surveillance, and lab-on-a-chip (LoC) systems [19–28].

A spectrometer is a highly complex system consisting of optical, mechanical, and image processing units. Miniaturizing such a system is a nontrivial task involving the ability to integrate multiple material platforms and careful planning of performance tradeoffs, such as spectral resolution, sensitivity, system size, and cost. Among various approaches, spectrometers based on reconstructive algorithms shift the complexity of processing spectral information from physical components to software computations [29,30,39–48,31–38]. With the advantage of more readily accessible computer processing power and reduced microprocessor size and cost, this approach has emerged as a new paradigm.

A miniaturized spectrometer can be implemented using either a tunable laser plus a broadband detector or a broadband source (which can be ambient light) plus an array of wavelength-selective detectors. The latter is often realized with a combination of wavelength-discrimination optics and a wavelength-insensitive sensor array. To miniaturize the spectrometer, the optical grating in Figure 1-1 is substituted by an array of spectral filters as shown in Figure 1-2, either dispersive or absorptive for wavelength discrimination [45,49–52]. Dispersive filters rely on optical interference due to optical path length differences at different wavelengths, while absorptive filters utilize materials with different light absorption properties. Examples of miniaturized dispersive filters include Fabry-Perot cavities [53–55], microcavities [40,56,57], photonic crystals [42], Michelson interferometer [58], and random media [59,60]. Dispersive filters generally exhibit a strong sensitivity to the incident angle of light [35], which requires collimation optics, e.g., an aperture plus a lens, and adds to the system's bulk.

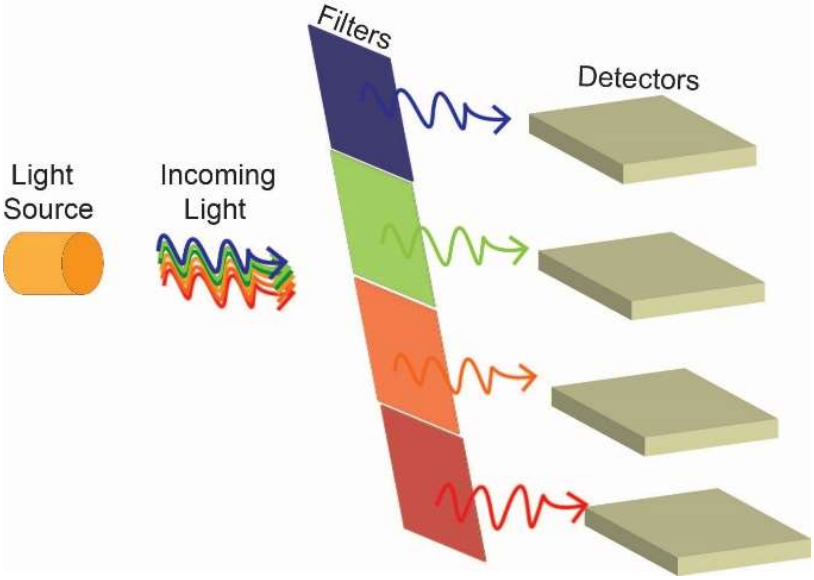

Figure 1-2: A miniaturized optical spectrometer based on multiple spectral filters and broadband photodetectors. The spectral filters provide the wavelength-selective filtering mechanism to resolve an incoming broadband spectrum at specific wavelengths. The broadband detector detects the filtered signal.

Absorptive filters can overcome these issues using materials with different spectral absorption properties, but an approach compatible with scalable manufacturing is crucial for miniaturization [41,61].

1.4 Reconstructive Optical Spectrometers

In recent years, optical spectrometers based on reconstructive computational techniques have become increasingly promising in realizing an extremely compact spectroscopic system. The major challenges lie in the spectral reconstruction with a limited number of encoders/photodetectors, which result in challenging estimation problems. Recent developments in advanced signal processing and machine learning techniques have made it possible to realize

miniaturization in the true sense. The reconstructive spectrometer encodes the signal with multiple broadband spectral filters having different spectral response characteristics. The reconstructive spectrometer has attracted intense research interest recently [29,30,64–66,40–42,44,55,61–63] because

1. Computational power per watt-dollar grows rapidly;

2. Spectral filters can be highly compact and mass-produced;

3. With machine learning and optimization advances, the spectrum can be efficiently reconstructed even with only a small number of encoders/photodetectors.[33,66,67]. These features are especially attractive when miniaturizing a spectroscopic system.

1.4.1 Principle of Spectral Reconstruction

Mathematically, an optical spectrometer transforms an incident optical spectrum into a photodetector response through a responsivity matrix as shown in Figure 1-3. Consider i photodetectors with known spectral response function $R_i(\lambda_j)$ at j wavelengths. For an unknown incident spectrum $S_j(\lambda)$, the photocurrent I_{pi} generated by the photodetectors can be described as the linear transformation by:

$$\begin{bmatrix} I_{p1} \\ I_{p2} \\ \vdots \\ \vdots \\ I_{pi} \end{bmatrix} = \begin{bmatrix} \begin{bmatrix} R_{1,1} & R_{1,2} & \dots & \dots & R_{1,j} \\ R_{1,2} & R_{2,2} & \cdots & \dots & R_{2,j} \\ \vdots & \vdots & \ddots & \ddots & \vdots \\ \vdots & \vdots & \ddots & \ddots & \vdots \\ R_{j,1} & R_{j,2} & \cdots & \dots & R_{j,j} \end{bmatrix} \times \begin{bmatrix} S_1 \\ S_2 \\ \vdots \\ \vdots \\ S_j \end{bmatrix} \end{bmatrix}. \tag{1-1}$$

Reconstruction here refers to the solution of linear equation system as described in Equation (1-1). This equation can be uniquely solved for the unknown incident spectrum $S_j'(\lambda)$, only if $i \geq j$, which allows one-to-one mapping between the photodetector response and the spectral values. However, mapping one wavelength to a specific detector is not possible when

decreasing the spectrometer footprint. For example, in a classical spectrometer, the response function matrix has only diagonal entries which permits different wavelengths j to be focused on different photodetectors i. However, in real and practical applications, any full-rank and well-conditioned matrix can be employed as the response function. On the other hand, the system also encapsulates the noise present in the output signal. Hence, instead of the model (1-1), in the presence of noise, we use the more complete signal plus noise model:

$$\begin{bmatrix} \mathrm{I_{p1}} \\ \mathrm{I_{p2}} \\ \vdots \\ \vdots \\ \mathrm{I_{pi}} \end{bmatrix} = \begin{bmatrix} \begin{bmatrix} \mathrm{R_{1,1}} & \mathrm{R_{1,2}} & \dots & \dots & \mathrm{R_{1,j}} \\ \mathrm{R_{1,2}} & \mathrm{R_{2,2}} & \cdots & \dots & \mathrm{R_{2,j}} \\ \vdots & \vdots & \ddots & \ddots & \vdots \\ \vdots & \vdots & \ddots & \ddots & \vdots \\ \mathrm{R_{j,1}} & \mathrm{R_{j,2}} & \cdots & \dots & \mathrm{R_{j,j}} \end{bmatrix} \times \begin{bmatrix} \mathrm{S_1} \\ \mathrm{S_2} \\ \vdots \\ \vdots \\ \mathrm{S_j} \end{bmatrix} \end{bmatrix} + \begin{bmatrix} I_{n1} \\ I_{n2} \\ \vdots \\ \vdots \\ I_{ni} \end{bmatrix}. \tag{1-2}$$

This makes the problem critical specifically for on-chip implementation. Inside the chip, the propagation of light in undesired directions can lead to noise. Both stray and scattered light can contribute as noise to the responsivity matrix.

Equation (1-1) can be discretized as:

$$\mathrm{I_p} = \mathrm{R} \times \mathrm{S}. \tag{1-3}$$

The spectrum can be solved by inverting Equation (1-3) as:

$$\mathrm{S} = (\mathrm{R^T R})^{-1} \mathrm{R^T} \times \mathrm{I_p}. \tag{1-4}$$

While evaluating the unknown spectrum using an inverse of the responsivity matrix as in Equation (1-4), the resultant spectrum can be comprised of large positive and negative spikes due to two reasons. 1. The noise in the measurements, 2. Equation (1-3) is an underdetermined system that can have an infinite number of solutions. This noisy solution can still mathematically lead to a finite photodetector response [68–70].

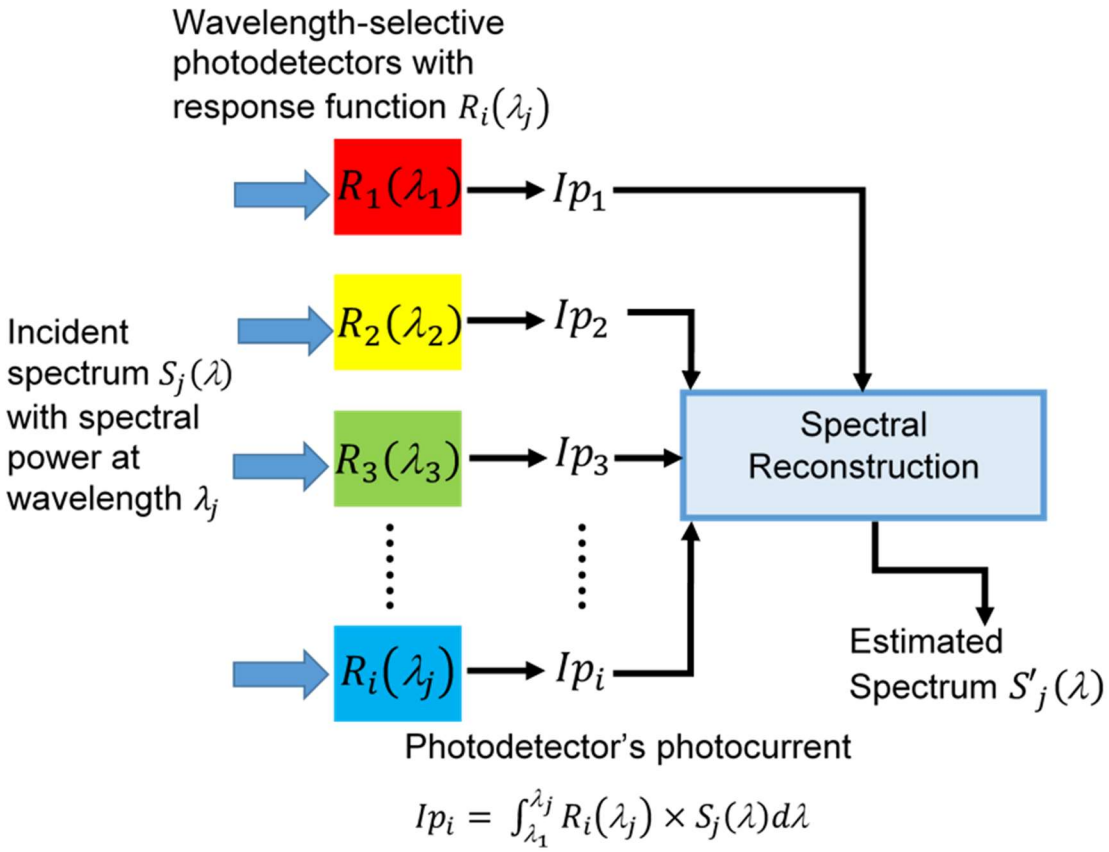

Figure 1-3: Mathematical Model of a spectroscopic system comprising of wavelength-selective photodetectors with tailored spectral response. The model represents an underdetermined system where the number of photodetectors is smaller than the number of spectral values in the reconstructed spectrum.

For a robust and accurate estimation of the spectrum, proper computation schemes need to be employed to solve an underdetermined system with $i < j$, as illustrated in Figure 1-3. In this case, additional information based on the prior knowledge of spectrum can be incorporated to estimate the most reasonable solution [71].

The randomness of different photodetectors' responsivities is also important in finding a plausible solution while reconstructing a spectrum. If the responses of two photodetectors are

indistinguishable for two different wavelengths, it is impossible to determine which wavelength leads to the measured response. Mathematically, the columns of the responsivity matrix $R_{ij}(\lambda)$ in Equation (1-1) should be as dissimilar as possible to achieve an accurate and precise numerical solution. Compressive sensing and machine learning techniques are proven very promising in solving an underdetermined system when the correlation between the response functions is sufficiently small.

The estimation of spectrum is a typical signal-processing problem and many algorithms can be applied to solve the problem. By adopting proper and suitable machine learning methods, better data acquisition processes and efficient reconstruction algorithms are possible, leading to faster and more accurate spectrum recovery with a limited number of encoders/photodetectors. In return, the developed learning methods will provide guidance for the better design of the sensing platform.

1.5 Current State of Knowledge-A Review of Previous Work

Researchers have attempted several approaches to develop different compact designs for chip-scale miniaturized optical spectrometers. This section demonstrates some of the recent developments, the technological aspects of different approaches, their relative merits, and their drawbacks. Based on the mostly explored platforms, miniaturized spectrometers are organized into five different categories that are discussed briefly below:

1.5.1 Spectrometers based on Dispersive Optical Elements

This configuration is based on the integration of nanostructured optical dispersive elements along with detectors on the same platform [8,36,52,72]. Recent developments in micro/nano-fabrication processes have provided the opportunity to scale down the sizes of optical components.

The working principle of such systems is quite similar to a conventional benchtop spectrometer as shown in Figure 1-1. The incident light is allowed to propagate through the device that interacts with several miniaturized DOEs to provide necessary optical path length differences [7,10,73–75]. These optical elements are designed to resolve the light into different wavelengths and disperse it by different angles. The resolved spectral components from all different directions are then focused on different locations of the photodetector array.

For spectrometers based on DOEs, the spectral resolution of the system depends on the optical path length of the system. When the system footprint decreases, the path length also decreases thus dropping the spectral resolution. Different design configurations use different strategies to compensate for this reduction. In one approach, collimated optics is replaced by a concave grating that disperses and focuses light from different angles on to the detector array [6,76–78]. As a result, collimated optics and different reflective components are no longer required and spectral resolution is also enhanced. A schematic illustration of the concave grating-based spectrometer design is shown in Figure 1-4.

In addition to this, some designs utilize a G-Fresnel optical device, which offers an integrated functionality of a diffraction grating with a Fresnel lens as shown in Figure 1-5 [7,79]. Recently, smartphone-based spectrometers have been demonstrated with G-Fresnel optical components and are applied for biochemical investigations [80,81].

In another approach, waveguide gratings are used as the DOEs to couple light inside the system [82–84]. The device is used for chemical and material analysis. When the light propagates through the waveguide, it interacts with the chemical sample. An array of photodetectors is then used to measure the absorption spectrum of the chemical as shown in Figure 1-6.

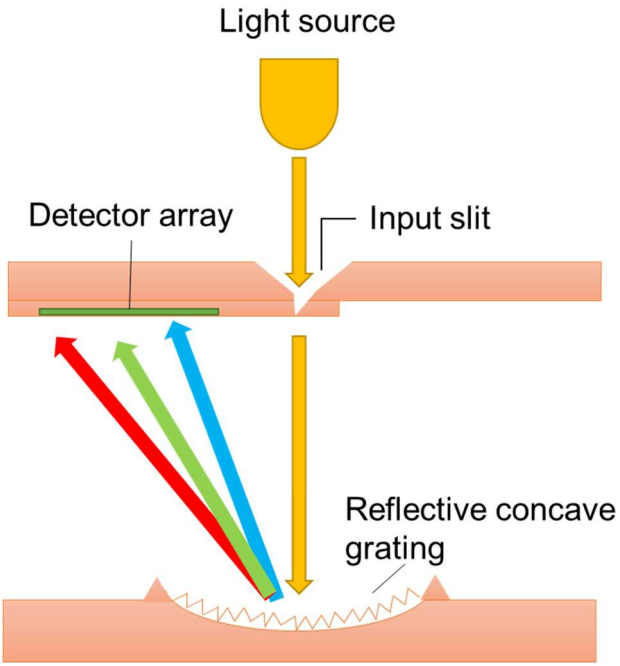

Figure 1-4: Simplified illustration of a spectroscopic system based on a concave diffraction grating.

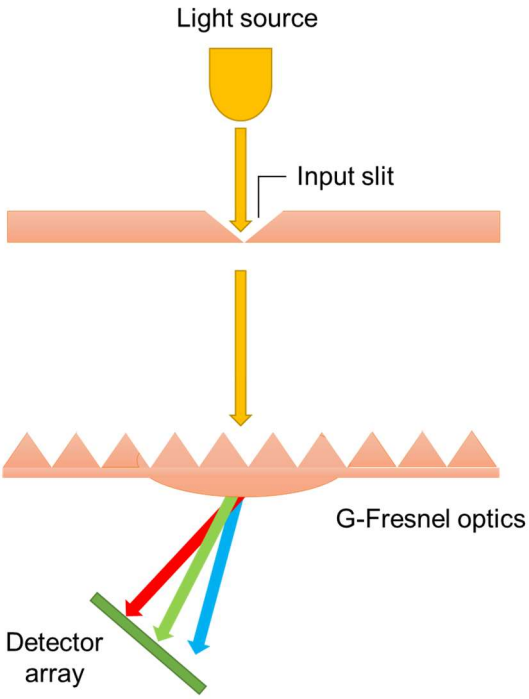

Figure 1-5: Schematic configuration of a spectrometer based on a G-Fresnel optical device.

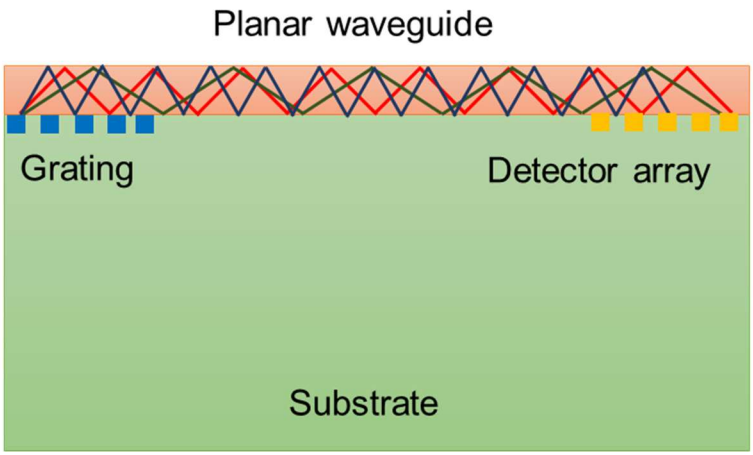

Figure 1-6: Schematic of a waveguide-based spectrometer with a buried grating on a waveguide sensor.

The spectrometers based on DOEs approach provide a fully integrated, on-chip system with reasonable spectral resolution sensitivity and peak detection accuracy. However, these are highly dependent on the incident light angles, light coupling efficiencies, quality of optical components, and system alignment [85].

1.5.2 Fourier-Transform Spectrometers

The Fourier-transform spectrometer (e.g., FTIR) encodes the signal's autocorrelation using a variable delay line which is then converted into the signal's spectrum via the Fourier transform [42,86–94]. Miniaturized FTIR spectrometers are categorized into two types based on the principle by which the interference of the light waves varies over time.

The first spectrometer is the Michelson interferometer, which consists of a beamsplitter, a scanning mirror, a stationary mirror, and a single detector [95–98]. The optical input is divided

into two equal beams with the help of the beamsplitter. One beam is reflected from the fixed mirror whereas the other beam is reflected off the moving mirror. Both reflected beams recombine at the beamsplitter and interfere with each other. A photodetector is used to measure the interferogram of the incoming light. The schematic configuration of Michelson interferometer is shown in Figure 1-7.

The second configuration is based on the Mach-Zehnder interferometers (MZIS) in which the input light is split into at least two unidirectional paths towards a single photodetector where they interfere with each other [99–101]. MZIs spectroscopic systems have found broad applications in integrated waveguides without any movable components.

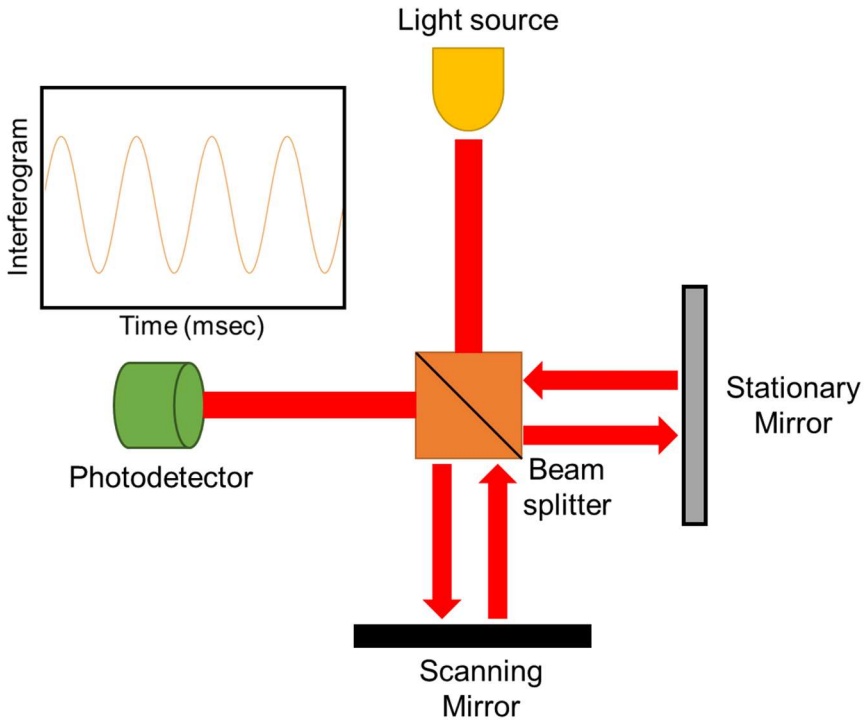

Figure 1-7: Schematic of a Fourier transform spectrometer based on a Michelson interferometer.

The Fourier-transform spectrometer has two key advantages over those based on DOEs.

1. It measures spectrum based on the multiplexing principle i.e. collecting spectrum information at one detector.
2. It prevents spectral dispersion resulting in a higher signal-to-noise ratio.

1.5.3 Fabry-Perot Spectrometers

In basic configuration, the Fabry-Perot device consists of two plane, parallel, highly reflective surfaces (mirrors) spaced by a distance d [102,103]. The device also includes a dielectric resonant cavity in between the reflective surfaces. The working principle is similar to a tunable diffraction grating. The spectrometer operation depends on the optical cavity to transmit a narrow spectral band to the detector. If the cavity length is varied spatially, it works as a variable filter. Excellent resolution can be achieved by properly controlling the cavity length. The spectral transmission of Fabry-Perot filter is controlled by the application of an acoustic signal that isolates the spectral components on the time axis [104–106]. A detector is placed under the resonator cavity, which eliminates the use of focusing optics. The device configuration is shown in Figure 1-8.

In maximum transmission through the cavity, the light with wavelength λ can be resonated and enhanced in the cavity if d becomes an integral multiple of $\lambda/2$. The system resolution depends on high reflectance of both mirrors. Moreover, the imperfection and nonparallelism in the mirrors combined with the cavity defects lead to the reduction of spectral resolution [107]. This approach is also sensitive to the incident light angle of incoming light. As the cavity reflects most of the incoming light, throughput is not good because a large fraction of energy is lost.

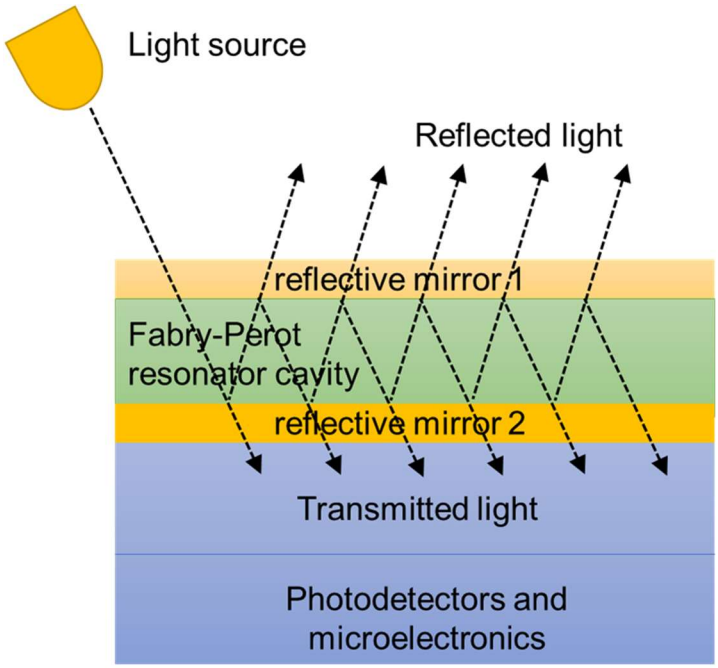

Figure 1-8: Simplified schematic illustrating the principle of a miniaturized Fabry-Perot cavity spectrometer.

1.5.4 Colloidal Quantum Dot - A Reconstructive Spectrometer

This approach is based on colloidal quantum dots (CQD) that are chemically synthesized filters with distinct, broadband transmission spectra [43,61]. The absorption properties of CQD filters are tuned by their sizes, shapes, and composition to allow wavelength selectivity. Broadband light, with its own specific spectrum, passes through the broadband spectral filters and reaches a detector where its intensity is measured. The incident spectrum is generated by implementing spectrum reconstruction techniques. The CQD spectrometer can efficiently reconstruct narrowband spectrums with precision and accuracy. The method has no angular or polarization

dependence. However, this approach involves nonconventional materials and non-standard fabrication processes implying limited feasibility of scalable manufacturing.

1.5.5 Spectrometers based on Dispersive Media/Photonic/Plasmonics Slabs-A Reconstructive Spectrometer

This configuration utilizes random spectral filters based on the photonic crystal (PC) or plasmonic slabs with a specific optical transmission spectrum. A schematic illustration is shown in Figure 1-9. The spectral response of each filter is unique and depends only on the structure and geometry of the slab. The incoming light bounces back and forth many times within the structure. This reduces the cross-correlation of the transmission spectra of each filter and enhances the reconstruction capability. However, the transmission spectra are highly sensitive to the incident angle of incoming light, which may affect the efficacy of the device.

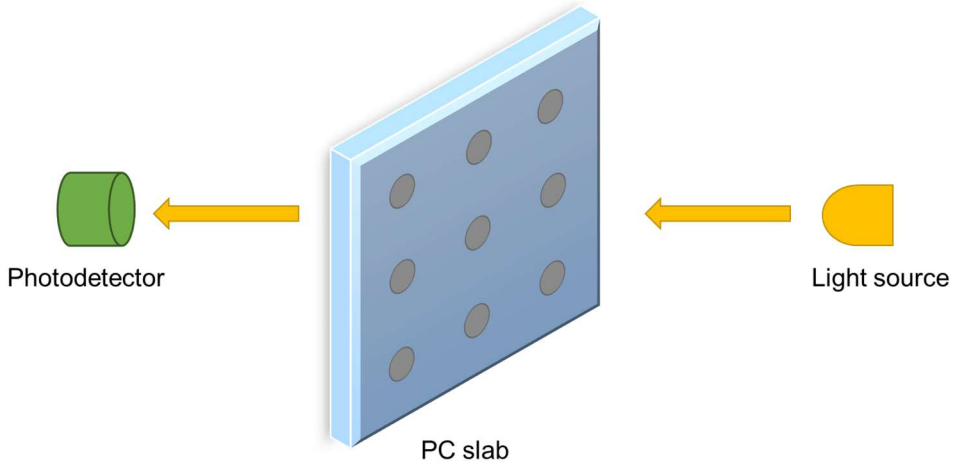

Figure 1-9: Schematic illustration of a photonic crystal (PC) slab optical spectrometer. PC slab filters are comprised of an array of air holes in a dielectric film. The transmission spectra depend on the diameter, array period, and lattice constant of the holes.

1.5.6 Filter-Free Optical Spectrometers based on Reconstructive Algorithms

In this class of spectrometers, instead of separately integrating DOEs with one or more detectors, light filtering occurs within the detectors themselves. In this method, the detector's responsivity is tailored by engineering the bandgap of the material. Each detector has its own response function, which is later used to generate the spectrums using spectral reconstruction techniques. Moreover, the spectrometers based on nanostructured photodetectors e.g. single nanowires [43] or GaN nanopillar arrays [30] have a clear advantage, as wavelength selective photo-detection is inherent to the photodetectors due to which this configuration is insensitive to the incident angle of light. This eliminates the need to condition the incident signal with any collimation optics or aperture, enabling a versatile integration of the spectrometer chip with a lab-on-a-chip sensor. A comparison of different existing spectroscopic approaches categorized by the filter materials is also summed up in Table 1-1.

Table 1-1: Summary of various methods for a miniaturized reconstructive spectrometer.

Design	Filter class	Signal Detection	Pros	Shortcomings
CMOS spectrometer	DOEs based on diffraction, interference, and resonance	Separate photodetector array	• Fully-integrated, optics free • Good spectral peak estimation accuracy • Range: 500 - 830 nm	• Requires an external optical fiber • Sensitive to the coupling conditions. • Resolution depends on system dimensions • Need to condition the incident light
PC slab spectrometer	Passive resonance	CMOS sensor array (involves integration with filters)	• High spectral and spatial resolution • Range: 550 - 750 nm	• A minimum of 36 filters required for decent reconstruction • Highly sensitive to the angle of incidence of the incoming light
CQD spectrometer	Passive absorptive	CCD Camera (assembled separately with filters)	• High-resolution spectrometer • No angular or polarization dependence • Range: 400 – 600 nm	• Accurate spectral reconstruction with at least 196 filters • Non-standard CMOS materials and fabrication processes • Scalable manufacturing is crucial
Single nanowire spectrometer	Active absorptive	Nanowire works as a photodiode with in-built filtering	• On-chip integration of nanostructures with unique responsivities • Doesn't need to condition incident light • Range: 510 – 620 nm	• Reasonable reconstruction with minimum of 30 units • Operational range is just over 100 nm broad and is limited by the band gap of bulk semiconductors
Our Spectrometer_ Strain-engineered semiconductor	Active absorptive	Spectral filtering and sensing in the same structure	• Spectroscopic functionality with only 16 PDs • Ultrathin, optics-free & chip-scale • Insensitive to the incident beam angle • Range: 400 -650 nm	• Needs improvement in the accuracy of intensity ratios between the peaks of reconstructed spectrum

1.6 Spectrometer Figures of Merit

The spectrometer design and its performance depends on several significant characteristics often refers to as the figures of merit of the device. When miniaturizing a spectroscopic system, it is essential to have a thorough understanding of the figures of merit and the trade-offs of the strategies. These characteristics include optical throughput, spectral range, spectral resolution, spectral multiplexing, and noise functioning. In this section, we compare our proposed approach with other spectrometer designs in the light of these key parameters.

Throughput denotes the portion of incoming light accessible for the spectrometer and is available to be analyzed by the system. It is the amount of light that passes through the spectroscopic system and is detected by the detectors. Throughput depends on the area of the aperture. For example, the DOEs based spectrometers use apertures or an entrance slit that limits the amount of input light reaching the detector. In such cases, most of the light is lost and is not available to traverse resulting a poor throughput. Our design approach does not need any aperture or slit, so the throughput is not limited as compared to other spectrometers.

Spectral multiplexing is another important trait of a spectrometer. It is the ability of the device to read multiple wavelengths simultaneously. Some spectroscopic systems such as tunable light spectrometers measure one wavelength at a time. Our spectrometer can encode all spectral information into one measurable optical signal as it uses a large fraction of incident light.

Spectral range is the span of the wavelengths measurable by the spectrometer. The spectral operating range is often limited by the detector's response at different wavelengths and sometimes by the optical components. In a GaN-based spectrometer, the basic building block is GaN nanopillars shaped by etching a standard GaN LED epitaxial stack. The strain relaxation around the nanopillar's perimeter leads to the modulation of the bandgap along the radial direction because

of the piezoelectric effect. This property potentially enables GaN nanopillar structures to continuously cover UV to near-infrared with InN/GaN (GaN/AlN) quantum wells.

The signal-to-noise ratio (SNR) is defined as the optical power divided by the root mean square of the noise. When the optical signal is detected, it generates a current known as photocurrent. Hence, electrical SNR is proportional to the optical power. In this way, SNR is derived from the throughput, spectral multiplexing, and other characteristics.

Another important attribute of a spectrometer is its ability to read and convert the encoded signal into a spectrum. Data readout implicates the output spectral information. Some configurations use multiple detectors, while others need a linear transform of only one detector output to produce a spectrum. In our design, readout detection takes place within the nanopillar itself with light filtering. This eliminates any sort of integration with separate detectors. However, the system still relies on reconstructive computational schemes and requires significant computing power to operate. Depending on the simulation's computing device, this may increase the complexity and total time consumption.

For a vast majority of portable and handheld applications, sophisticated bench-top spectrometers with lab-grade sensitivity and resolution are not necessarily required. There are two features, which are sufficient for most of the spectral sensing investigations. 1. Detection of the spectral peak positions of a spectrum. 2. Determination of the intensity ratios between these peaks. In practice, very accurate generation of the target spectrum is not required for some sensing applications. Simple discrimination among known spectra with the low computational requirement is an attractive and simple strategy. We can also take advantage of a *priori* information of an unknown spectrum, e.g., the number of peaks, linewidth, or lineshape. In most cases, we have this advance knowledge of the sensing material, which can be used to successfully detect, analyze and

identify a target with an even less number of spectral encoders. This is our spectrometer's advantage.

1.7 InGaN/GaN-Based Photodetectors

In recent years, GaN and related compound semiconductors have emerged as critical optoelectronic materials due to their exclusive functionalities of light emission, detection, and transmission in the ultraviolet and visible wavelength ranges. In solid-state lighting, GaN-based light-emitting diodes (LEDs) have made revolutionary developments. Beyond solid-state lighting, GaN-based optoelectronic technology is unfolding a new realm of innovative and advanced device applications such as head-up displays for augmented reality [108,109], visible light communications (VLCs) [110,111], biochemical sensing [112], and multi-or-hyperspectral-imaging [113].

In a semiconductor, absorption of light occurs when the incident photon's energy is greater than its bandgap. Hence, a semiconductor photodetector's absorption cutoff wavelength can be modified and controlled by tuning the bandgap. Local strain engineering was recently shown to tune the bandgap of an InGaN dot-in-wire (DIW) nanostructure across the entire visible spectrum [114,115]. There is a large lattice mismatch at the InGaN/GaN heterostructure interface that generates compressive strain. This substantial built-in strain induces a strong piezoelectric field, which leads to a large bandgap tilting, a phenomenon known as the quantum-confined Stark effect (QCSE) resulting a redshift in the bandgap. This strain can be relaxed through the free surfaces of nanopillar structures. A blueshift in the bandgap can be achieved by fabricating nanopillars with different diameters using InGaN/GaN heterostructures. As a result, tuning of strain controls the emission wavelength depending on the diameter[116]. Among different nanostructures, the

nanopillar structure is one of the most effective. It has a higher surface-to-volume ratio compared to nanostripes and nanoholes to enable more effective strain relaxation [117].

Local strain engineering in GaN DIW structures has been previously applied to control and change individual nanopillars' emission wavelengths as a function of their diameters [118–122]. We expect a similar modulation of the photodetector's cutoff wavelength because of the change results from bandgap tuning. A notable advantage of tuning the intrinsic bandgap of a photodetector for spectroscopy applications is the insensitivity to the incident angle of light. In contrast, a similar silicon nanowire structure has also been shown to exhibit a diameter-dependent cutoff wavelength [123]. However, the wavelength tuning was achieved by optical interference and hence depended strongly on the incident angle of light [124,125].

1.8 UV/Visible Optical Spectroscopy- Potentially Enabled Applications

UV/VIS spectrometer is an essential analytical tool in scientific and industrial research for performing in-situ, noninvasive, and multiplexed measurements [10,54,126–132]. It has found broad applications in life science, microbiology, food industry, biomedical sensing, environmental monitoring, pharmaceutical research, and quality control. In this section, some of the earlier well-known applications using UV/VIS spectroscopy are reviewed.

In medical and life sciences, useful diagnostic information and surgical guidance can be revealed in this spectral range. An excitation light source is used to excite a biological sample. When light propagates through the sample, it undergoes multiple scattering and gets absorbed. The characteristics of the absorption, fluorescence, reflection, and scattering spectra change during the development of a disease. Hence, by making comparisons, disease screening is quantitatively studied using subsequent spectra. For example, the concentrations and oxygen saturation of hemoglobin [133], protein, and amino acid levels in cellular media are determined to diagnose two

hallmarks of cancer [134–137]. Cervical, skin, and breast cancers have spectral response curves from 330 - 480 nm [138], 440 - 640 nm [139], and 450 - 700 nm [140], respectively.

In geology and mineralogy, iron oxide is one of the most examined soil minerals that has an absorption spectrum in the UV-Visible wavelength range [141–145]. This is of great interest because it determines the mechanism of photochemical reactions between iron oxides and organic molecules in waters stimulated by sunlight [146]. Quantitative and qualitative analysis is also important in planetary exploration to determine the surface mineralogy, at present a great deal of attraction, for life to exist on Mars [147–149].

In food quality, the ripeness of tomatoes [150], bruises on apples [151], peach firmness [152] and infections in citrus food [153] are investigated in this spectral range. In all of these cases and others, miniature spectroscopic instrumentation offers an excellent measurement tool for remote sensing and nonionizing technology, especially operating in the UV-VIS wavelength range.

1.9 Monolithic Integration of Photodiodes and Light-Emitting Diodes

Most spectroscopic applications require not only a detection system but also an excitation light source to provide a reference in reflection and transmission spectroscopy or to excite the analyte in fluorescence spectroscopy. Chip-scale integration of an LED (light-emitting diode) light source is an important part of miniaturizing a spectroscopic system. However, very few works have been carried out to address this need [154–158]. There are two main challenges:

1. The difficulty of shrinking multiple dissimilar system components (light source and photodetectors) while simultaneously addressing their integration [159,160].

2. The heterogeneous integration of different material platforms for the light source and detectors, the already considerable size of the optical detection system preventing further integration of the light source, and interference between the light source and the spectral signal.

In reflection mode spectroscopy, the target sample is located on the top of the coplanar light source and detectors, both monolithically integrated on the same chip. When the light source is on, light is directed towards the target sample, where it interacts with the sample and is reflected back towards the detectors. In integrated modules, the most commonly used excitation light sources are mercury discharge lamps, halogen lamps, and lasers. However, GaN-based LEDs have their own advantage due to their easily adjustable wavelength, pixel number, and size.

For on-chip detection of the signal, conventional photomultiplier (PMT), single-photon avalanche diode SPAD detectors, CMOS photodiodes, and semiconductor photodiodes are employed. Most of the schemes require the incorporation of an optical filter, distributed Bragg reflectors (DBRs), or diffractive micro-optics to focus light onto the target sample and collect their emitted signals. Optical filters and diffraction-based systems are strongly dependent on the incident light angle. Light incident at low angles is strongly reflected whereas if incidence angles become larger it is highly transmitted. As a result, peak reflectance becomes sensitive to the normal incidence. However, for various applications sensing ability is needed under a wide range of incident angles and over a wide spectral range. This becomes even more important in integrated architectures where light may be incident over a wide range of angles due to intense scattering. Hence, insensitivity to incident angle is a clear advantage. GaN-based photodiodes are independent of the incident angle of light beam due to their larger viewing angle. In addition, optics-free detection and inherent wavelength selectivity can make them a good choice.

1.10 Research Objectives

This research's main objective is to develop an ultrathin, optics-free chip-scale reconstructive spectrometer based on GaN nanostructural absorbers The optical spectrometer operates across the entire visible spectral range and can be extended to ultraviolet and near-infrared

spectral regions. A spectrometer is not merely a device but a system. Miniaturizing a spectrometer requires seamless integration and scaling of multiple dissimilar functional components, including reference/excitation light sources, spectral encoders, photodetectors, and measurement circuits. This work focuses on an all-semiconductor platform with the heterogeneous integration of GaN-based LED and photodetectors. The demonstration of spectroscopic functionality without the use of any collimated and focusing optics remains the key goal. The major challenges lie in the spectrum reconstruction with a limited number of encoders/photodetectors, which result in challenging machine learning problems and the existing method performed inadequately. The research intends to resolve the challenge by developing new machine-learning methods with precise models of the data acquisition process and reconstructive algorithms, leading to faster and more accurate spectrum recovery.

There are several powerful techniques with which the InGaN LED and photodiode structures can be easily removed from their primary substrate and transferred to another flexible substrate. This opens up a novel approach that can potentially enable the realization of foldable, flexible, deformable, and personal wearable optical spectrometers for disposable chip application in a fully hybrid architecture, which is the motivation behind this research.

1.11 Research Contributions

The proposed research has provided the following key contributions:

- A proof-of-concept demonstration of an optical spectrometer based on 14 photodiodes, without any external optics or additional spectral filtering components, in the wavelength range 450 – 590 nm [30].
- The absorption properties of individual photodiodes were controlled via local strain engineering in nanostructured InGaN/GaN [30].

- Implementation of the photodiode array's spectroscopic function using compressive sensing and machine learning algorithms [30].
- Development of a monolithically integrated fully hybrid optical spectrometer architecture comprised of independently addressable photodiodes and LEDs for chemical sensing applications. An optical blocking structure was used to suppress the LED-photodetector interference and was shown to be essential for spectroscopic functionality. A proof of concept using a reflection spectroscopy configuration was experimentally conducted to validate the feasibly of simultaneously operating the LED excitation light source and the photodetectors [161].
- Designs to improve the absorption efficiency of InGaN nanostructured light absorbers. This part of the work was in collaboration with Juhyeon Kim [29].
- Proof-of-concept of a spectroscopic chip consisting of sixteen spectral encoders, which simultaneously functioned as photodetectors were monolithically integrated on a chip area of 0.16 mm^2. A non-negative least square (NNLS) algorithm with total-variation (TV) regularization and a choice of a proper kernel function was shown to deliver a decent spectral reconstruction performance in the wavelength range of 400 – 650 nm. The accuracies of spectral peak positions and intensity ratios between peaks were found to be 1.08% and 11.3%, respectively. No external optics such as collimation optics and apertures were used or necessary in the experimental demonstration, enabled by angle-insensitive light-harvesting structures, for an incident angle of light up to 30º, which included an array of nanopillar-shaped light

absorbers and a cone-shaped back reflector fabricated on the underside of the sapphire substrate [46].

1.12 Thesis Overview

This work focuses on an optical spectrometer concept utilizing an array of GaN photodiodes where local strain engineering enables the tailorable spectral response of individual photodiodes. The dissertation proposal is organized as follows. Chapter 2 offers a comprehensive description of the spectroscopic functionality of the GaN photodiodes array. Experimental results and the spectrum reconstruction of a test light source are also discussed in detail. Chapter 3 provides the proof-of-concept of monolithically integrated photodiodes and LEDs on the same platform. An experimental demonstration of such a hybrid optical spectrometer for reflectance spectroscopy is presented. Chapter 4 discusses the design aspects to increase the light-harvesting efficiency in the visible wavelength range. Improvement in the accuracy of spectral reconstruction is also shown. Chapter 5 delivers a proof-of-concept of a wafer-thin chip-scale portable spectrometer based on a reconstructive algorithm. A decent spectral reconstruction performance in the wavelength range of 400 – 650 nm is also presented. Chapter 6 concludes the thesis and proposes future study ideas in this research.

Chapter 2 On-Chip Optical Spectrometer Based on GaN Nanostructural Absorbers[1]

This chapter demonstrates the proof-of-concept of a spectroscopic chip based on wavelength-selective semiconductor photodiodes. The photodiodes have inherent spectral filter properties eliminating the use of separate filters. The absorption properties of individual photodiodes were tuned via local strain engineering in nanostructured InGaN/GaN. By varying the diameters of individual nanopillars, the cutoff wavelengths of absorption were varied across the chip. The spectroscopic function was also demonstrated using these photodiodes in combination with a spectral reconstruction algorithm. The responsivity of each photodiode was measured and stored as a library file. To measure the unknown spectrum of the incident light, photocurrent was measured under illumination from each pixel. By using the measured photocurrent and responsivity with a suitable reconstruction algorithm, the spectrum of unknown incident light was generated. The spectral filtering is intrinsic to the nanopillars and has negligible dependence on the incident angle of light, enabling an optics-free spectrometer chip and simplifying integration in a lab-on-a-chip layout. Such a compact, ultrathin optical spectrometer is of great importance due to its immense potential for portable and remote sensing applications. Figure 2-1 shows an illustration of such a system.

[1] T. Sarwar, S. Cheekati, K. Chung, and P. C. Ku, "On-chip optical spectrometer based on GaN wavelength-selective nanostructural absorbers," Appl. Phys. Lett. **116**(8), (2020). TS: methodology, experiment, data analysis, and results interpretation; SC: spectral reconstruction analysis; KC: fabrication.

2.1 Operating Principle

A semiconductor photodiode is an optoelectronic device that absorbs optical energy and converts it to electrical energy, which is known as photocurrent. The cutoff wavelength of a semiconductor photodiode is given by its bandgap. In a GaN nanopillar array comprising of InGaN quantum wells, the strain relaxation around the nanopillar's perimeter leads to the modulation of the bandgap along the radial direction because of the piezoelectric effect. The bandgap at the center of the nanopillar can be determined using a solid mechanics model [162,163] as

$$\mathrm{E_g} = \mathrm{E_0} - \mathrm{B_m}\gamma(\mathrm{D}), \tag{2-1}$$

where E_0 is the bandgap of bulk InGaN, $E_0 - B_m$ is the bandgap of InGaN quantum wells in thin films due to the quantum-confined Stark effect (QCSE), and

$$\gamma(D) = 1 - \sinh \kappa D/2, \tag{2-2}$$

where $\gamma(D)$ is a geometric factor that depends on the elastic property of InGaN (κ factor) and the diameter of the nanopillar D [164–166]. In this way, the bandgap of nanopillar structures is directly related to the amount of strain relaxation that varies with diameter. The strain relaxation in nano-pillars increases the bandgap. The concept of local strain engineering in GaN nanostructures has been previously demonstrated to tune the emission wavelength of individual nanopillars as a function of their diameters [118–122]. The same principle is used to control the cutoff wavelengths of individual photodiodes across the visible spectrum. The DIW nanopillars can be fabricated either using a top-down or bottom-up process. In this work, we adopted the top-down process. The nanopillars were defined by lithography and etching. Because all nanopillars have the same epitaxial structure, any change in the absorption properties can be attributed to the strain relaxation effect.

2.2 Sample Preparation

The sample consists of an array of 14 photodiodes as illustrated in Figure 2-1. Each photodiode further comprises of an array of DIW nanopillar structures. The diameter of all nanopillars within each photodiode was fixed but varied from 55nm to thin film among different photodiodes. All photodiodes have the same dimensions of 100 μm by 100 μm. The overall size of spectrometer is 1.5 cm by 1.5 cm. The nanopillar structures were defined and fabricated using a top-down process. The epitaxial wafer is a standard LED structure with five periods of $In_xGa_{1-x}N$ (2.5nm)/GaN (12nm) quantum wells grown on a c-plane sapphire substrate by metal-organic chemical vapor deposition (MOCVD). The epitaxial structure of $In_xGa_{1-x}N$/GaN nanopillars and the fabrication process flow are shown in Figure 2-1 and Figure 2-2, respectively.

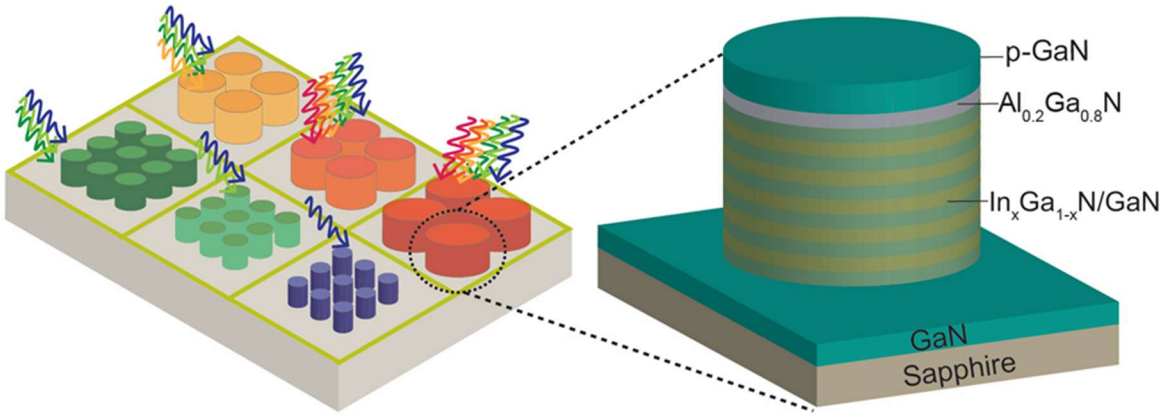

Figure 2-1: (a) Schematic of the spectrometer concept utilizing a wavelength-selective photodiode array to enable a thin, compact, and potentially flexible (by removing the substrate) spectrometer chip. (b) The epitaxial structure of individual DIW nanopillar structures as a building block for the wavelength-selective photodiode, comprising of 5 InGaN/GaN multiple quantum. wells (MQWs) and a thin AlGaN electron blocking layer.

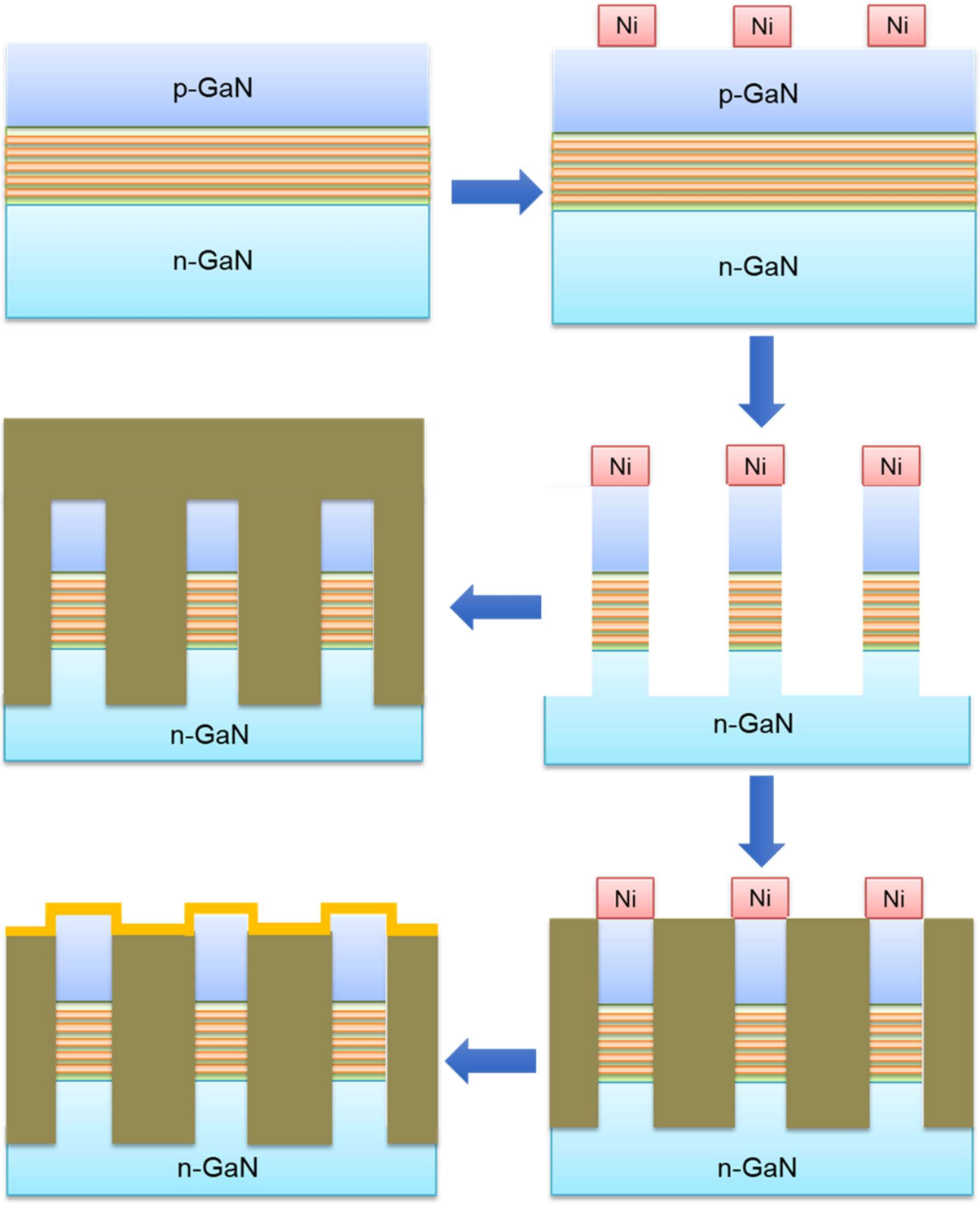

Figure 2-2: Fabrication process flow of nanopillar by a top-down process. The epitaxial wafer is a standard LED structure grown on a sapphire substrate. Fabrication involves e-beam lithography to define the diameters of all nanopillars in a single step, ICP-RIE etching combined with subsequent wet etching in a diluted KOH. After that, planarization and fabrication of electrical interconnects were completed.

The electroluminescence showed orange emission (λ=590nm at 3V) from the thin-film LED. E-beam lithography was used to define the diameters of all nanopillars in a single step. Inductively-coupled plasma reactive ion etching (ICP-RIE) followed by wet etching in 2% KOH solutions was used to fabricate the nanopillars. After defining the structure, the planarization, electrical insulation, and the patterning of electrical interconnects were carried out [121]. The scanning electron microscope (SEM) images for 55nm and 100nm $In_xGa_{1-x}N$/GaN nanopillars are shown in Figure 2-3(a) and 2-3(b), respectively. Optical microscope images of the spectrometer device are shown in Figure 2-4(a) and 2-4(b).

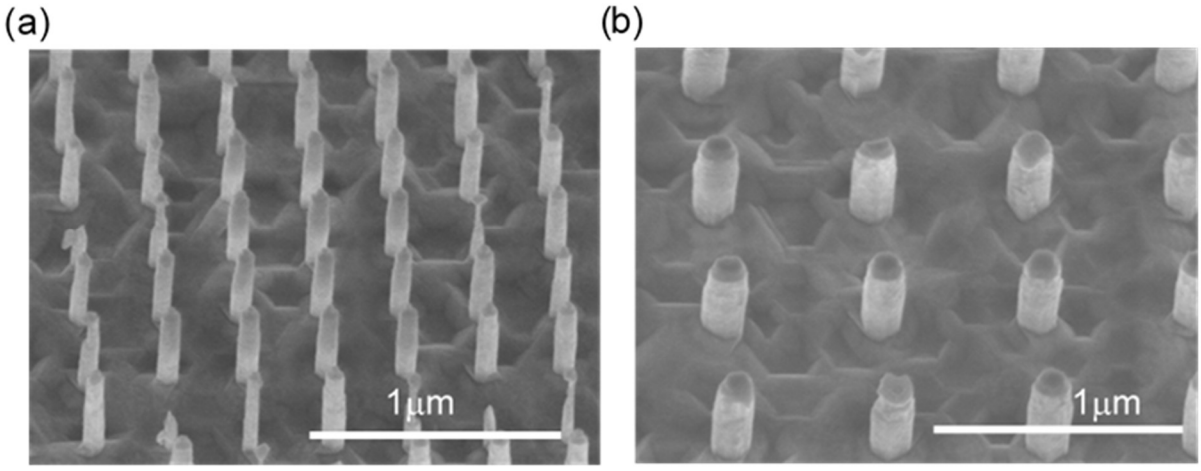

Figure 2-3: The scanning electron micrographs of two as-etched nanopillar arrays of different diameters before planarization and metallization. Vertical sidewalls were achieved using a two-stage dry/wet etch process.

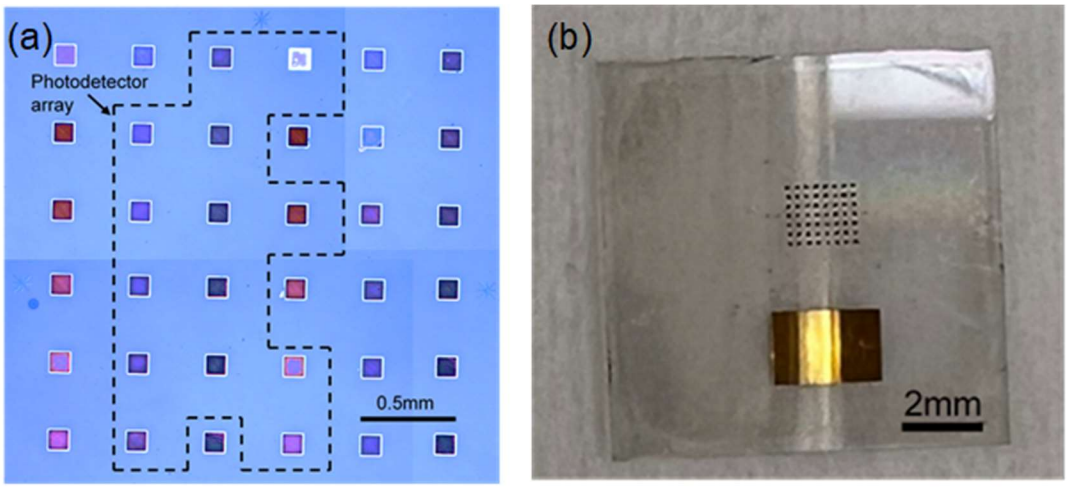

Figure 2-4: (a) The bright-field optical microscope image of the spectroscopic chip used in this study consisting of an array of 14 photodiodes, each with a size of 100μm x 100μm. Each photodiode is further comprised of an array of nanopillar structures with different nanopillar diameters. Chip contains some test pixels outside the photodetector array. (b) The fabricated spectrometer device. The array of dark squares on the right are the photodiodes. The dark color of the photodiodes is the result of light absorption.

2.3 Characterization of GaN Photodiodes_Photoresponse

After fabrication, each photodiode was characterized for its photoresponse. The measurement setup is illustrated in Figure 2-5. Light from a solar simulator (Abet Technologies) was filtered by a monochromator (Acton Research Corporation 2500i, 0.500m focal length, triple-grating). The broadband spectrum of light source measured from a commercial spectrometer is shown in Figure 2-6(a). The filtered light was then directed upon individual photodiodes via a fiber optic cable. A current meter (Keithley 6482) was used to measure the photocurrent from the photodiode which was biased at 0V. The wavelength of the incident light was swept from 450nm to 590nm with a step size of 1nm. The spectrum of filtered monochromatic light is also measured from a commercial spectrometer at each wavelength and shown in Figure 2-6(b).

The optical power of incident light was separately measured from a reference detector using an integrating sphere. The size of the optical beam spot on the sample was also estimated which allowed us to calculate the responsivity.

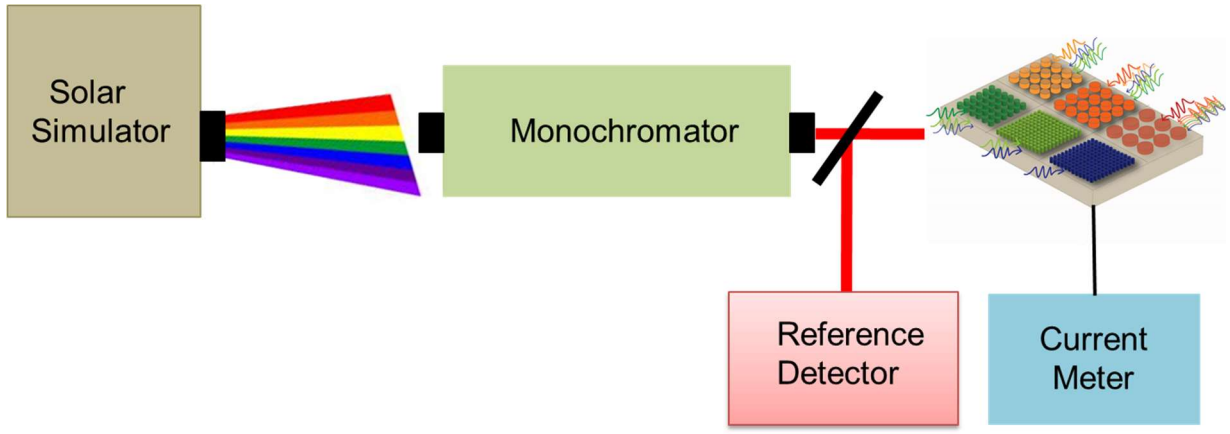

Figure 2-5: Schematic of responsivity measurement experimental setup. Light from a solar simulator was filtered by a monochromator and directed upon individual photodiodes with a fiber optic cable. A current meter was used to measure the photocurrent from the photodiode which was biased at 0V.

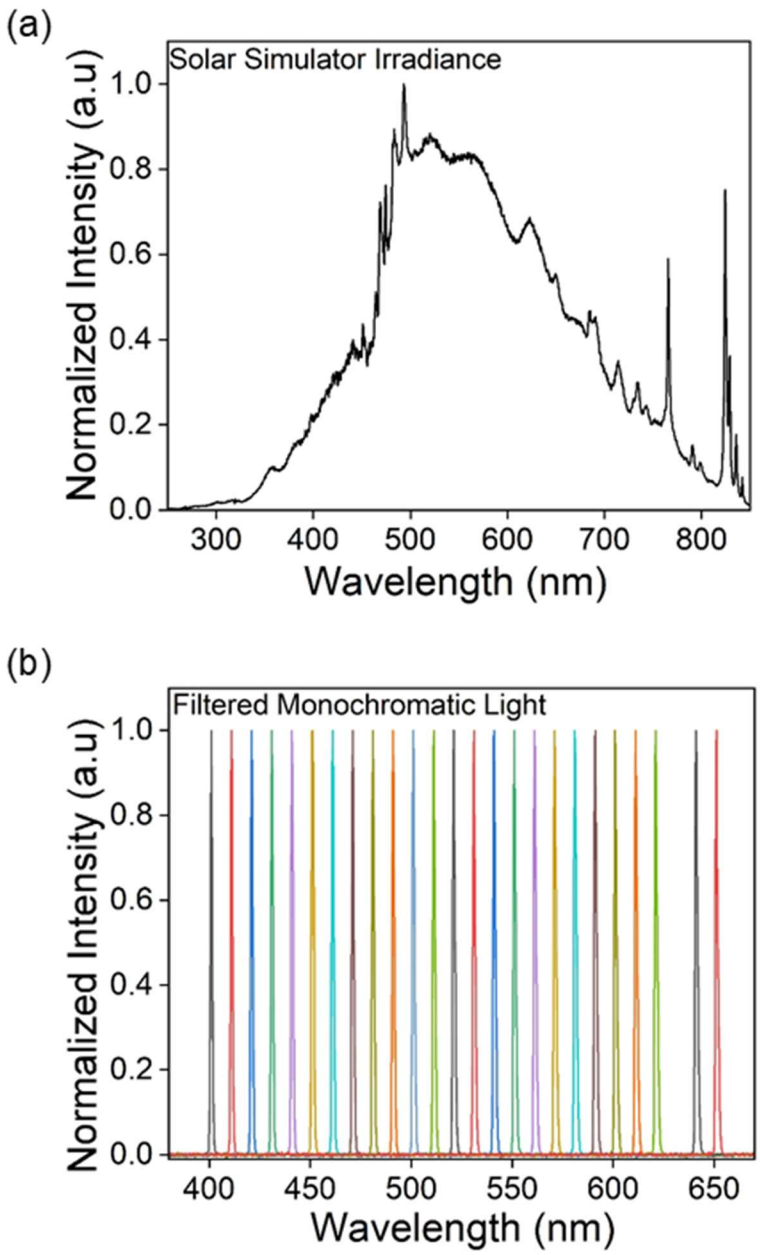

Figure 2-6: Measured spectrum using a commercial spectrometer for (a) Broadband light source, a solar simulator is used in this study. (b) Filtered monochromatic light reaching the spectrometer chip; one wavelength at a time.

2.3.1 Results and Discussion-Responsivity

Figure 2-7(a) shows the result for responsivity of each photodiode under the illumination of monochromatic light. It can be seen that the absorption cutoff wavelength blue shifts while the nanopillar diameter decreases. The peak responsivity also decreases with the decreasing diameter, which is largely due to the reduction of the InGaN light-absorbing area. Figure 2-7(b) shows the responsivity normalized to the total nanopillar area in each photodiode. The normalized responsivity of the smallest photodiodes is ~10X lower than that of the larger ones. The difference is attributed to the surface recombination of photogenerated electrons and holes. Proper surface passivation is expected to bridge the gap in the future.

To understand the blue shift of the cutoff wavelength, Figure 2-7(c) compared the dependence of electroluminescence peak wavelength versus the nanopillar diameter measured from the same photodiode devices but biased at the lowest possible forward voltage to avoid any carrier screening. A very good agreement was obtained between the emission and the absorption cutoff wavelengths, suggesting the origin of the absorption blueshift is due to the change of the bandgap as a result of local strain engineering.

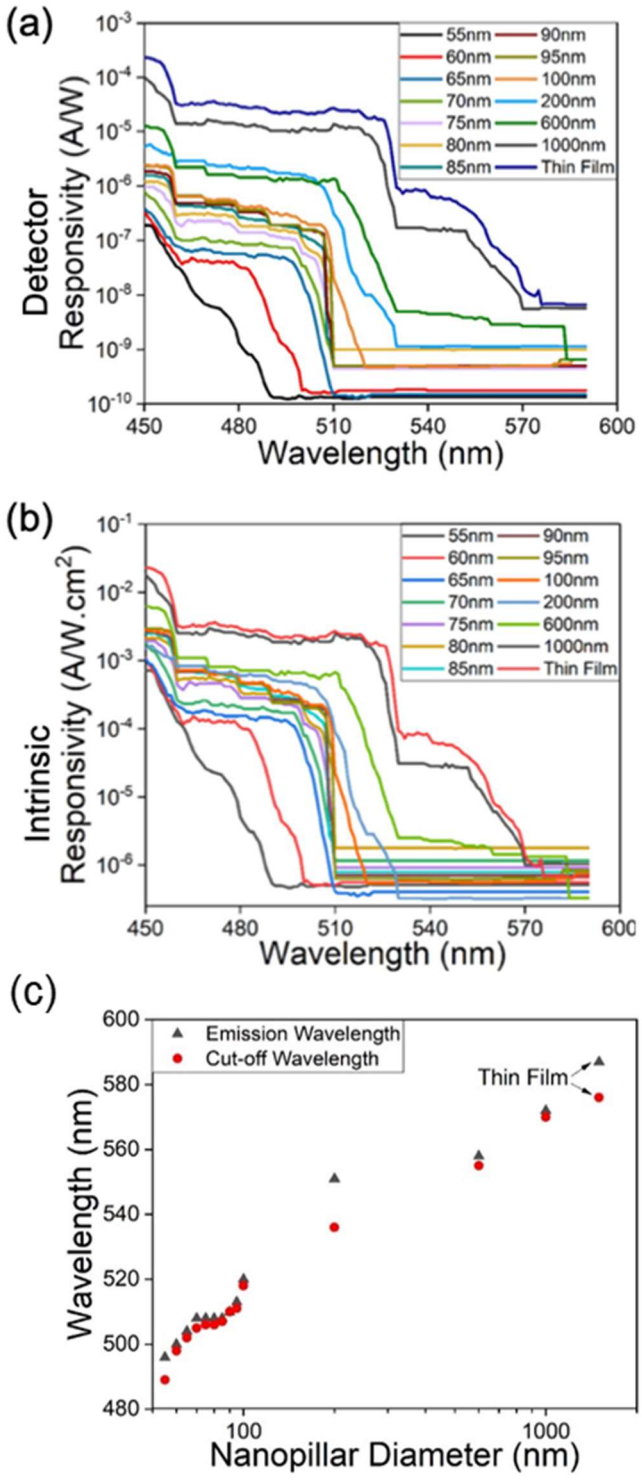

Figure 2-7 (a) The measured responsivities of the 14 photodiodes with different nanopillar diameters. (b) The measured responsivities normalized to the total nanopillar cross-sectional area in each photodiode. (c) The comparison of the emission wavelength from each "photodiode" biased at the lowest possible forward voltage to obtain the electroluminescence spectra and the cutoff wavelength from part (a).

2.4 Spectral Reconstruction

Numerically, an optical spectrometer has an ability to transform the photocurrent from photodiodes into an unknown incident optical spectrum through a pre-measured responsivity matrix. Thus, an appropriate algorithm is required for spectrum reconstruction. Unprecedented developments in advanced signal processing and machine learning techniques have enabled the chip-scale miniaturization of spectrometers in the true sense. There are several reconstruction algorithms available to determine the unknown spectrum information. By carefully adopting a suitable reconstruction technique, we can achieve high-dimensional information from low-dimensional data. Hence, after obtaining the responsivities for all 14 photodiodes, we demonstrated the spectroscopic function by illuminating the sample with a test light source comprising of two commercial light-emitting diodes (LEDs). Figure 2-8 shows the experimental setup for measuring the photocurrent from each photodiode. No external optics was used between the LED output and the sample. In addition, we also measured the spectrum of the test light source using a commercial spectrometer (Ocean Optics HR2000) for comparison. We denote the photocurrent measured (at 0V) from the i-th photodiode as I_{P_i}. The spectrum P_j of the test light source at a wavelength λ_j satisfies

$$\mathrm{I_{P_i}} = \sum_{\mathrm{j}} \mathrm{R_{ij}} \times \mathrm{P_j}, \tag{2-3}$$

where R_{ij} is the responsivitiy of the i-th photodiode measured at λ_j. Hence, the spectrum can be reconstructed by inverting (1). Because the number of photodiodes is much smaller than the number of wavelengths used to characterize R_{ij}, we have an under-determined system for which a variety of algorithms have been developed for spectral reconstruction. In this work, we applied one of the simplest algorithms, the non-negative least square algorithm (NNLS) which minimizes

$\min_{P_{guess} \geq 0} \|I_p - RP_{guess}\|^2$ with an L_2 norm [49]. We also show an improved result by applying orthogonal matching pursuit (OMP) [167–169].

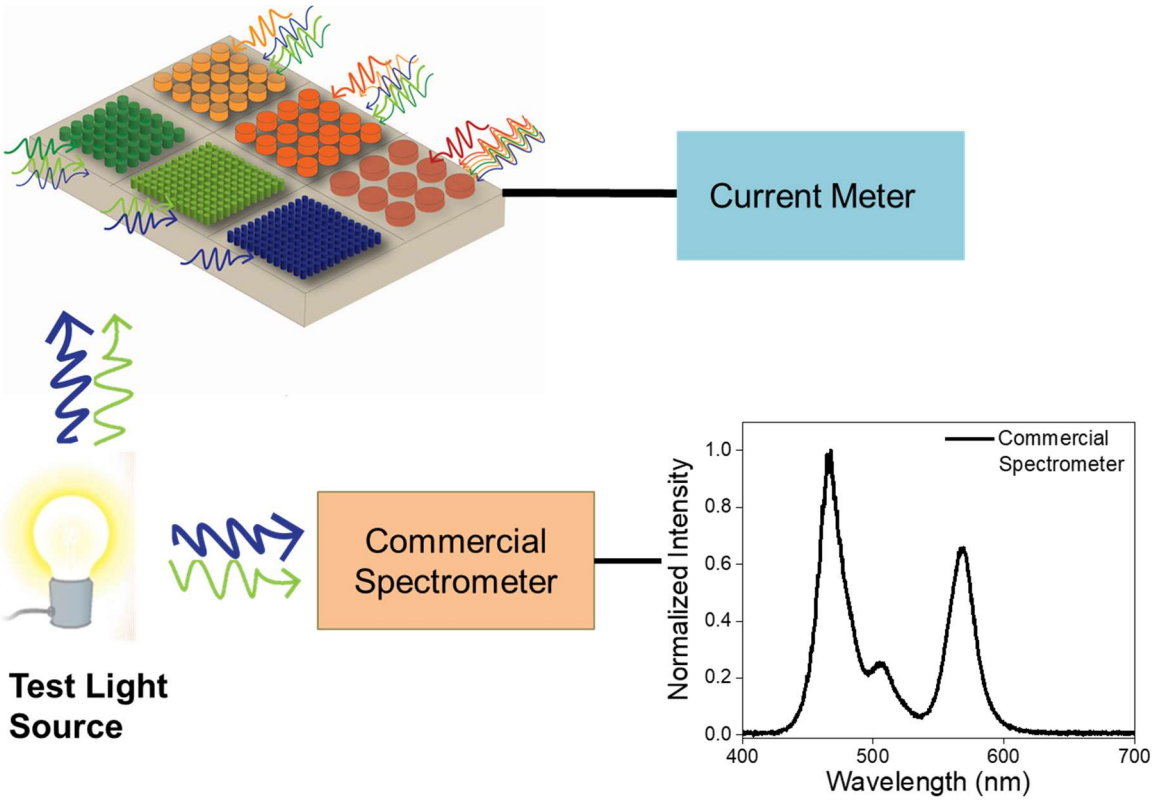

Figure 2-8: Experimental setup for measuring the photocurrent from each photodiode under the illumination of a test light source comprising of two commercial LEDs. Photocurrent was measured to demonstrate the spectroscopic function. No external optics was used. The spectrum of the test light source was also measured using a commercial spectrometer for making a comparison.

2.4.1 Discussion_Spectral Reconstruction

The NNLS algorithm finds a solution by first constructing a zero spectrum and treating the responsivity matrix as a set of basis vectors to compute its dual vector. Next, it finds the maximum dual vector index and uses the responsivity pseudoinverse to assign the corresponding spectral value at that index. This continues until the dual vector has all positive values. While this algorithm will always converge to a solution, the solution might not be optimal [170]. Figure 2-9(a) shows the reconstructed spectrum using the Kronecker delta function at each wavelength as a basis. The reconstructed spectrum picks up the peak wavelengths of the test light source although the shorter wavelength peak has a slight offset, likely due to the small number of photodiodes we used. However, most of the spectral values remain 0 due to the nature of minimizing the L_2 norm which makes the reconstructed spectrum sparse. For applications with prior knowledge of the spectral nature, one can choose a different basis, e.g., a gaussian or Lorentzian basis [171]. We can also enhance the NNLS algorithm using OMP which iteratively reduces the residual between the measured photocurrent and calculated photocurrent (from the reconstructed spectrum) by using the residual to construct a correction to the spectrum. The OMP cannot converge when there is noise present in the photocurrent or responsivity values, so we simply limit it by setting a maximum number of iterations to 141, the number of bases. Figure 2-9(b) shows spectral reconstruction using the Lorentzian basis (5nm FWHM), with and without OMP. The result with the OMP shows an improved intensity ratio between the two peak wavelengths as well as more spectral contents outside the peaks. Further improvements are expected by designing a photodiode array with a larger number of photodiodes. Moreover, the noise is expected to be reduced by designing more equalized responsitivity between different photodiodes, e.g. by increasing the number of nanopillars at a smaller diameter.

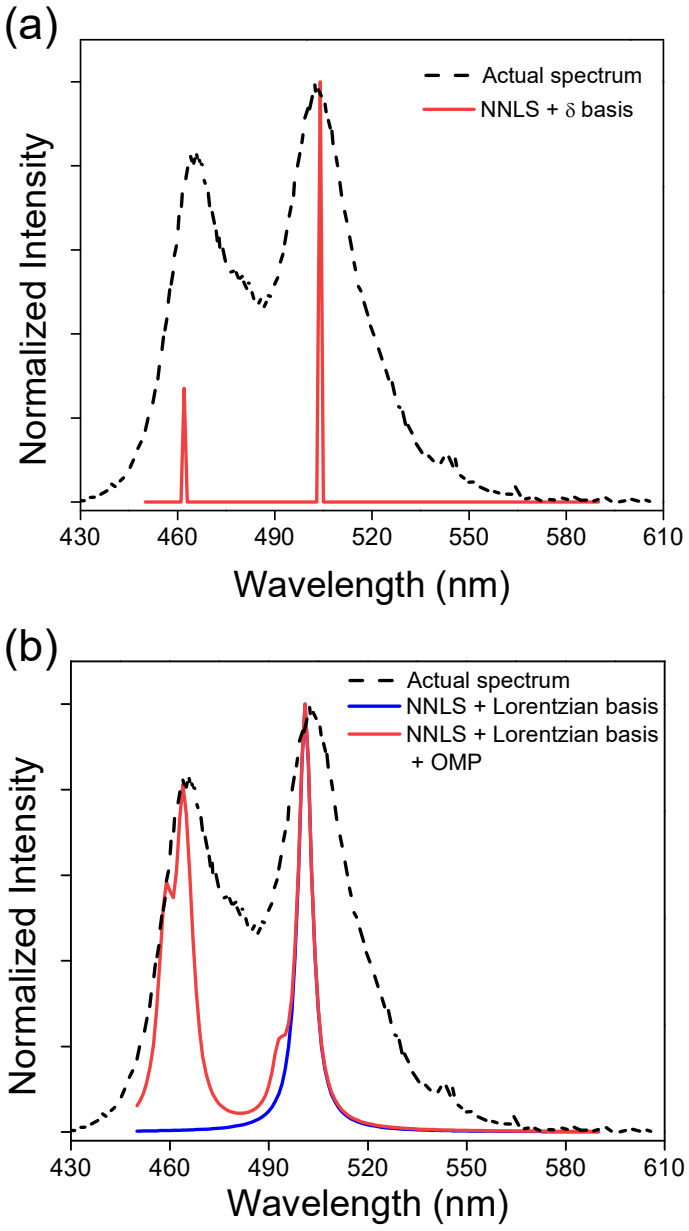

Figure 2-9: Spectral reconstruction from the photocurrents measured from the 14 photodiodes illuminated by a test light source. The spectrum measured from a commercial spectrometer is also shown as a dashed line for comparison. The spectra reconstructed from the NNLS algorithm with (a) Kronecker delta function basis and (b) Lorentzian basis (5nm FWHM) with and without orthogonal matching pursuit (OMP).

2.5 Conclusion

In summary, an array of monolithically integrated GaN-based photodiodes with built-in spectral filtering responses was demonstrated. Local strain engineering in GaN DIW nanopillar structures enabled the control of the absorptive properties of each photodiode. The comparison to the emission wavelength variation from the same set of devices confirmed the strain relaxation was the major cause for the blue shift of the absorption cutoff wavelength with a decreasing nanopillar diameter. Spectroscopic function was also demonstrated using these photodiodes in combination with a spectral reconstruction algorithm. The spectral filtering is intrinsic to the DIW nanopillars and has negligible dependence on the incident angle of light, enabling an optics-free spectrometer chip and simplifying integration in a lab-on-a-chip layout. Finally, spectral reconstruction for an under-determined system is a topic in a rapidly developed field: compressive sensing. A more suitable algorithm may be identified to work with the nature of our absorber spectral properties.

Chapter 3 Ultrathin Optics-Free Spectrometer with Monolithically Integrated LED Excitation[2]

A semiconductor spectrometer chip with a monolithically integrated light-emitting diode was demonstrated. The spectrometer design was based on a computational reconstruction algorithm and a series of absorptive spectral filters directly built into the photodetectors' active regions. The result is the elimination of the need to employ external optics to control the incident angle of light. In the demonstration, an array of gallium nitride (GaN) based photodetectors with wavelength selectivity generated via the principle of local strain engineering were designed and fabricated. Additionally, a GaN-based LED was monolithically integrated. An optical blocking structure was used to suppress the LED-photodetector interference and was shown to be essential for spectroscopic functionality. A proof of concept using a reflection spectroscopy configuration was experimentally conducted to validate the feasibly of simultaneously operating the LED excitation light source and the photodetectors. Spectral reconstruction using a non-negative least squares (NNLS) algorithm enhanced with orthogonal matching pursuit was shown to reconstruct the signal from the reflection spectroscopy. Optics-free operation was also demonstrated.

[2] T. Sarwar and P. C. Ku, "Ultrathin Optics-Free Spectrometer with Monolithically Integrated LED Excitation," Micromachines **13**(3), 382 (2022). TS: methodology, experiment, data analysis, and results interpretation.

3.1 Introduction

To enable a portable and handheld in-vivo monitoring system, chip-scale optical spectrometers in a fully integrated mode are needed. A fully hybrid design allows the integration of photonic, microelectronic, and image-processing modules on a single chip. The integration of micro-LEDs as a light source and photodiodes as a detector can provide localized illumination and detection that is highly desirable in many applications because micro-LED can target specific entities at precise wavelengths, without influencing other parts of the system. Among various approaches, spectrometers based on reconstructive algorithms [172–174] shift the complexity of processing spectral information from physical components to software computations [175–178]. A reconstructive spectrometer consists of a series of photodetectors with different spectral responses $R_k(\lambda)$, where k denotes the k_{th} detector and λ is the optical wavelength. For an unknown spectrum S(λ), the photocurrent generated by the k_{th} detector is given by $I_k = R_k(\lambda)S(\lambda)$. With a set of known $R_k(\lambda)$, one can reconstruct the unknown spectrum $S(\lambda)$ by inverting the above equation using a computational algorithm, e.g., the non-negative least squares (NNLS) method. The spectral resolution is determined by the size of the $R_k(\lambda)$ matrix and how differently each photodetector's spectral response relates to another. Ideally, there should be no correlations between any two photodetectors' responses and the number of photodetectors should be equal to the spectrometer's spectral range divided by the desired spectral resolution. For many applications, however, a reconstructive spectrometer can generate useful information even working as an underdetermined system. For example, the locations of a spectrum's peaks and the relative intensities between them are often sufficient information. Moreover, the reconstruction algorithms can be enhanced by adding constraints that can either be improved over time via learning or be

constructed based on the specific characteristics of the application of interest [179,180]. This is highly desirable for many applications targeted by a miniaturized spectrometer.

A conventional semiconductor-based photodetector's spectral response cannot be easily tuned. Therefore, a reconstructive spectrometer has often been implemented with a series of filter/detector combinations. However, dispersive spectral filters are highly sensitive to the incident angle of light, requiring additional collimation optics, which add to a system's bulkiness and weight. Recently, absorptive filters, either standalone or built into the photodetectors, have been successfully integrated into a reconstructive spectrometer [31,41,43]. Absorptive filters' spectral responses have a weak dependence on the incident angle of light [47]. As a result, collimation optics either become optional or can be replaced by other imaging optics to enable a spectrometer array for hyperspectral imaging.

3.2 Monolithic Integration of LED and Photodiodes

Most spectroscopic applications require not only a detection system but also an excitation light source to provide a reference in reflection and transmission spectroscopy or to excite the analyte in fluorescence spectroscopy. Chip-scale integration of an LED (light-emitting diode) light source is an important part of miniaturizing a spectroscopic system. However, very few works have been carried out to address this need [112,135,143,156,158,181–183]. The main challenges include the heterogeneous integration of different material platforms for the light source and detectors, the already considerable size of the optical detection system preventing further integration of the light source, and interference between the light source and the spectral signal. In this work, we successfully demonstrated monolithic integration of LEDs and an array of wavelength-selective photodetectors.

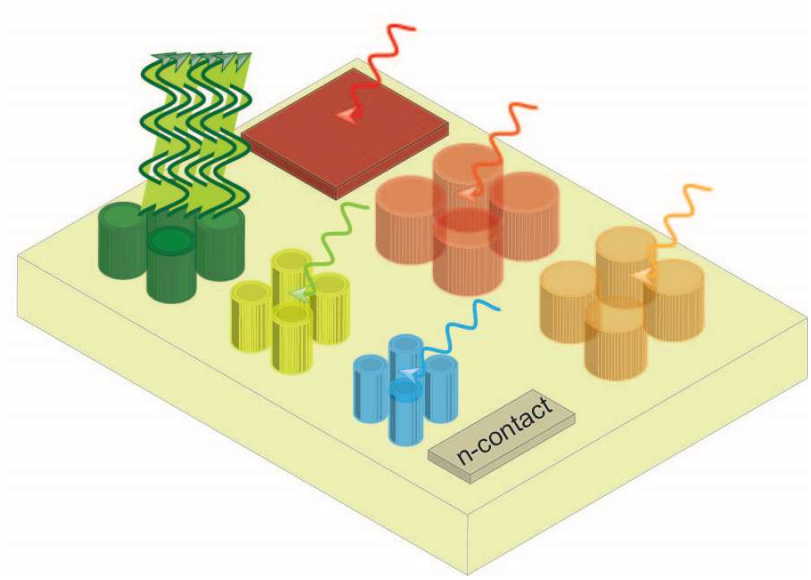

Figure 3-1: Schematic of the spectrometer concept utilizing monolithically integrated wavelength-selective photodiode array with Light emitting diode (LED) to enable an optics-free, ultra-thin film spectrometer chip.

We experimentally validated the feasibility by showing the negligible interference of the on-chip LED due to the portion of light directly leaked to the detector array. We also showed an example of reflection spectroscopy using the on-chip LED and a notch filter to simulate an analyte absorbing at a specific wavelength as shown in Figure 3-1.

3.3 Design Configuration

The spectrometer design consists of an array of GaN-based wavelength-selective photodetectors [184]. When the strained InGaN quantum well active region is made into a nanopillar geometry, the strain relaxation shifts the emission wavelength of the quantum well to a short wavelength [185]. The strain relaxation is nonuniform and decreases from the edge to the center. As GaN exhibits a large piezoelectric polarization due to the in-plane strain, the strain

relaxation leads to the change of the bandgap and the absorption cutoff wavelength. The amount of wavelength shift depends on the nanopillar's diameter and the emission wavelength of the original quantum well. In this work, the sample's epitaxial structure includes five periods of InGaN/GaN quantum wells sandwiched between a GaN pn junction. The room temperature (sample uncooled) electroluminescence peaked at 590 nm and can be tuned between 480 and 590 nm depending on the nanopillar diameter.

3.4 Materials and Methods

Figure 3-2 shows the device schematic. The device consists of an array of photodetectors, each constructed based on an array of GaN nanopillars comprising InGaN/GaN multiple quantum wells. It also has an LED which was made of GaN nanopillars. The nanopillar's diameter was varied to control emission and absorption properties. The sample was grown by metal–organic chemical vapor deposition (MOCVD) on a c-plane sapphire substrate. After growth, the sample was patterned using electron-beam lithography into a series of nanopillar arrays. Each array is either a photodetector or LED depending on the bias. Each array occupied a chip area of 100 μm by 100 μm. All nanopillars in the same array have the same diameter. The spacing between two adjacent nanopillars was 250 nm for smaller nanopillar diameters and 2 μm for larger ones. The nanopillars were formed using a two-stage etching process, first using inductively coupled plasma-reactive ion-etching (ICP-RIE) followed by an anisotropic wet etch in a 2% diluted KOH solution (AZ-400). Chromium was used as the etch mask. The wet etch step created a vertical sidewall, allowing the nanopillar diameter to be better controlled. The etching was stopped once we cleared the quantum well region. The resulting nanopillar height was 260 nm. After etching, a conformal 50 nm thick SiN_x layer was deposited to form electrical insulation around the nanopillars. The

sample was then finished with planarization using SiO_2 and electrode deposition (Ni–Au for p-contact and Ti–Au for n-contact).

3.5 Experimental Details

Two sets, each containing a total of 14 nanopillar arrays were fabricated along with a few additional test structures. The optical image of the as-fabricated sample and the scanning electron micrographs of two of the arrays immediately after the patterning step are shown in Figure 3-3. To choose the nanopillar diameters, we aim to distribute the absorption cutoff wavelengths of the nanopillar arrays evenly across a wide wavelength range. Previously, using a simple one-dimensional solid mechanics model which modeled the InGaN quantum well with a linear chain of atoms whose positions were determined from the balance of the strain relaxation due to the nanopillar geometry and the intrinsic compressive strain due to the lattice mismatch. The result is that the emission wavelength of each nanopillar array follows an exponential dependence $1 - \sinh \kappa D/2$ on the nanopillar's diameter D, where κ describes the material's elastic property [186]. The emission wavelength of each nanopillar array was previously shown to be identical to the absorption cutoff wavelength at a zero bias [30]. To this end, we varied the nanopillar diameter from 55 to 100 nm with a 5 nm increment and from 100 nm to thin film with a larger increment to even out the emission wavelength distribution across the blue–green–orange range. One of the 14 nanopillar arrays was chosen to operate in the LED mode with a forward bias applied. The emission spectrum was measured by Ocean Optics HR2000 and is shown in Figure 3-4.

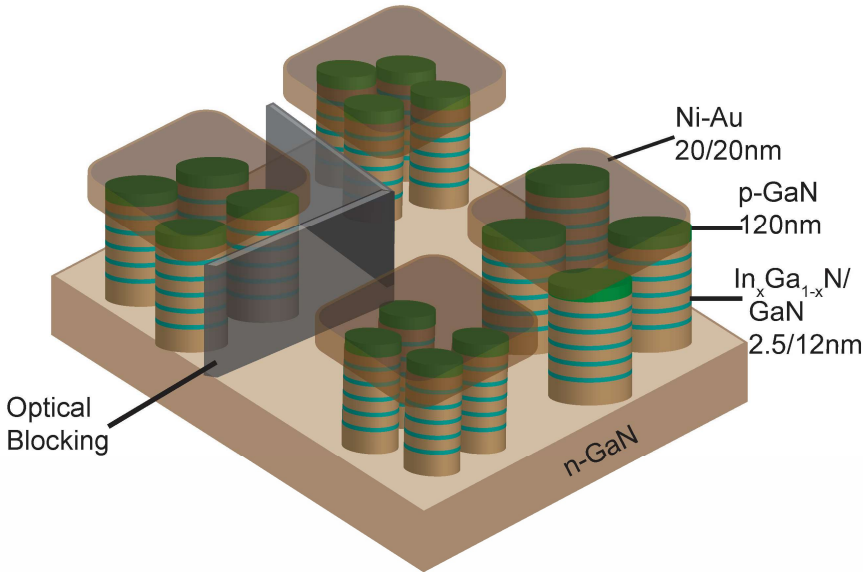

Figure 3-2: Schematic of the proposed spectrometer chip with a monolithically integrated LED. As shown in the illustration, there are three photodetectors and one LED separated by an optical blocking structure. The three photodetectors exhibit different spectral responses due to the difference in the nanopillar diameter.

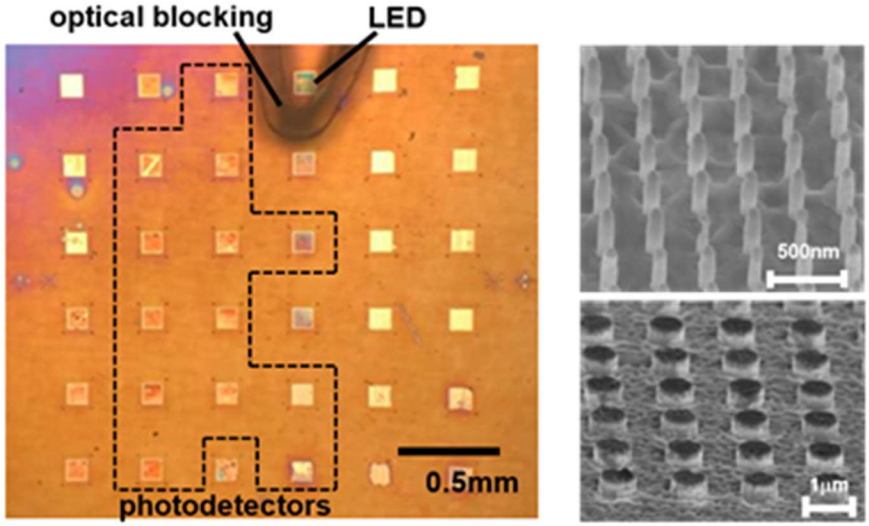

Figure 3-3: The optical image of the as-fabricated spectrometer chip with a monolithically integrated LED light source. Each yellow square is a nanopillar array with a chip area of 100 μm × 100 μm. The nanopillar diameters of the 13 arrays enclosed by the dashed line vary from 55 nm through thin film (see Figure 3a,b for the diameter values). The black-colored structure is the

enamel-coated PET optical blocking structure to suppress the direct capture of the LED emission by the photodetectors. The edge-to-edge spacing between two arrays is 0.3 mm. The two scanning electron micrographs show two nanopillar arrays after etching but before planarization. The diameters of the nanopillars are 80 nm and 800 nm for the images on the top and bottom, respectively.

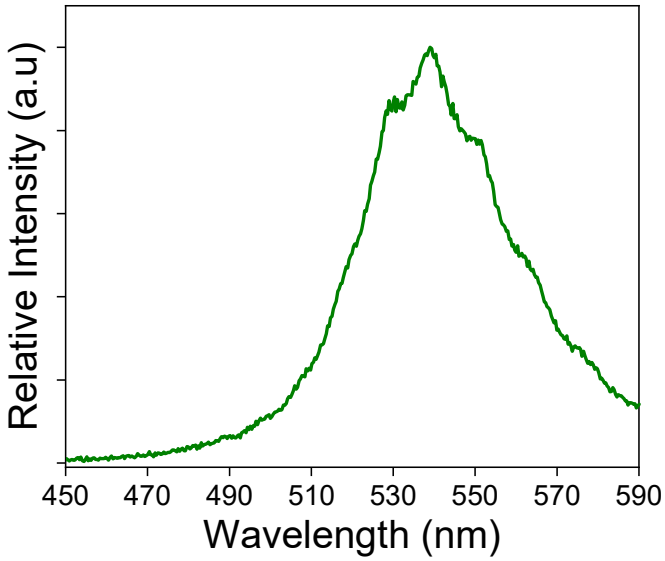

Figure 3-4: The emission spectrum of the on-chip LED (biased at 8V) measured by Ocean Optics HR2000. The LED device is also a nanopillar array with a diameter of 200 nm.

3.6 Optical Blocking and its Effectiveness

As shown in Figure 3-2, the LED is placed adjacent to the photodetector array. The spacing between each array is 0.3 mm. Due to the proximity, the LED emission can be directly captured by the photodetectors. This interference can overwhelm the spectroscopic signal, which is likely to be much weaker than the emission along a direct path from the LED to the photodetectors. To

address this challenge, we fabricated an optical blocking structure using polyethylene terephthalate (PET). We first coated the PET with black enamel. We then shaped the PET sheet into a wall-like structure and attached it to the sample surrounding the LED. Figure 3-4 shows that the PET optical blocking layer successfully suppressed the LED interference. The photocurrents due to the direct LED emission being captured by the photodetectors were significantly reduced to be within the same order of magnitude as the dark currents measured with the LED turned off.

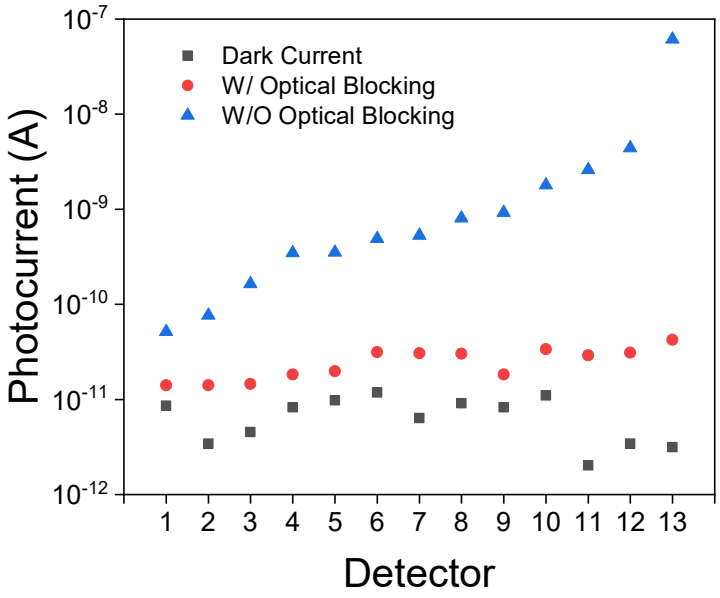

Figure 3-5: The photocurrents measured from the 13 photodetectors using a semiconductor parameter analyzer (Keithley 4200) under various scenarios: the dark currents measured when the on-chip LED was electrically disconnected; the photocurrents with and without the optical blocking structure integrated on the LED (shown in Figure 1a) which was biased at a constant 8V. LED emission reflected from an off-chip object is negligible. As a result, the photocurrents measured were the result of LED emissions being directly captured by the photodetectors along a direct path on the chip. With optical blocking, the photocurrent due to the LED interference can be considerably suppressed to be within the same order of magnitude as the dark current.

3.7 Results

Unlike a filter-based spectrometer, the reconstructive spectrometer's operating range is largely determined by the wavelength range in which the photodetectors' responses do not have a strong correlation. To determine the operating wavelength range of our device, we first measured each photodetector's responsivity between 450 and 590 nm with a 1 nm spectral resolution. All photodetectors were kept at zero bias. The results are shown in Figure 3-6(a,b). The responsivity shown uses a standard definition for a silicon photodetector and accounted for all the light not absorbed when passing between the nanopillars and ~88% not absorbed when passing through the quantum wells. A stronger absorption, e.g., by increasing the nanopillar array's fill factor, can further enhance the responsivity.

Once the responsivities of all 13 photodetectors were obtained, we can determine the operating range of the spectrometer by performing the NNLS algorithm with a series of delta-function spectra, i.e., spectra with only a finite value at a specific wavelength and zeros everywhere else. The result is shown in Figure 3-7. The reconstruction is accurate between 450 and 540 nm. Although the emission wavelength of the photodetector ranges from 480 through 590 nm, the operating window is not the same. The photodetectors' responses beyond 540 nm are not sufficiently diverse, which results in a large reconstruction error between 540 and 590 nm. This can be remedied by increasing the responsivities of all photodetectors [187]. In contrast, although all photodetectors absorb strongly between 450 and 480 nm, the correlation between their responsivities is weak enough to still lead to an accurate reconstruction.

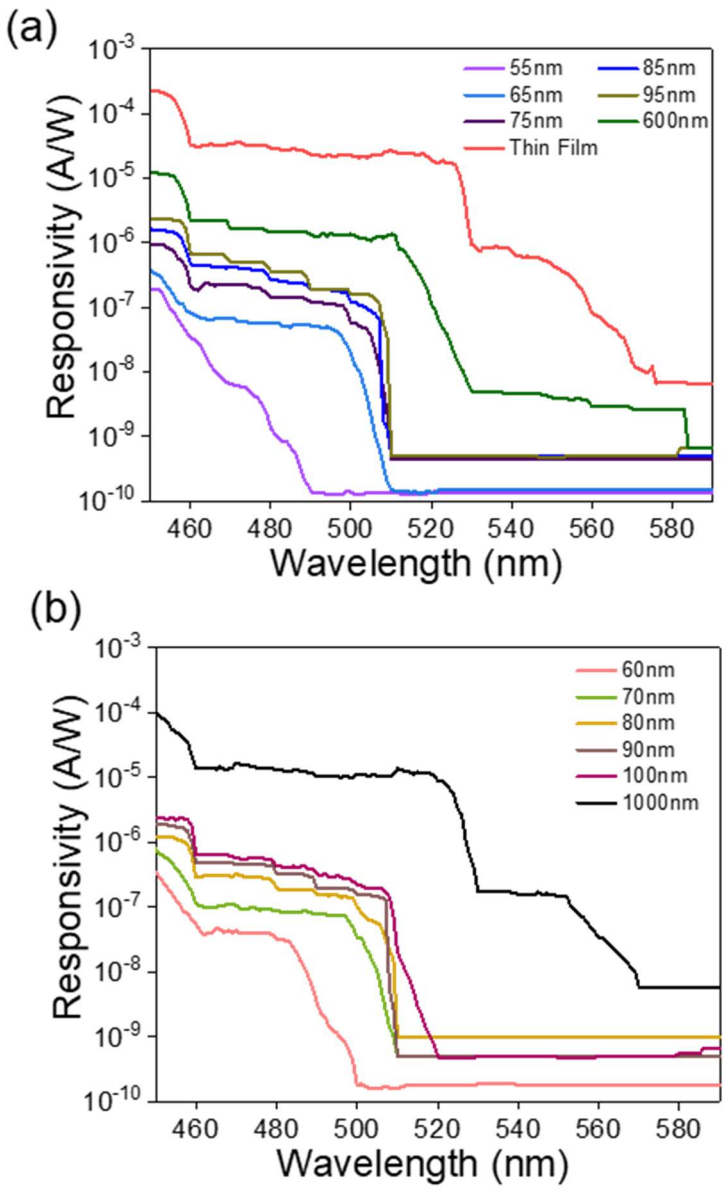

Figure 3-6: (a,b) The responsivities of the 13 photodetectors measured at a zero bias using a tunable monochromatic light source (adapted from [29]). The optical power at the sample was characterized separately using an integration sphere. The photocurrent was measured using a semiconductor parameter analyzer (Keithley 4200). The legend shows the nanopillar's diameter in each photodetector.

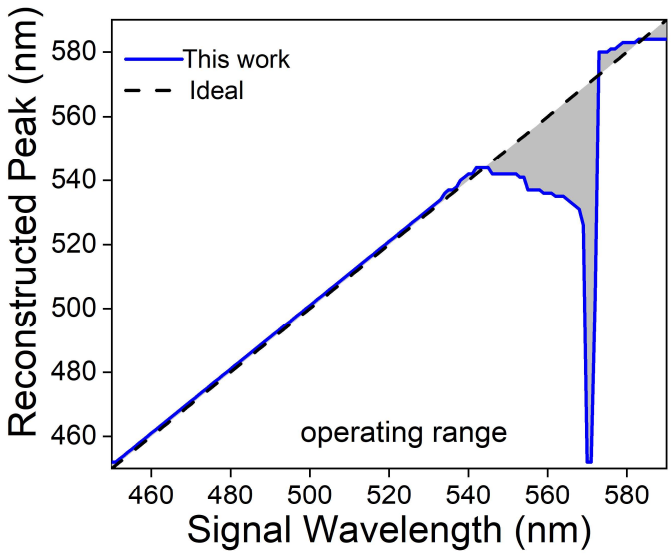

Figure 3-7: Determination of the spectrometer's operating range using an NNLS algorithm with a series of delta-function spectra between 450 nm and 590 nm. The shaded area from 541 to 590 nm indicates the wavelength range in which the reconstruction has a large error. The result implies an operating range from 450 nm through 540 nm.

3.8 Reflectance Spectroscopy Feasibility

Next, we demonstrated the viability of the monolithically integrated LED light source in the configuration of reflection spectroscopy. Figure 3-8 shows the schematic of experimental setup to demonstrate the proof-of-concept using reflection mode spectroscopy. We tested two configurations. In one configuration, we placed a mirror approximately 4 cm from the sample, as shown in Figure 3-9(a). In the second configuration, we inserted a notch filter (Thorlabs NF-533-17) with a center wavelength of 533 nm and a linewidth of 17 nm between the mirror and the sample as shown in Figure 3-10(a). No other optics were used. In the experiment, the LED emission emanated from the sample passed through the notch filter, was reflected from the mirror,

and passed through the filter another time before being absorbed by the photodetectors. The returned spectra were measured by a commercial spectrometer and shown by the dashed curve in Figure 3-9(b) (without placing a notch filter), and Figure 3-10(b) (with a notch filter).

To reconstruct the reflected spectrum, we used an NNLS algorithm enhanced by the orthogonal matching pursuit (OMP) method to address a full range of spectral components simultaneously at multiple photodetectors [30]. We used a Gaussian basis with a 12 nm linewidth and a maximum iteration value of 141, which is equivalent to the number of wavelengths used to characterize the response function of photodetectors. The reconstructed spectra for both configurations are shown in Figure 3-9(b) and Figure 3-10(b) with the blue solid curve which reasonably matches the spectrum measured by a commercial spectrometer (black dashed curve). The spectral reconstruction in this work is an underdetermined problem with only 13 photocurrent values available. As a result, only an approximate instead of an exact spectrum can be reconstructed in Figure 3-10(b).

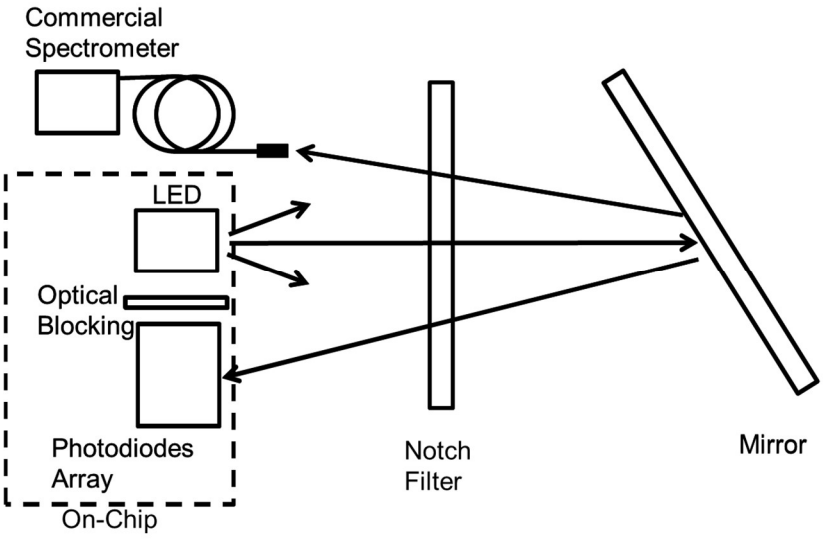

Figure 3-8: Experimental setup to show the feasibility of using our spectrometer chip for chemical analysis in reflection spectroscopy configuration.

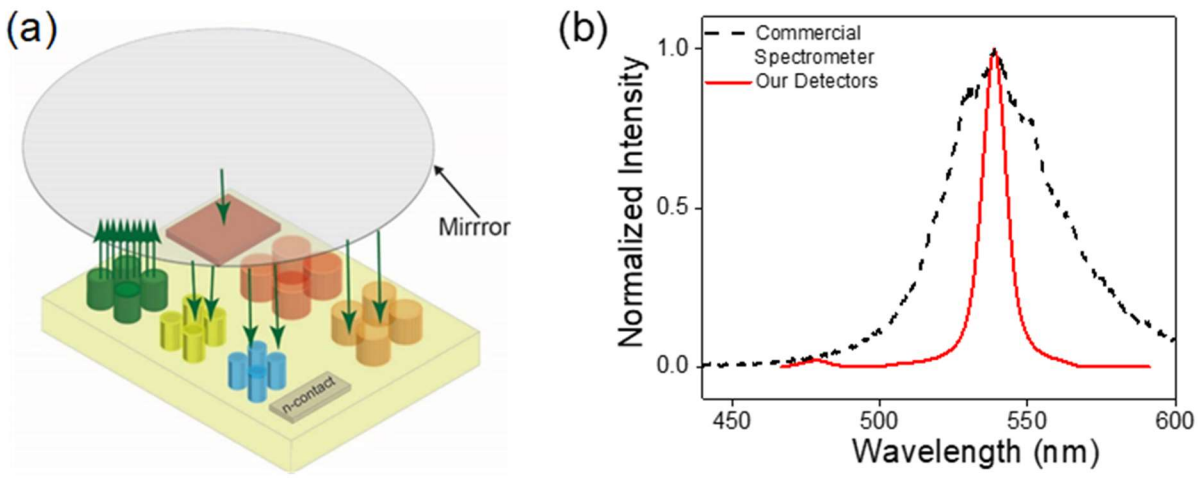

Figure 3-9: (**a**) The experimental configuration to demonstrate the feasibility of the monolithically integrated LED light source in reflection spectroscopy. We used a mirror, imitating as a chemical. To demonstrate reflection spectroscopy. The distance between the mirror and the chip is 4 cm. No external optics were used. (**b**) The LED emission (black dotted curve), captured by Ocean Optics HR2000, and the reconstructed spectrum (red solid curve) using an OMP-enhanced NNLS algorithm.

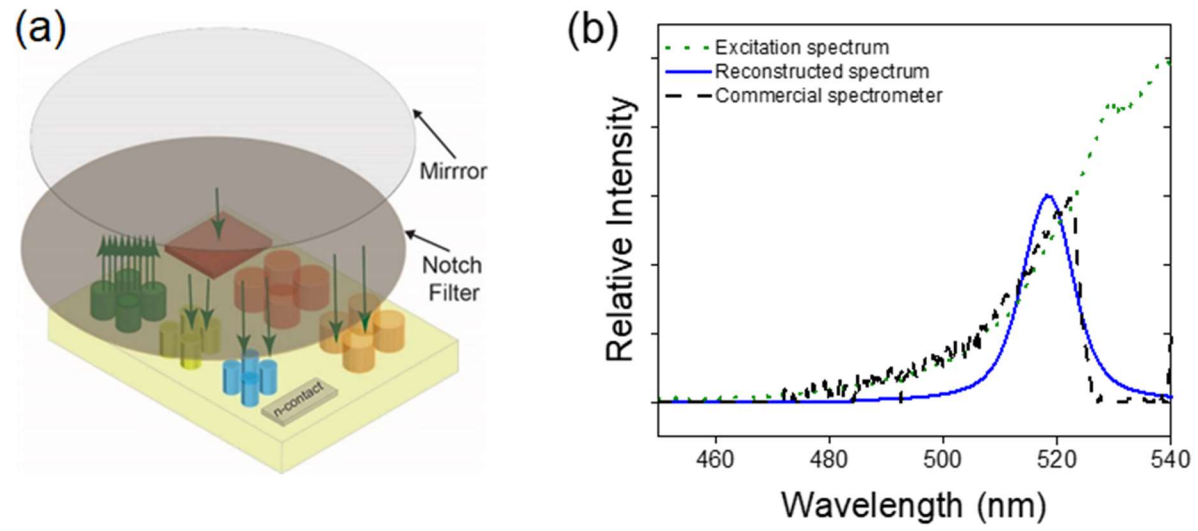

Figure 3-10: (**a**) The experimental configuration to demonstrate the feasibility of the monolithically integrated LED light source in reflection spectroscopy. A notch filter was used to modify the LED emission. Together with the mirror, the reflected spectrum simulated an analyte absorbing around 533 nm with an absorption linewidth of 17 nm. The distance between the mirror and the chip is 4 cm. No other optics other than the two shown were used. (**b**) The LED emission (green dotted curve), the reflected spectrum (black dashed curve) just above the chip captured by Ocean Optics HR2000, and the reconstructed spectrum (blue solid curve) using an OMP-enhanced NNLS algorithm

3.9 Discussion

The reconstructive spectrometer chip designed, fabricated, and characterized in this work used a series of wavelength-selective photodetectors that exhibited a very weak dependence on the incident angle of light. As a result, collimation optics were not necessary for the functionality of the device. It was evident that the responsivities used in the spectral reconstruction in Figure 3-10(b) were measured using a completely different illumination profile. The responsivities were measured using a monochromatic light focused onto the sample while the reflected spectrum in Figure 3-10 diverged significantly due to the incoherent nature of the LED emission. The results highlighted an important advantage of the reconstructive spectrometer using absorptive spectral filters, which in our case were built in as part of the photodetectors. The optionality of the collimation optics can enable a miniaturized spectrometer in an ultrathin form factor. One can also opt to integrate focusing lenses to increase the signal-to-noise level and/or to easily enable an array of spectrometers on the chip for hyperspectral imaging.

The spectroscopic operating range in this work can be expanded by reducing the correlation between the photodetectors' responses, e.g., by enhancing the absorption in the long-wavelength region. When some photodetectors' responsivities are very low, they effectively become non-participating and correlated, as 0 and 0 are always correlated. The enhanced absorption can allow more photodetectors to participate in the reconstruction algorithm. This was shown in [29].

The optical blocking in this work was fabricated using an enamel-coated PET sheet manually attached to the spectrometer chip. A more scalable approach can be to use a MEMS (microelectromechanical system) process. For example, when patterning the nanopillar arrays, one can keep a checkerboard pattern of GaN unetched. These wall-like structures can then be heightened using PDMS (polydimethylsiloxane) which can be subsequently coated with a thin

metal layer to be rendered light-blocking. As the LED is simply a forward-biased photodetector in our design, a photodetector array separated by optical blocking structures can enable a reconfigurable excitation spectrum for more versatile applications.

3.10 Conclusions

In summary, we designed, fabricated, and demonstrated the feasibility of an optics-free spectrometer chip with a monolithically integrated LED light source. With 13 photodetectors, we successfully achieved spectroscopic functionalities in the wavelength range between 450 nm and 540 nm. We also demonstrated the feasibility of reflection spectroscopy using the on-chip LED source and photodetectors simultaneously. The optical blocking structure successfully suppressed the direct capture of the LED emission by the photodetectors, which were as close as 0.3 mm from the LED. Finally, we showed that the spectrometer chip in this work did not require any external optics for its functionality. Therefore, the proposed spectrometer design can potentially enable a miniaturized spectroscopic system in an ultrathin film platform which can enable new opportunities, e.g., a wearable spectrometer chip to monitor physiological conditions in real-time.

.

Chapter 4 Designing an Ultrathin Film Spectrometer Based on III-Nitride Light-Absorbing Nanostructures[3]

In this chapter, a spectrometer design enabling an ultrathin form factor is proposed. Local strain engineering in group III-nitride semiconductor nanostructured light-absorbing elements enables the integration of a large number of photodetectors on the chip exhibiting different absorption cut-off wavelengths. The introduction of a simple cone-shaped back-reflector at the bottom side of the substrate enables a high light-harvesting efficiency design, which also improves the accuracy of spectral reconstruction. The cone-shaped back-reflector can be readily fabricated using mature patterned sapphire substrate processes. Our design was validated via numerical simulations with experimentally measured photodetector responsivities as the input. A light-harvesting efficiency as high as 60% was achieved with five InGaN/GaN multiple quantum wells for the visible wavelengths. (This work was done in collaboration with Juhyeon Kim.)

4.1 Introduction

An absorption-based spectrometer utilizes a series of optical filters with different absorption responses. The absorption responses from any two optical filters need to have minimal spectral correlations. Once this condition is satisfied, the photocurrent I_i generated from the i-th photodetector/optical filter combination can be determined by,

[3] J. Kim, S. Cheekati, T. Sarwar, and P. Ku, "Designing an Ultrathin Film Spectrometer Based on III-Nitride Light-Absorbing Nanostructures," Micromachines **12**(7), 760 (2021). JK: simulations and analysis; SC: spectral reconstruction analysis; TS: photodetector design and measurements.

$$I_i = R_{ij} \times P_j, \tag{4-1}$$

where P_j is the optical power at a wavelength λ_j absorbed by the photodetector, and R_{ij} is the responsivity, with a unit of A/W, of the i-th photodetector/optical filter combination at a wavelength λ_j. Once the responsivities of individual detection elements are measured, one can invert the above equation to obtain the optical spectrum P. In practice, the measured photocurrents include noise, and, thus, the above equation may not have a solution. However, one can seek a solution that minimizes the norm of the difference between the two sides of Equation 4-1. This is a topic of immense interest in recent years [188–192]. As the spectra of interest are often not arbitrary, the accuracy of spectral reconstruction can be improved with a set of constraints, e.g., by assuming the optical spectrum consists of a series of Gaussian spectra with a finite linewidth. The estimation approach also allows one to recover important spectral information even when the number of photodetectors is less than the number of wavelengths [193–196].

The photodetector/optical filter combination can be further simplified by a photodetector design with an intrinsic tunable absorption response. For example, indium gallium nitride (InGaN) dot-in-the-wire (DIW) light-absorbing nanostructures have been shown to exhibit a tunable absorption response by changing their geometric parameters, such as diameter and shape [197]. The intrinsic strain stored in the InGaN DIW region grown on GaN due to lattice mismatch is relaxed near the surface of the nanostructure, modifying the electronic band structure and thus the absorption response. Lithographically defined InGaN DIW nanostructures can tune their absorption cut-off wavelengths from ultraviolet through near-infrared spectra [186,198–200].

Previously, an absorption-based spectrometer using an InGaN DIW nanostructure directly integrated with a GaN pn junction was demonstrated [201]. Such a design enables an extremely compact construction, eliminating the need for a separate silicon photodiode array. However,

InGaN DIW nanostructures have very limited light absorption in the visible wavelength range due to a small absorption length. Significantly increasing the InGaN thickness will not be feasible due to a large lattice mismatch with GaN.

In this chapter, three major aspects were analyzed to visualize the improvement in the current device design. 1. We theoretically evaluated the absorption coefficient of nanopillars using Nextnano^3 simulation tool. 2. This work proposed a simple strategy, utilizing the well-established sapphire substrate patterning process to greatly enhance the absorption efficiency while maintaining a large acceptance angle for the incident light. We also demonstrated that spectroscopic performance can be significantly enhanced. Simulations and analysis for this part were carried out by Juhyeon Kim. 3. The electrical characteristics of the photodetectors were studied thoroughly by employing equivalent circuit models to investigate any room for improvement in the performance of our spectrometer.

4.2 Calculation of Absorption Coefficient

Nextnano is a simulation software for electronic and optoelectronic semiconductor micro/nano devices [202–204]. It provides theoretical models for understanding designing, and improving the electronic and optical properties of nanostructures with any arbitrary arrangement of geometries and materials. Here, Nextnano^3 tool was employed to theoretically calculate the absorption coefficient of nanopillars with different diameters. The program process flow and used equations model are shown in Appendix A. The simulated structure is a GaN nanopillar that contains a 2.5 nm In_xGaN_{1-x} quantum well (QW) embedded 10 nm below the top surface with $x = 0.32$ i.e., the indium composition. The nanopillar was surrounded by air. A nanopillar structure with 40 nm diameter is shown in Figure 4-1 as an example. The numerical model was based on continuum elasticity approximation that minimizes the total strain energy in the nanopillar. A 6-

band $k.p$ model was used to solve the strain-involved electronic band structure and energy states in the conduction (CB) and valance band (VB) [205–209]. The interaction between the CB and the VB was ignored. The calculated band structures are plotted in Figure 4-2(a) and (b) in the x-direction at the top and bottom of the InGaN layer, respectively. The 1st electron and hole Eigen energy states are also labeled. A total of 100 Eigen values in both CB and VB were calculated by solving Schrödinger's equation under the effective mass approximation and shown in Figure 4-2(c) and (d), respectively. Wavefunctions and wavefunction overlap integrals were also calculated for all those Eigen states. A MATLAB code was used to calculate the absorption coefficient for different nanopillar diameters using imported data files from Nextnano[3]. Absorption rates were calculated only for the QW region since the barrier material has a higher bandgap and does not participate in the optical process because the photon energies are much higher. The Eigen values and Eigen functions with Spatial overlap only in the QW region were considered. MATLAB algorithm for carrying out this analysis is reproduced in Appendix B. Figure 4-3 shows the results. The absorption pattern for each nanopillar is dissimilar to the other. This diversity in the signature patterns defines the resolving power of a reconstructive spectrometer and is thus very important for finding the most 'plausible' solution.

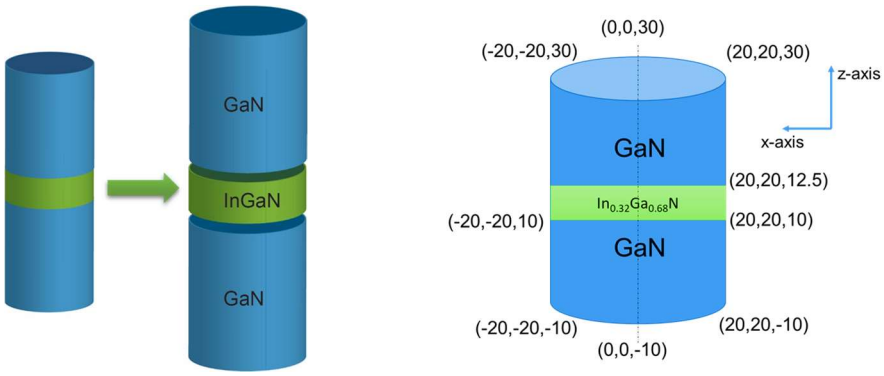

Figure 4-1: The schematic of the In_xGaN_{1-x}/GaN nanopillar structure simulated in Nextnano[3] with its coordinates. Nanopillar has a diameter of 40 nm with 32% Indium content.

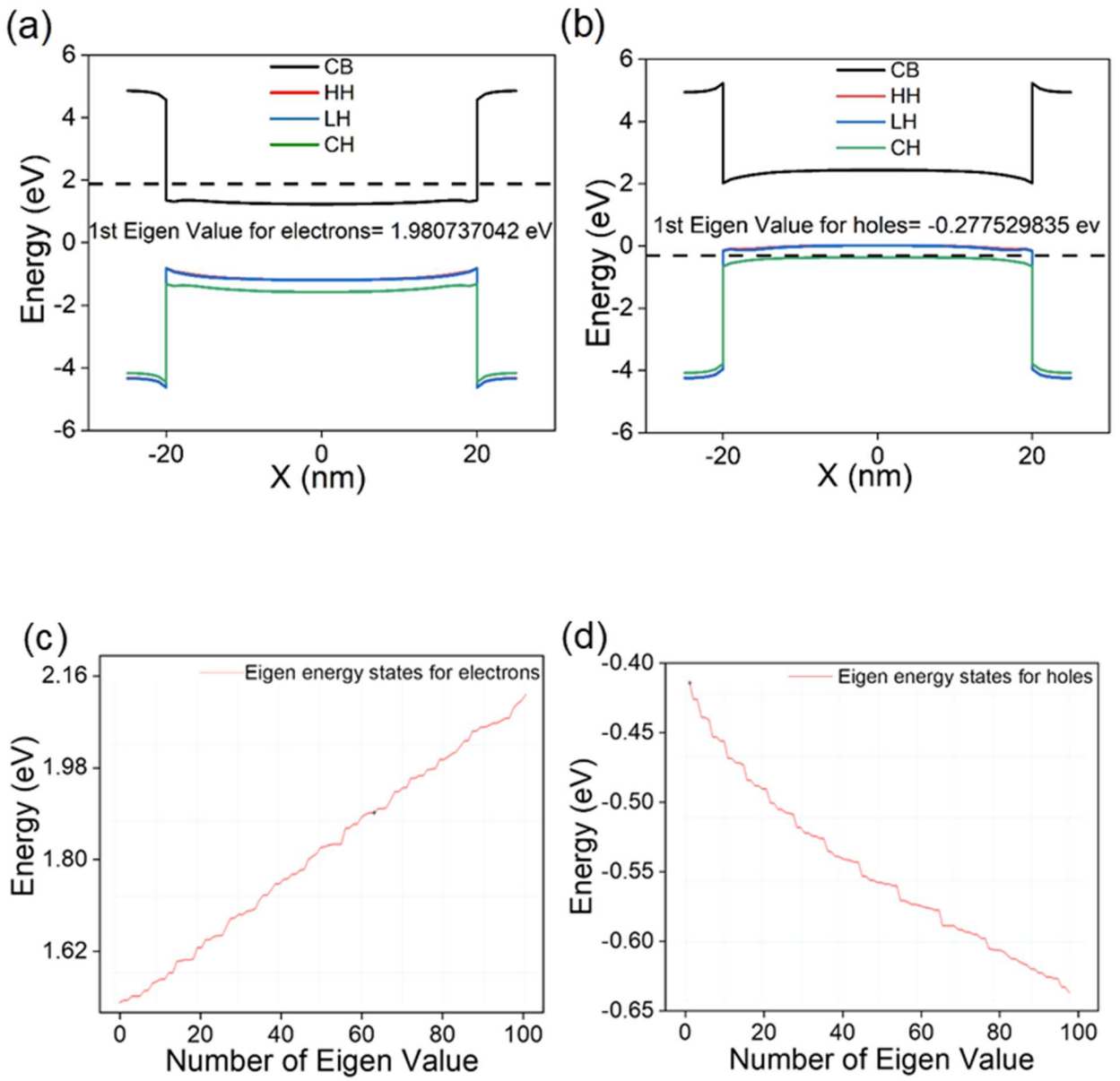

Figure 4-2: (a) The electronic band structure in the x direction at the top of the QW layer and the corresponding first electron Eigen state. (b) The band structure at the bottom of the QW layer and the corresponding first hole Eigen state. Eigen energy states were calculated by solving Schrödinger's equation under the effective mass approximation in (c) conduction band, and (d) valance band.

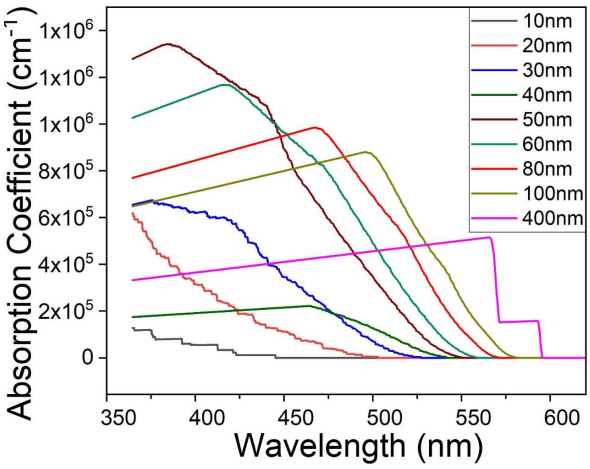

Figure 4-3: The absorption coefficient response curves of InGaN/GaN nanopillars with various diameters at different wavelengths. The absorption rates were calculated using Nextnano[3] simulation tool.

4.3 Device Design using Finite-Difference Time-Domain (FDTD) Simulations

Although silicon is a ubiquitous and often preferred material for a wide range of electronic and optoelectronic applications, silicon's light absorption properties cannot be easily tuned, which is necessary for an absorption-based spectrometer. To address this limitation, the proposed spectrometer design consists of an array of GaN-based photodiodes. Individual photodiodes' absorption cut-off wavelengths are tuned by changing the nanopillar structures' diameters. The underlying principle for absorption tuning is local strain engineering [210]. When the compressive strain in the InGaN multiple quantum well (MQW) regions is relaxed at the nanopillars' sidewalls, the absorption band-edge is blue shifted due to the reduction of the quantum-confined Stark effect (QCSE). Local strain engineering has been previously applied to monolithically integrate red, green, and blue-light-emitting diodes (LEDs) on the same substrate using a single epitaxial stack [211–213]. The same principle has also enabled the realization of an absorption-based

spectrometer [30]. InGaN absorbs light efficiently, exhibiting a large absorption coefficient >104/cm. However, the lattice mismatch with GaN limits the total InGaN thickness to a few tens of nanometers, resulting in a low absorption efficiency and photodiode responsivity. To increase the light-harvesting, one can employ light trapping structures, such as optical cavities, a roughened surface plus a back-reflector, plasmonic structures, and photonic crystals. In this work, we investigated a simple strategy using a metal-coated patterned sapphire substrate (pss) acting as a back-reflector and light scatterer to deflect the incident light in order to increase the optical path. The process of fabricating a pss is well established and widely used in the LED industry [214]. As a result, the proposed pss as a wafer-scale light trapping structure can be fairly economical to manufacture. In the current design, we consider the pattern to be fabricated on the bottom side of the sapphire substrate, as a laser lift-off (LLO) process to separate the GaN layer from the pss substrate is still in development [215–217]. In the future, it may be possible for the photodiode epitaxial stack to be grown directly on a pss, which can then be coated from the underside with a metal back-reflector after substrate removal. In addition to the back-reflector, we also included optional top TiO_2 grating, which we found to further enhance light absorption in large-diameter nanopillar structures. (This study was done by Juhyeon Kim.)

Figure 4-4 shows the schematic of the proposed device structure. For the pss, we considered an array of cone-shaped, silver (Ag)-coated structures with adjustable sidewall angle φ, which can be tweaked by the resist reflow condition and the subsequent transferring of the resist pattern into the sapphire via dry etching [218]. We fixed the base diameter of the cone and assumed the backside of the sapphire substrate was polished before the cone structures were formed. The photodiode consists of an array of nanopillars. The epitaxial stack of the nanopillar is a typical LED structure with an InGaN/GaN MQW active region sandwiched between a GaN pn junction.

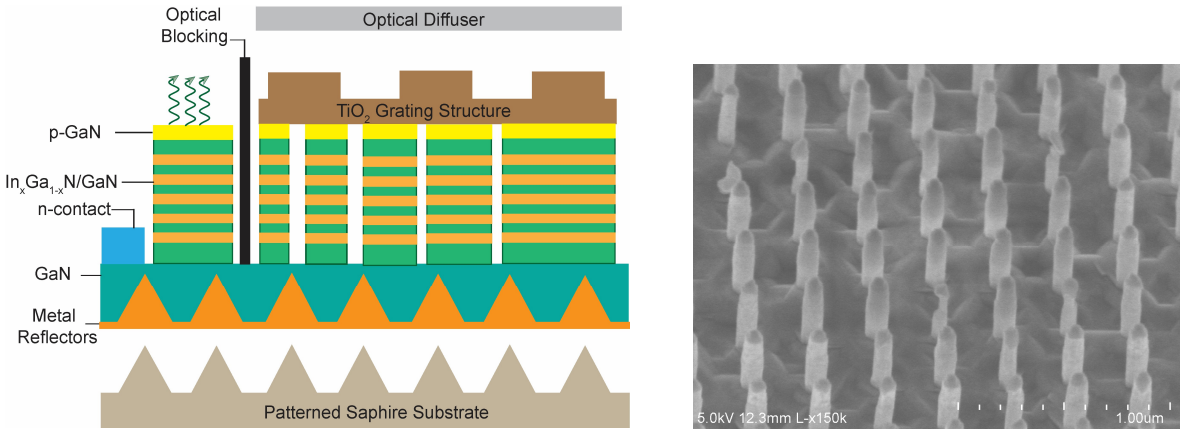

Figure 4-4: Schematic of the proposed wavelength-selective photodetector. The structure consists of three parts: the light absorbing InGaN/GaN MQW active region, the photodetector p-type (ITO, Ni/Au) and n-type contacts, and the light-trapping structure consisting of the silver (Ag)-coated cone-shaped back-reflector and the top TiO_2 photonic crystal (PhC) layer. The InGaN active region and the GaN pn junction are formed by lithographically patterning a thin-film structure of the same epitaxial stack, as shown by the scanning electron micrograph on the right, with an array of InGaN DIW nanopillars with a diameter of 80 nm before filling the space between the nanopillars with the insulating Si_3N_4.

The nanopillar's diameter D determines the active region's absorption cut-off wavelength. In this work, we considered five pairs of 2.5 nm InGaN/12 nm GaN MQWs with an emission wavelength of 590 nm at room temperature. The absorption cut-off wavelength decreased with the nanopillar diameter and became 485 nm with a nanopillar diameter of 50 nm. To complete the photodiode, the nanopillars were first coated with 50 nm of SiN_x as the insulator, and the voids were filled and planarized by SiO_2. The p-type contact consists of 5 nm each of Ni and Au plus a 200 nm-thick indium–tin–oxide (ITO) as the current spreading layer. The device fabrication and photodiode characterizations were previously reported in Ref. [219].

To evaluate the light-harvesting efficiency (LHE), which we defined as the fraction of light intensity absorbed by the InGaN active region in the wavelength range 20 nm above the cut-off

wavelength, we used finite-difference time-domain (FDTD) simulations with a periodic boundary condition (performed by Juhyeon Kim). We considered an unpolarized incident light at an angle θ. We included the entire epitaxial stack, including the metal layers, and assumed a transparent Ni layer. After thermal annealing of the p-type contact in air at a high temperature, the Ni layer transformed into a transparent NiO. Although the absorption in InGaN depends on the wavelength as shown in Figure 4-3, we assumed a constant absorption coefficient of 10^5 cm^{-1} for simplicity. This assumption is justified because we are mainly interested in the relative improvement in absorption after introducing the light-trapping structure. We considered five different nanopillar diameters: 50 nm, 100 nm, 200 nm, 1000 nm, and thin film, corresponding to the absorption cut-off wavelengths of 485 nm, 518 nm, 536 nm, 570 nm, and 590 nm, respectively.

4.3.1 Results and Discussions

We first determined the optimal cone angle φ for the back-reflector. We focused on the smallest diameter nanopillar array, as it has the lowest LHE. The edge-to-edge spacing between two adjacent nanopillars was fixed at 50 nm for all nanopillar arrays. This spacing was chosen because it can be readily patterned using modern lithographic tools. Figure 4-5 compares the relative LHE as a function of the cone angle. It can be seen that the LHE peaks at a cone angle range between 32º and 37º. We fix $\varphi = 33^0$ in the following discussions.

Next, we considered a design with a higher density of nanopillars and added a TiO_2 two-dimensional grating structure on top of the GaN nanopillar array. We also proposed to grow the epitaxial structure on a patterned sapphire substrate (pss) to increase the optical path length through the MQW region. These strategies can significantly increase the absorption efficiency, as shown in Figure 4-5, determined using finite-difference-time-domain simulations (in collaboration with Juhyeon Kim).

The absorption responses of different photodetectors in an absorption-based spectrometer need to be uncorrelated. In our design, the correlation is removed by varying the absorption cut-off wavelength. photodetectors' LHEs.

Finally, we examined how the improved LHE impacts the spectrometer's performance. We considered 14 photodetectors with absorption cut-off wavelengths varying from 485 nm to 590 nm. Starting from the experimentally measured responsivity curves for these detectors, we estimated the new responsivity matrix R based on the calculated LHEs. To compare the spectral reconstruction's performance, we inputted a monochromatic light $\delta(\lambda)$, varied its wavelength λ from 460 nm to 590 nm, determined the theoretical photocurrents $I_p = R \times \delta(\lambda)$, and calculated the peak positions of the reconstructed spectra P using the non-negative least square (NNLS) algorithm with an L_2 norm $\| \cdot \|_2$ on the following inequality [49]:

$$\min_{P \geq 0} \|I_P - RP\|_2^2. \tag{4-2}$$

The result is shown in Figure 4-6. Without the LHE enhancement, the spectral reconstruction has a large error between 540 nm and 570 nm. The cone reflector increases its LHE by more than 10 times, resulting in a much more accurate spectral reconstruction. Further improvements are expected by increasing the number of photodetectors in the long wavelength range and the level of responsivity with improved electrical characteristics.

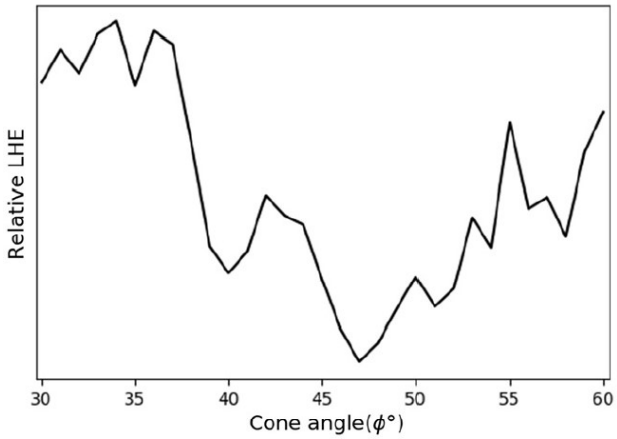

Figure 4-5: The relative LHE as a function of the cone-shaped Ag back-reflector's sidewall angle φ calculated using 2D FDTD simulations. The nanopillar diameter is 50 nm. The edge-to-edge spacing between two adjacent pillars is 50 nm.

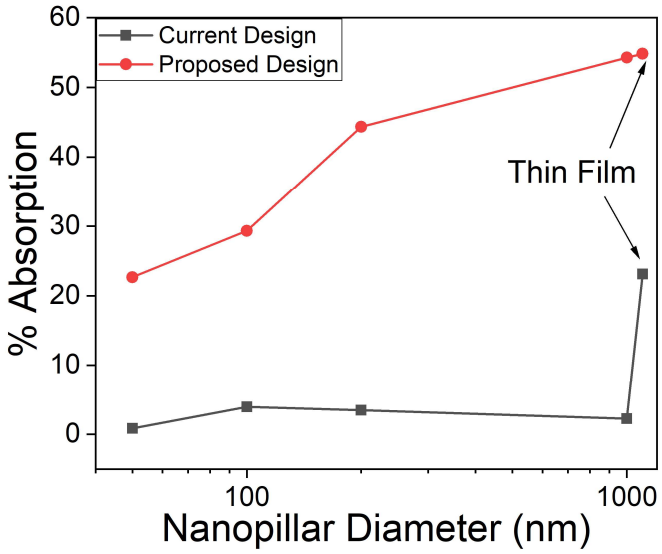

Figure 4-6: LHEs of various photodetectors with different nanopillar diameters for an unpolarized, normally incident light. The absorption cut-off wavelengths are 485 nm, 518 nm, 536 nm, 570 nm, and 590 nm in the order of the nanopillar diameter. The LHE is defined as the fraction of light intensity absorbed by the InGaN active region in the wavelength range 20 nm above the cut-off wavelength. For each photodetector, the LHEs for different light-trapping designs are also shown: "prior result" corresponds to the experimental device that was previously reported without any light-trapping structure and with a low nanopillar fill factor. Proposed design contains a high fill factor, metallic, and TiO_2 grating corresponds to the complete light-trapping structure shown in Figure 4-4.

4.4 Electrical Characteristics of Nanopillar pn Junction Diode

In this section, we studied the electrical characteristics of the photodiodes comprising of nanopillars with diameter 55 nm to thin film. Current density-voltage $(J-V)$ measurements were performed at room temperature and under dark conditions using Keithley 4200 semiconductor parameter analyzer. We fitted the experimental $(J-V)$ curves as shown in Figure 4-7(a), using an equivalent circuit model, which is also shown in Figure 4-7(b). The current equation of an ideal diode is given by Shockley diode equation [220–224] and can be described as:

$$I = I_s exp\left(\frac{qV}{\eta k_B T}\right). \tag{4-3}$$

But a real diode has unwanted parasitic resistances for which the Shockley equation modifies as:

$$I - \left(\frac{V-IR_s}{R_p}\right) = I_s \exp\left(q\left(\frac{V-IR_s}{\eta k_B T}\right)\right), \tag{4-4}$$

where R_s represents the series resistance that includes both the contact resistance and the bulk resistance through the nanopillar. R_P represents the shunt resistance due to surface leakages. η denotes the ideality factor. We used a MATLAB algorithm for fitting the $(J-V)$ curves using Equation 4-4. Here, we present the fitting results for only three photodiodes i.e. blue (55 nm), green (200 nm), and red (thin film) channels as shown in Figure 4-8 (a), (b), and (c), respectively. MATLAB code can be found in Appendix C.

When fitting R_s, we used the same resistivity ρ_s of the different photodiodes because they were fabricated on the same epitaxial wafer. We obtained R_s to be 230 Ω (red), 1.9×10^4 Ω (green), and 1.3×10^5Ω (blue); and R_P to be 10^9 Ω (red), 4×10^9 Ω (green), and 5×10^6Ω (blue). The smaller values of R_s compared to R_P suggest that dominant photo-generated carrier transport occurred through the p-MQW-n junction inside the nanopillar. Further observing the R_s and R_P values for

the three photodiodes, the difference between R_S and R_P is much smaller for the blue (55 nm) channel. In particular, R_P for the smallest diameter nanopillar array is three orders of magnitude smaller than that for the red and green nanopillars, suggesting a non-negligible surface leakage for the blue nanopillars. We attribute this enhanced surface leakage for the blue nanopillars to the plasma damage during the ICP-RIE rather than intrinsic to the epitaxial materials since all red, green, and blue photodiodes share identical device structures and fabrication processes. It has been reported that the penetration depth of the plasma damage due to the Ar and/or Cl_2 etch gas is approximately 50–100 nm [225–227], which is larger than the diameter of the blue-emitting nanopillars. Although the top region of the p-GaN was protected by the Ni etch mask, the plasma damage can still affect the sidewall of the InGaN active region, leading to large leakage current through surfaces and tunneling current through MQWs even if electrons and holes are transported through the inside of the nanopillar. This is further confirmed by the larger ideality factor η associated with the blue photodiode. A large ideality factor for the InGaN LED is often attributed to defect-assisted tunneling through the MQW region. From the $(J-V)$ curves, the ideality factor η was estimated to be 6.5, 9, and 28 for the red, green, and blue photodiodes, respectively. Meanwhile, the green nanopillar has a diameter larger than the plasma damage penetration depth. Therefore, the green photodiode exhibits better optical and electrical characteristics compared to the blue nanopillar.

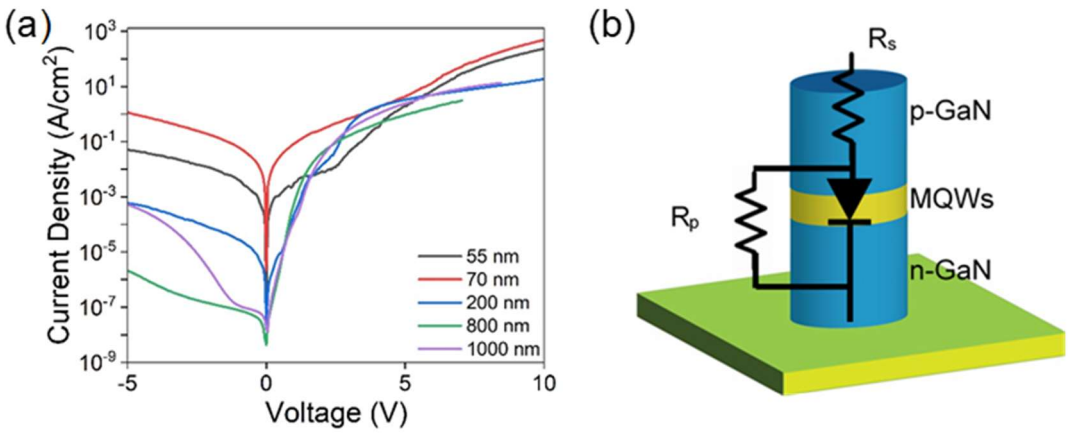

Figure 4-7: (a) Current density-voltage ($J-V$) curves of the pixels with nanopillars diameter 55 nm, 70 nm, 200 nm, 800nm, and 1000 nm. (b) Equivalent circuit model used to fit the $J-V$ curves.

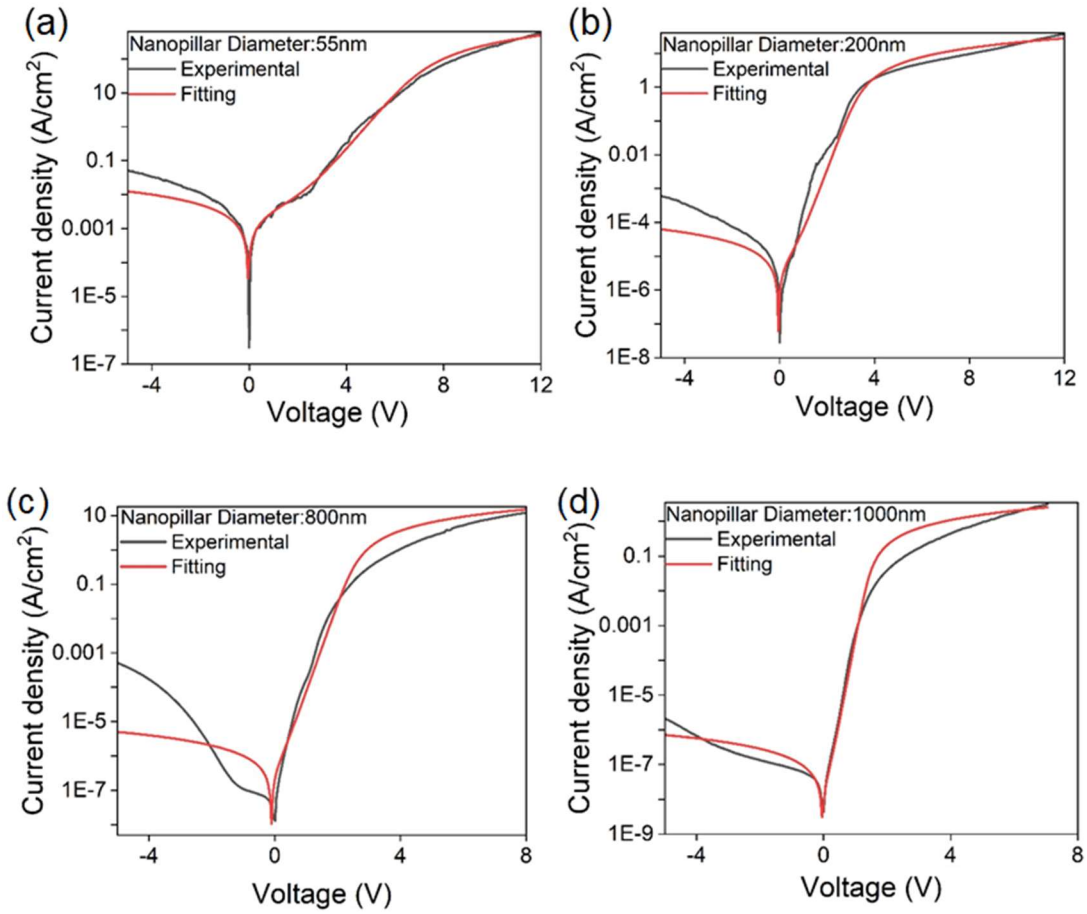

Figure 4-8: Fitting results of different current components *on* $J-V$ curves of (a) blue (55 nm), (b) green (200 nm), (c) amber (800 nm), and (d) red (1000 nm) nanopillar arrays.

Experimental responsivity measurements give strength to our discussion. The normalized responsivity of the smallest photodiodes was ~10X lower than that of the larger ones (Figure 2-7(b)). The difference is attributed to the surface recombination of photogenerated electrons and holes. To reduce the impact of plasma damages, one can increase the initial dimensions of the nanopillars after ICP-RIE and remove the outer 50 –100 nm of materials using a wet etch [226,227]. Surface passivation has also been shown to reduce the surface recombination [228,229]. Proper surface passivation is expected to bridge the gap in the future.

4.5 Conclusion

In summary, we have demonstrated an absorption-based on-chip optical spectrometer design based on a standard LED epitaxial stack. Using local strain engineering, the detector's absorption cut-off wavelength can be tuned geometrically by various lithographically defined arrays of nanopillars with different diameters. In spite of InGaN's high absorption coefficient, the lattice mismatch between InGaN and GaN limits the LHE of an InGaN/GaN MQWs to a few percentage points. To this end, we introduced a simple cone-shaped, Ag-coated back-reflector at the bottom side of the sapphire substrate to enhance the absorption. The interplay between the light scattering from the nanopillar array and the deflection from the cone shape significantly increases the absorption length through the active region. The LHE can be further enhanced with the addition of a thin TiO_2 film dotted with a two-dimensional TiO_2 periodic structure. Using a photodetector design previously demonstrated by experiments, LHEs of 20–60% can be obtained in the wavelength range of 450 nm–590 nm, which represents a 10-fold improvement on the prior results.

Not only can the Ag-coated cone-shape back-reflector be readily fabricated using mature patterned sapphire substrate processes, but the enhanced LHEs can lead to improved accuracy of spectral reconstruction in the situation when the number of photodetectors is smaller than the

degree of freedom or the number of independent wavelengths. Moreover, the LHE enhancement to the cone-shaped back-reflector and the top TiO_2 layer exhibit weak dependence on the incident angle of light, reducing the requirement to include collimation optics as is often needed for most spectrometers. Therefore, our spectrometer design can enable an ultrathin form factor for an array of spectrometers on the chip, which can be attractive for many mobile applications.

.

Chapter 5 Miniaturizing a Chip-Scale Spectrometer Using Local Strain Engineering and Total-Variation Regularized Reconstruction[4]

A wafer-thin chip-scale portable spectrometer based on reconstructive algorithms was proposed and demonstrated. 16 spectral encoders which simultaneously functioned as photodetectors were monolithically integrated with a chip area of 0.16 mm^2 using the principle of local strain engineering in compressively strained InGaN/GaN multiple quantum well structures. The built-in GaN pn junction enabled photocurrent measurements at a zero bias. A non-negative least square (NNLS) algorithm with total-variation (TV) regularization and a choice of kernel function was shown to deliver a decent spectral reconstruction performance in the wavelength range of 400 – 650 nm. The accuracies of spectral peak positions and intensity ratios between peaks were found to be 1.08% and 11.3%, respectively. No external optics such as collimation optics and apertures were used or necessary in the experimental demonstration, enabled by angle-insensitive light-harvesting structures, for an incident angle of light up to 30º, which included an array of nanopillar-shaped light absorbers and a cone-shaped back-reflector fabricated on the underside of the sapphire substrate. The small chip area together with a computationally efficient spectral reconstruction algorithm makes the proposed spectrometer especially suitable for wearable applications.

[4] T. Sarwar, C. Yaras, X. Li, Q. Qu, and P.-C. Ku, "Miniaturizing a Chip-Scale Spectrometer Using Local Strain Engineering and Total-Variation Regularized Reconstruction," Nano Lett. **22**(20), 8174–8180 (2022). TS: methodology, experiment, data analysis, and results interpretation; CY and XL: spectral reconstruction analysis under the supervision of QQ.

5.1 Background

Optical spectroscopy is one of the most important and widely utilized scientific techniques. A spectrometer measures an optical signal's spectrum, i.e., the relative power spectral density $P(\lambda)$ at different wavelengths λ. A visible-wavelength spectrometer is a versatile tool for applications in chemistry, life science, microbiology, food industry, biomedical sensing, lab-on-a-chip, environmental monitoring, pharmaceutical research, cosmetic industry, and quality control. A spectroscopic system consists of three parts: a light source for reference or fluorescence excitation, a series of spectral encoders to encode the optical signal from the sample, and one or more photodetectors to convert the encoded signal into the spectrum. The most common Czerny−Turner configuration[16] (e.g., in a monochromator) uses a grating to encode the signal's wavelength onto different spatial coordinates, which are subsequently measured by a linear photodetector array. The Fourier-transform spectrometer (e.g., FTIR) encodes the signal's autocorrelation using a variable delay line which is then converted into the signal's spectrum via the Fourier transform. The tunable light spectrometer (e.g., a tunable laser spectrometer; an oximeter in a smartwatch[136,181]) uses multiple LEDs or a tunable laser as the encoder to isolate the signal one wavelength at a time. However, this approach is not suitable for detecting an active optical signal such as that from fluorescence, chemi-, and electro-luminescence. The reconstructive spectrometer encodes the signal with multiple broadband spectral filters, $R_k(\lambda)$ where k is the index of the spectral encoder.[230] Each of the encoded signals is measured by a separate or integrated photodetector. The collective photocurrents $\{I_k\}$ are then used to reconstruct the spectrum, e.g., using a non-negative least square (NNLS) algorithm $P(\lambda)$: $\min_{P\geq 0}\|I - RP\|^2/2$. The reconstructive spectrometer has attracted intense research interests recently[29,30,64–66,40–42,44,55,61–63] because 1. Computational power per watt-dollar grows rapidly; 2. Spectral filters

can be highly compact and mass produced; 3. With machine learning and optimization advances, the spectrum can be efficiently reconstructed even with only a small number of encoders/photodetectors.[33,66,67] These features are especially attractive when miniaturizing a spectroscopic system.

In this chapter, a low-profile reconstructive spectrometer with only the thickness of the semiconductors and an operating range spanning the visible wavelength spectrum is reported. Visible spectrometers have broad applications in UV-VIS, fluorescence, and chemi-/electro-luminescence spectroscopy. In our design, the spectral encoders are based on wide-bandgap gallium nitride (GaN) semiconductors. As GaN semiconductors are an excellent light emitting material, monolithic integration of a reference or excitation light source on the spectrometer chip is possible and has been shown previously.[161] Heterogeneous integration with silicon transimpedance amplifier (TIA)[231] or monolithic integration of GaN TIA[232] have also been previously reported for GaN-based detectors.

The GaN-based spectral encoders were programmed using local strain engineering and had a very weak dependence on the incident angle of light[29], eliminating the need to condition the optical signal's angle distribution with collimation optics or an aperture. Computationally efficient machine learning methods were applied to further reduce the number of encoders needed and the chip area of the spectrometer without greatly sacrificing the spectral reconstruction performance. The result is an ultrathin-film form factor as illustrated in Figure 5-1 which is suitable for the integration with a lab-on-a-chip sensor for epidermal sensors, biochips, neuro- and endoscopic probes, internet-of-things, and environmental monitoring.

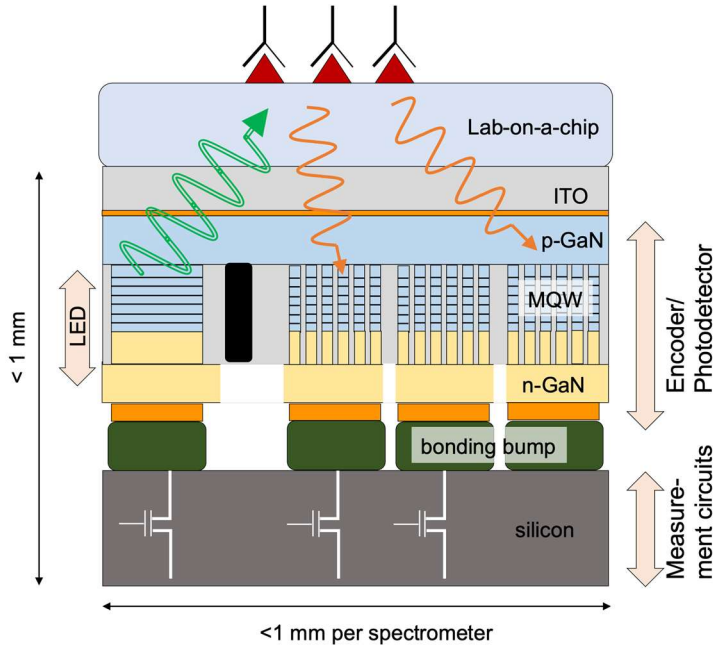

Figure 5-1: The conceptual illustration of the strategies used to achieve a low-profile ultrathin spectrometer chip based on the spectral reconstruction technique utilizing an array of GaN-based spectral encoders and photodetectors (This Work). As shown is the monolithic integration of the GaN reference or excitation LED and three spectral encoders which double as photodetectors. The programming of each spectral encoder is via local strain engineering using nanopillar-shaped InGaN/GaN multiple quantum wells (MQWs). The negligible angle dependence of the spectral encoders' absorption eliminates the need to condition the incident optical signal using collimation optics or apertures, enabling a direct integration on a lab-on-a-chip platform.

5.2 Device Design

A proof-of-concept chip-scale reconstructive spectrometer consisting of 16 spectral encoders was prepared (Figure 5-2; see Methods – Sample Preparation). Each encoder consisted of a pn junction and therefore also functioned as a photodetector biased at a zero voltage. Moreover, each encoder exhibited a unique spectral responsivity determined by the geometric shape of the constituent light absorbers. The encoder comprises of an array of nanopillar-shaped GaN nanostructural light absorbers. The strain profile of the InGaN/GaN multiple quantum wells

(MQWs) inside each nanopillar follows a hyperbolic secant (*hsec*) profile along its radial direction with a zero strain (fully relaxed) at the perimeter and an increasing strain (partially relaxed) toward the center.[116] When the nanopillar diameter is large, the strain at the center reaches its maximum value as determined by the lattice mismatch between InGaN and GaN. However, as the nanopillar diameter is on the order of several hundreds of nanometers or smaller, the strain at the center does not reach the maximum value. A smaller strain increases the bandgap and decreases the absorption cutoff wavelength, allowing the spectral response to be programmed simply by changing the nanopillar's diameter using lithography and etching.

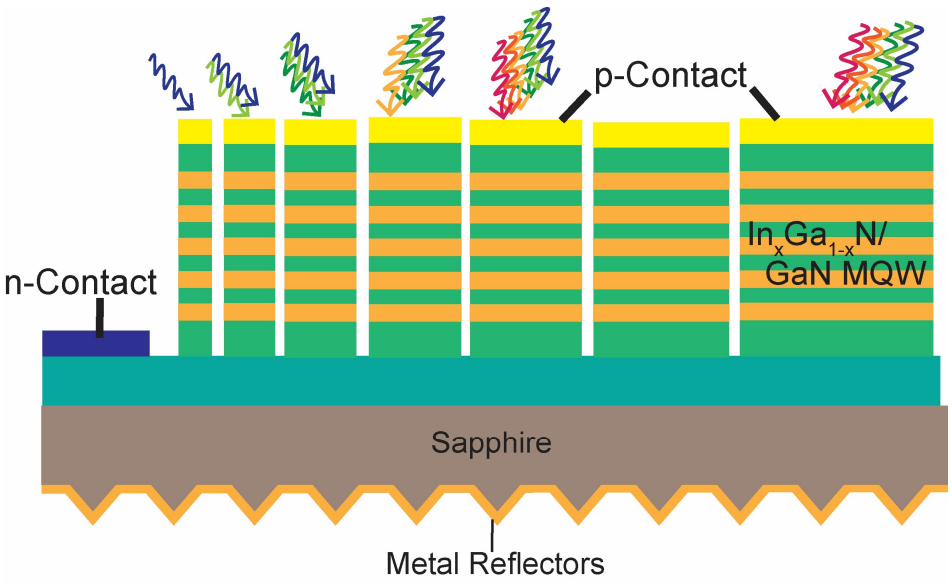

Figure 5-2: The device schematic showing the cross-sectional view of seven photodetector sections and the light-trapping back reflector. Each photodetector section consists of an array of nanopillar-shaped LEDs of a different diameter. The diameter programs the spectral response via local strain engineering.

5.3 Methods

5.3.1 Sample Preparation

The sample used in this study was grown on a 50-mm diameter double-side-polished (DSP), c-plane sapphire substrate by a commercial foundry (NovaGaN) using metal-organic chemical vapor deposition (MOCVD). The epitaxial structure was a simple LED heterostructure with GaN pn junction and five periods of $In_{0.32}Ga_{0.68}N$ (2.5 nm)/GaN (12 nm) multiple quantum wells (MQWs) in the active region. No electron blocking layer was added. The indium composition in the MQWs was controlled such that electroluminescence at room temperature showed red emission (λ=630nm at 7V). The sample started with the underside of the substrate with the preparation of dome-like light trapping structures. First, 500-nm thick SiO_2 was deposited on the front side of the substrate to protect the epi-layers. A photoresist (SPR 220) was then spin-coated on the backside of the substrate and patterned with an array of circles (4 μm diameter with an interval of 3 μm) using optical lithography. The resist was reflowed at 140^0 C for 6 minutes using a hot plate in air to achieve the desired shape. Next, the resist pattern was transferred to the sapphire substrate using inductively-coupled-plasma-reactive-ion-etching (ICP-RIE), resulting in a sidewall angle of ~32^0. The shape and sidewall angles of the dome-structures were verified by atomic force microscopy and shown in Figure 5-3. The scanning electron microscopy (SEM) image of the resulting dome-structures array is shown in Figure 5-4(a). After ICP-RIE, SiO_2 layer was removed using Buffered HF. A 300 nm thick Ag layer was deposited on the domes as the reflector.

The photodetectors with integrated spectral encoders were fabricated by a top-down process. Electron beam lithography and ICP-RIE were used to define the nanopillars of various diameters. To get a vertical sidewall and remove the plasma damage, a wet etch in a buffered KOH

solution (AZ 400K) was performed after the dry etch. The SEM images for the 60 nm GaN nanopillars are shown in Figure 5-4(b). After achieving cylindrical nanopillars with a height of 200 nm, the sample was planarized. A 500 nm SiO_2 was deposited using plasma-enhanced chemical vapor deposition (PECVD) followed by a 600 nm spin coating of polymethylmethacrylate (PMMA). After planarization, PMMA and SiO_2 were etched back using ICP-RIE with a subsequent ion milling to expose the tips of the nanopillars. Ion milling was used to avoid plasma damage on the circumference of the exposed nanopillars. Finally, the metallization for the electrical interconnects was carried out. We used 7 nm/7 nm Ni/Au layer for p-contact thermally annealed in air and 30 nm/100 nm Ti/Au for n-contact. All photodiodes share a common n-contact. Bright-field optical microscope images of the spectral encoders after metallization are shown in Figure 5-5. Pictures of the sample at the beginning of the process and the fabricated spectrometer device used in this work are also shown in Figure 5-6. The detailed fabrication process flows of nanopillars and the dome structures are shown in Figure 5-7 and Figure 5-8, respectively.

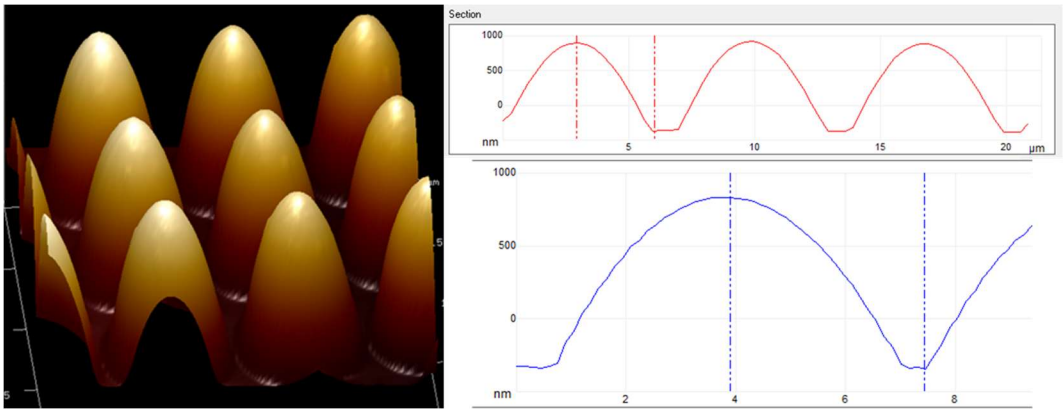

Figure 5-3: The 3D AFM image of cone structures fabricated on the backside of the sapphire substrate (left). Surface height histograms are also shown with a 20 µm scan length (top right). The bottom right scan is the zoom view of the center parabola. Scan shows a height of 2.074 µm giving a sidewall angle of 32º.

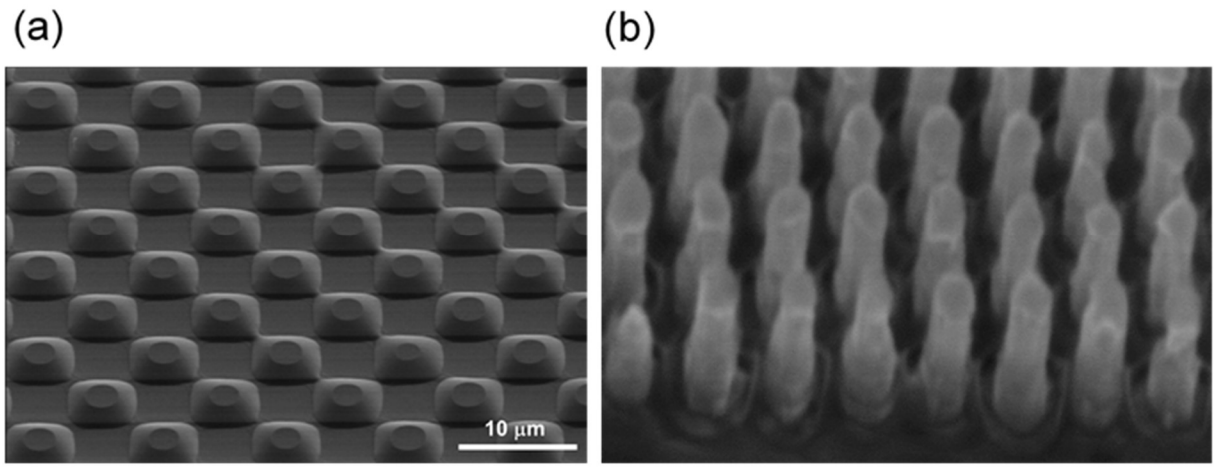

Figure 5-4: The scanning electron microscopy (SEM) image of a representative nanopillar array is shown on the bottom-left. The SEM bird's-eye view of the light-trapping back-reflector is shown on the bottom-right.

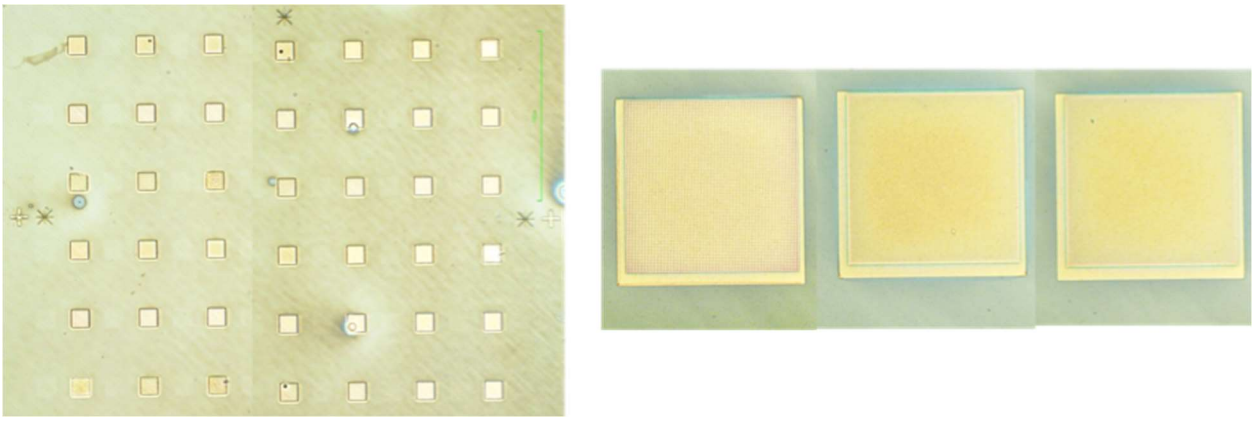

Figure 5-5: (Left) The bright-field optical microscope image of the array of spectral encoders, each with a size of 100µm x 100µm. The underside of the substrate is patterned with an array of cone-shaped light-scattering structures coated with silver. (Right) The zoom-in view of three encoders comprising of arrays of nanopillars of different diameters.

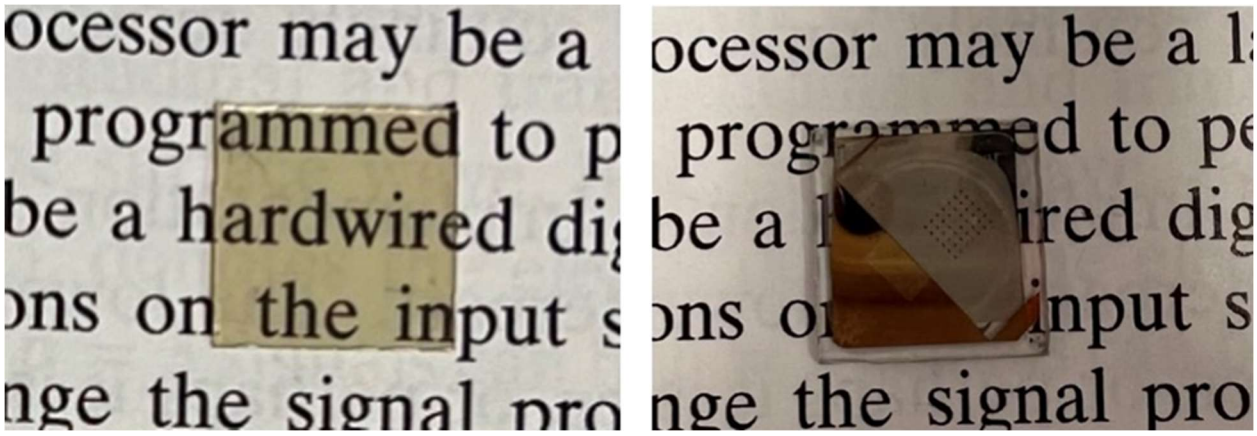

Figure 5-6: The starting sample (left) and the fabricated spectrometer device (right) used for the demonstration in this work. The array of dark squares on the right are the spectral encoders shown in Figure 5-5. The silver background is from the silver coating on the underside of the sapphire substrate. The dark color of the spectral encoders is the result of light absorption. The yellow-ish tint on the left is from the weak light absorption through the InGaN/GaN multiple quantum wells.

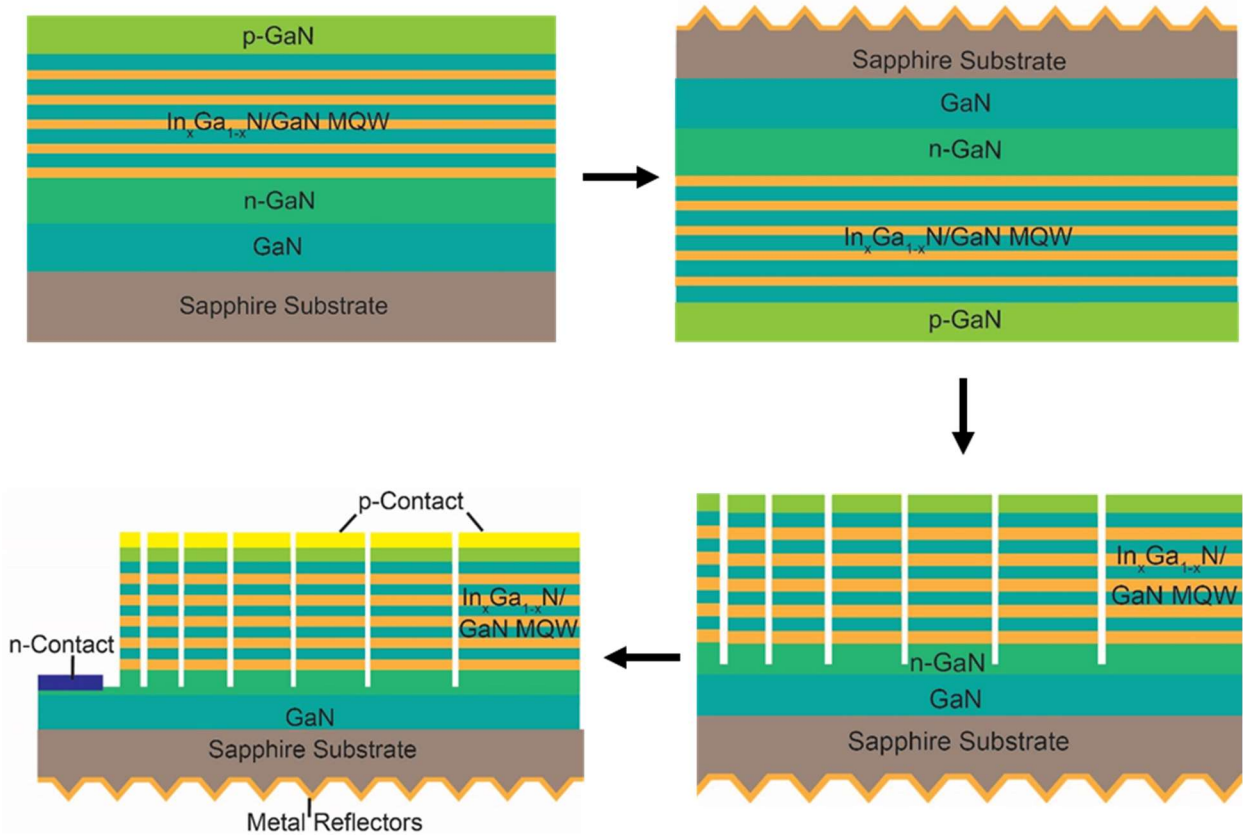

Figure 5-7: Spectral encoders' detailed fabrication flow using a top-down approach.

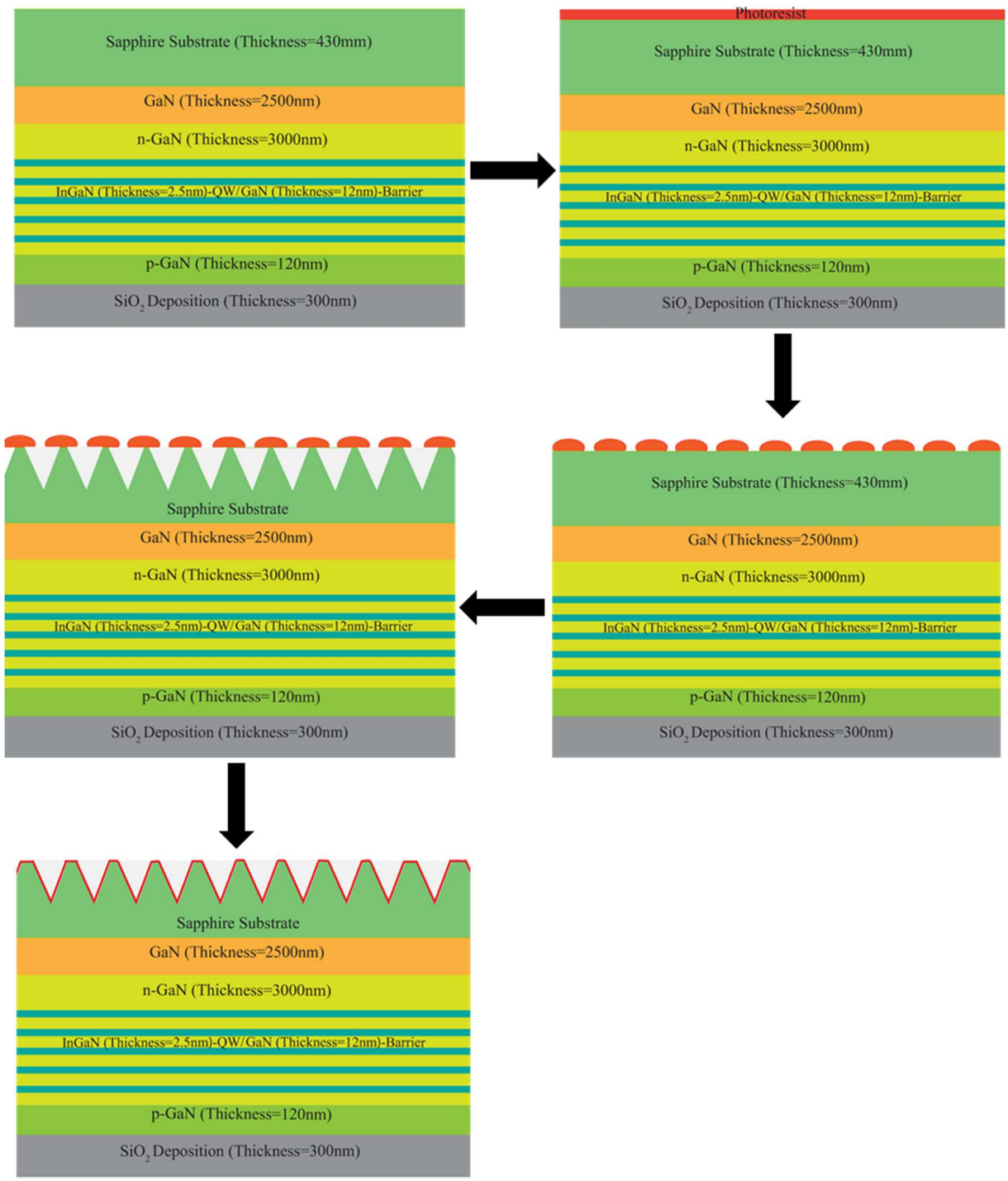

Figure 5-8: Fabrication process flow of cone-shaped structure on the sapphire substrate.

5.3.2 Optical Measurements

Each photodiode was characterized for its intrinsic response under the illumination of a monochromatic light in the spectral range of 400 nm to 700 nm with a step size of 1nm. We used a solar simulator (Abet Technologies) as the light source. The broadband spectrum was filtered through a monochromator (Acton 2500i, 0.500m focal length triple-grating) and impinged upon each photodiode via fiber optic cable. The photocurrent was measured at 0V using a current meter (Keithley 6482). The optical power of the impinged light was separately measured from a reference detector. The responsivity of each photodiode was calculated from the measured photocurrent and optical power of incident light. We also considered the estimated illumination area and the dimensions of each photodiode (including areas without nanopillars) in the responsivity calculations.

5.4 Responsivity-Results

Figure 5-9 shows the 16 encoders' responsivities $R_k(\lambda)$ measured at 0V with a 1-nm spectral resolution as a function of the nanopillar's diameter (see Methods – Optical Measurements). We also determined the operating wavelength range by using the NNLS algorithm with a monochromatic delta-function spectrum $\delta(f_0)$ as an input tuned from 400 nm through 700 nm. We calculated the photocurrents $I_k = R_k\delta(f_0)$ and applied NNLS to check how well $\delta(f_0)$ can be recovered. The reconstructed peak wavelength versus the input is plotted in Figure 5-10. The straight-line segment from 400 nm to 645 nm represents the operational window of the device.

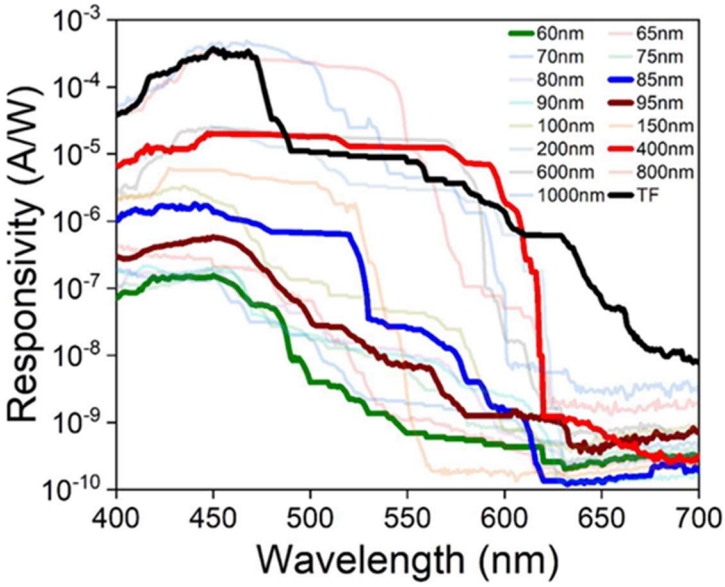

Figure 5-9: The responsivities of the 16 photodetectors measured using a tunable monochromatic light (see Methods – Optical Measurements). The legend shows the diameter of the nanopillar in each photodetector, ranging from 60 nm to thin film (TF). The responsivity is not normalized to the active region area but rather to the chip area.

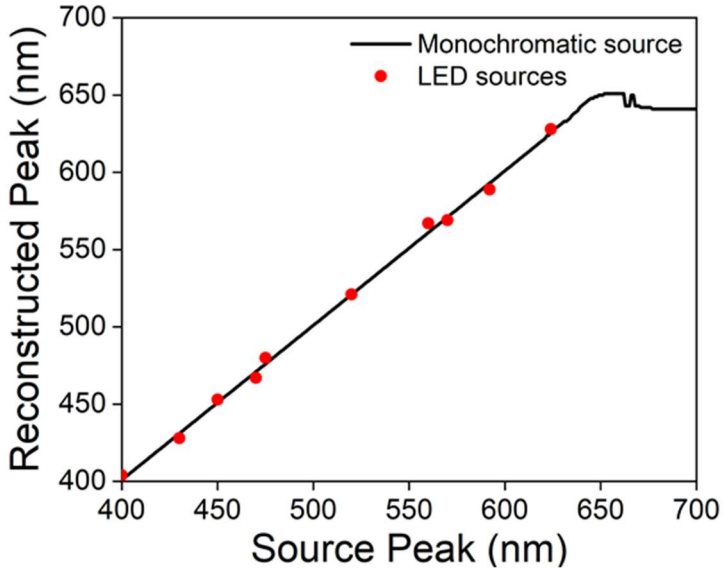

Figure 5-10: The spectrometer's spectral reconstruction accuracy in the range of 400 nm to 700 nm, using both the monochromatic input (solid curve) and LED sources (dots). A diagonal section between 400 nm and 650 nm represents the spectrometer's operating range.

5.5 Dependence on Angle of Incidence

In a spectrometer, the encoders' spectral responses $R_k(\lambda)$ must remain constant under all measurement conditions for the reconstruction algorithm to correctly determine the spectrum. Thus the incident light's angle distribution is often conditioned in a reconstructive spectrometer, e.g., by letting it go through a pinhole or/and collimation optics. This is because the spectral response is generally sensitive to the incident angle of light. The external optical elements filter or/and fix the distribution of the incident angles but also increase the difficulty of miniaturizing the spectrometer, especially achieving a chip-scale device with a low profile. While on-chip aperture and coupler have been reported to address this limitation, these structures inevitably reduce the light-harvesting efficiency (LHE) and the signal-to-noise ratio (SNR). Alternatively, a nanostructural absorber can reduce the sensitivity as light can bound around between the nanostructures which effectively randomizes the angle distribution. A light trapping structure, which increases light scattering at all angles also helps.

In this work, a periodic array of microscale dome-like silver-coated back-reflectors was added on the back side of the sapphire substrate. Figure 5-11 shows the LHEs of different encoders as a function of the incident angle of light. The result suggests that the LHE is relatively insensitive to the incident angle of light up to ±30º, corresponding to a numerical aperture of 0.5. The sensitivity increases when the incident angle is more than 30º for larger-diameter and thin-film photodetectors. Further improvements are possible with a second light scatterer added on the top [29] or a microlens to function as a spatial filter.

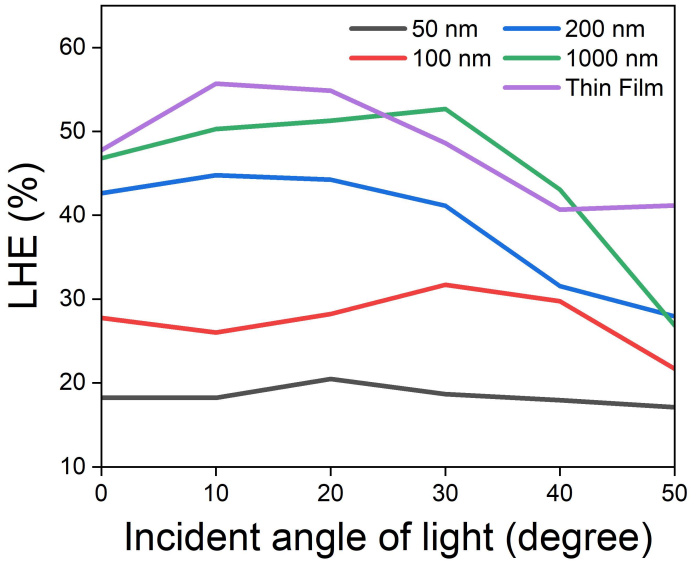

Figure 5-11: The light-harvesting efficiencies (LHEs) of different photodetectors as a function of the incident angle of light calculated using the three-dimensional finite-difference-time-domain (FDTD) method. The legend shows the diameter of the nanopillar in each photodetector. A bottom light-trapping structure with a sidewall angle of 32º as shown in (A) was included in the calculations

5.6 Spectroscopic Performance

To characterize the spectral reconstruction performance, a variety of commercial 5-mm LEDs of different colors and their combinations were used as the test light sources. These LEDs were mounted around 5 cm above the sample with no special alignment or any external optical elements other than making sure the light from all LED devices hit the photodetector area on the sample. The LED emission was separately measured by a commercial spectrometer to obtain the ground truth.

To reconstruct the spectrum, as there are only 16 spectral encoders, the linear system specified by $R_k(\lambda)$ is heavily underdetermined. On the other hand, $R_k(\lambda)$ may change for different

scenarios. While the LHE of the photodetectors used in this study is relatively insensitive to the incident angle of light up to ±30°, the sensitivity starts to increase at a larger incident angle for large-diameter and thin-film photodetectors. The change in the illumination angle distribution may lead to the uncertainty of $R_k(\lambda)$ which means the reconstructed solution may be inaccurate.

To address both challenges, we introduced a variant of total-variation (TV) regularization [233]. The TV loss is defined as $||S||_{TV}^2 = \frac{1}{2}||DS||_2^2$, where $D \in R^{300\times300}$ is the first-order difference matrix given by

$$D = \begin{bmatrix} 1 & -1 & 0 & 0 & 0 & 0 \\ 0 & 1 & -1 & \ddots & \ddots & 0 \\ 0 & 0 & 1 & \ddots & \ddots & 0 \\ 0 & \ddots & \ddots & \ddots & \ddots & 0 \\ 0 & \ddots & \ddots & \ddots & \ddots & -1 \\ 0 & 0 & 0 & 0 & 0 & 1 \end{bmatrix}. \tag{5-1}$$

We solved $\hat{S} = \arg\min_{S\geq0} \frac{1}{2}||I - RS||_2^2 + \lambda||S||_{TV}^2$, where $\lambda > 0$ is the weight of the TV loss. We can interpret the optimization problem as

$$\hat{S} = \arg\min_{S\geq0} \frac{1}{2}\left\|\begin{bmatrix} R \\ \lambda D \end{bmatrix} S - \begin{bmatrix} I \\ 0 \end{bmatrix}\right\|_2^2. \tag{5-2}$$

Given the size of the new sensing matrix $\begin{bmatrix} R \\ \lambda D \end{bmatrix}$, the original problem is now transformed into an over-determined system. This is the uniqueness of our solution for estimating the spectrum. Second, using the modified TV regularizer improves robustness to the uncertainty of $R_k(\lambda)$. It is well understood that adding a regularizing term (e.g., ridge regularization) reduces the sensitivity of the solution $\hat{S}$ to errors in the measurement process [234]. In particular, regularization schemes such as ridge regression are known to be optimally robust against perturbations in the sensing matrix R, which is precisely where the uncertainty arises [235]. Finally, it is worth mentioning that

our formulation is a specific instance of *generalized ridge regression* – in this case, we encourage the reconstructed spectrum to be smooth, which is generally applicable to most optical spectra.

In the following, we present the results of TV regularized spectral reconstruction with an empirical choice of $\lambda = 10^{-5}$ using MATLAB's lsqnonneg routine. The results are summarized in Figure 5-12, where Figures 5-12(a) and 5-12(b) show the results from single- and three-LEDs, respectively. More results can be found in Appendix D. Moreover, for many potential applications of a miniaturized spectrometer, the nature of the optical signal is almost always known *a priori*. In this study, the LED emission can be represented by the sum of multiple Lorentzian-shaped lines, i.e., inhomogeneously broadened. Therefore, in addition to the above results from TV regularization, we convolve the result with a Lorentzian kernel function

$$L(\lambda, \Delta E) = \frac{\Delta E}{4(\lambda-\lambda_o)^2+\Delta E^2}, \tag{5-3}$$

where ΔE is the FWHM line width, h is the Planck's constant, and c is the speed of light. A commercial LED typically has a line width in the range of $3 - 10kT$. In this work, we chose $\Delta E = 6kT$.

5.7 Spectrum Reconstruction Accuracy

Figure 5-13 summarizes the spectral reconstruction performance. We focus on the major features of the spectrum such as the peak positions and the relative optical powers between these peaks, which are likely going to be sufficient for many miniaturized spectrometers' targeted applications. The accuracy of the peak wavelengths has a standard deviation of 0.97%, corresponding to 4 to 6 nm of wavelength accuracy in the visible wavelength range. The accuracy for the intensity ratio at different peak positions is not as good with a standard deviation of 21.1% (or 10.4% if the one outlier is removed). Accurately determining the intensity ratio requires more

spectral information and hence a larger number of spectral encoders, which is left for future investigations. Increasing the number of spectral encoders is also expected to improve the wavelength accuracy but at the expense of a larger chip area and more computational resources.

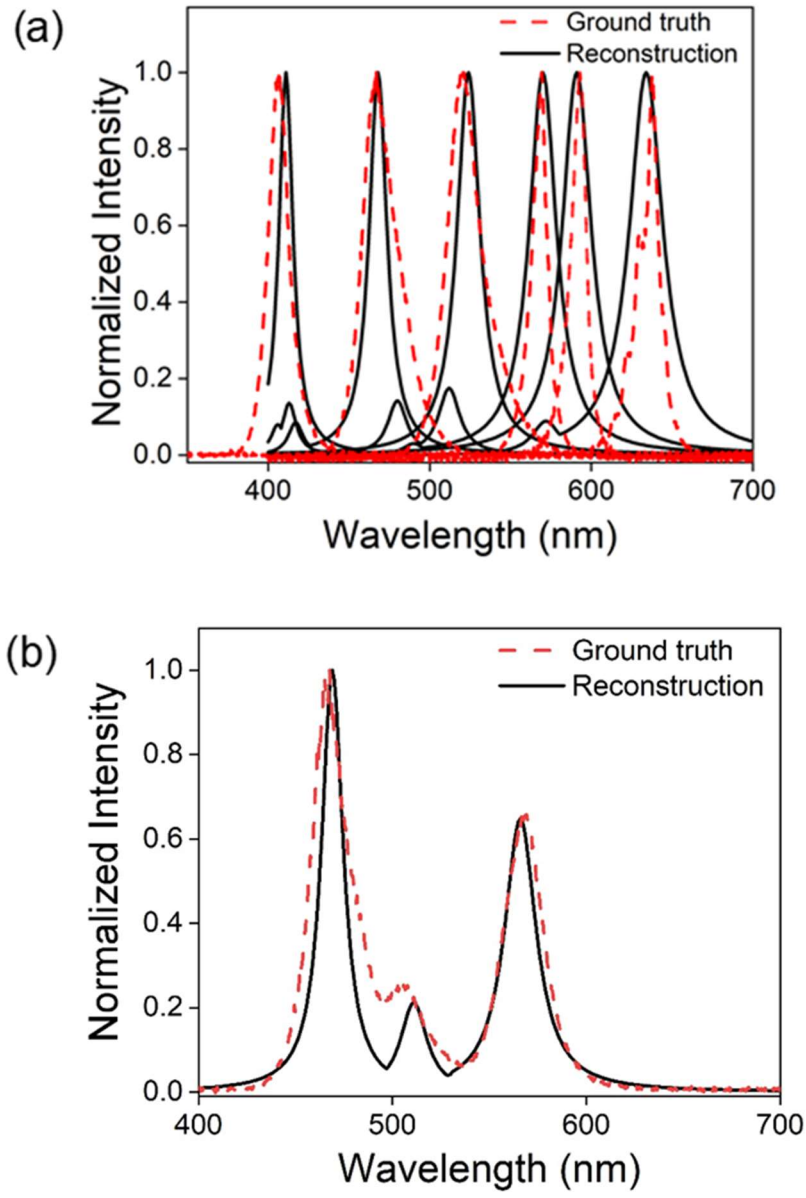

Figure 5-12: The measured spectra constructed from a TV-regularized NNLS algorithm (solid curves) and their comparison to the ground truths (dashed curves) measured by a commercial spectrometer. (a) A series of single-color 5mm LEDs as the test light sources. A total of 10 were measured with six results shown here (see Appendix D for the entire data set). (b) Test light source with three 5mm LEDs of different colors.

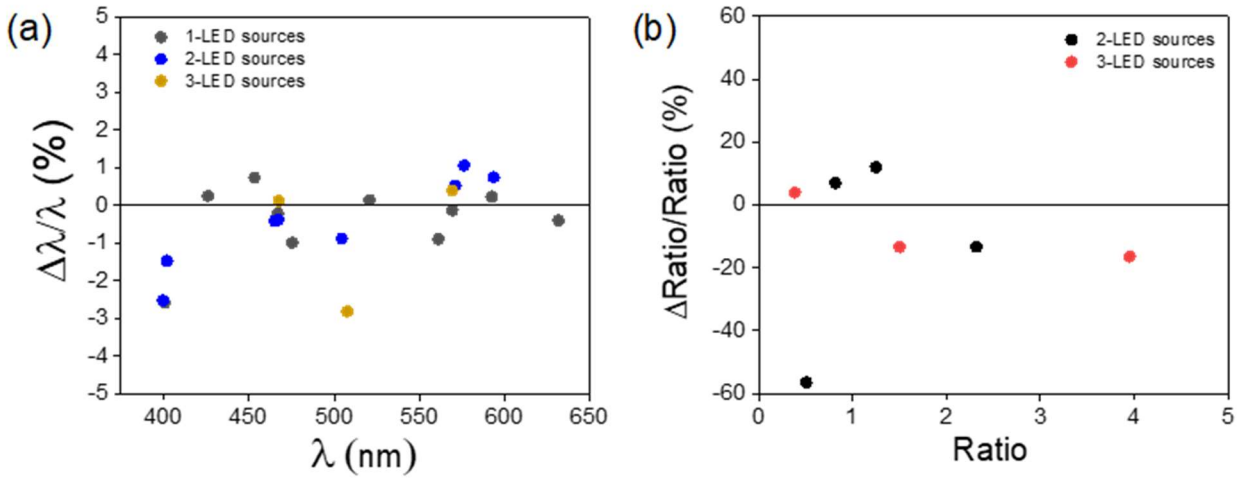

Figure 5-13: The accuracies of spectral reconstruction performance of various test light sources comprising of 1, 2, and 3 LEDs of different colors. (a) The accuracy of the reconstructed peak wavelength positions $\Delta\lambda = \lambda_{reconstructed} - \lambda$ as compared to the ground truth (λ). (b) The accuracy of the intensity ratios $\Delta\mathrm{Ratio}$ at different peak wavelengths as compared to the ground truth (Ratio).

5.8 Discussion

In this work, we assumed the nature of the optical signal was known to improve the spectral reconstruction with an appropriate kernel. It is likely true that the optical signal in many scenarios is categorizable based on the specific application. On the other hand, those applications often have constraints on system size, thickness, weight, power consumption, and reliability under constant motion. The proposed spectrometer design in this study is most suitable for applications that value the thinness and lower power consumption more than the ability to analyze an arbitrary spectrum with a high spectral resolution. Examples can include a wearable or epidermal sensor that regularly monitors an optical signal for a long time.[236–238] By thinning or removing the sapphire substrate and vertically stacking a silicon ASIC that incorporates TIA and microprocessor for

spectral reconstruction as illustrated in Figure 5-1, the overall dimensions of the spectrometer can be no more than a few hundred micrometers in thickness and a few millimeters in the lateral directions. Multiple photodetectors can share one TIA in a round-robin fashion.

While advanced machine learning methods such as deep learning can likely improve the spectral reconstruction performance, they require training with a large number of test light sources.[33,66] In this study, an alternative was suggested based on the known nature of the optical signal---in our case, the Lorentzian lineshape of the LED emission. By manually convoluting the appropriate kernel with the reconstructed spectrum obtained from a simple NNLS algorithm can greatly increase the computational efficiency of the spectrometer while still achieving a reasonable accuracy. Such an approach can potentially greatly reduce the power consumption, a feature likely important for wearable applications.

5.9 Reducing the Number of Detectors

A key step in miniaturizing a spectrometer is determining a minimal subset of detectors that can achieve accurate reconstruction results. However, if we have M available detectors, the time to find an optimal solution to this problem scales *exponentially* with M. Instead, we can use a "greedy" approach to significantly reduce the number of detectors without sacrificing performance, which scales only quadratically with M. The algorithm is as follows: at iteration t, we keep a candidate subset of detectors S_t (we set initial S_0 to be all available detectors). We then choose $\hat{s}$ to be the detector $s \in S_t$ that minimizes $L(S_t \setminus \{s\})$, where $L(S)$ is a loss function measuring reconstruction performance using the subset S of detectors. For our purposes, we use

$$L(S) = \sum_{i=1}^{N} (x_i - \hat{x}_i)^2 + (p_i - \hat{p}_i)^2, \tag{5-4}$$

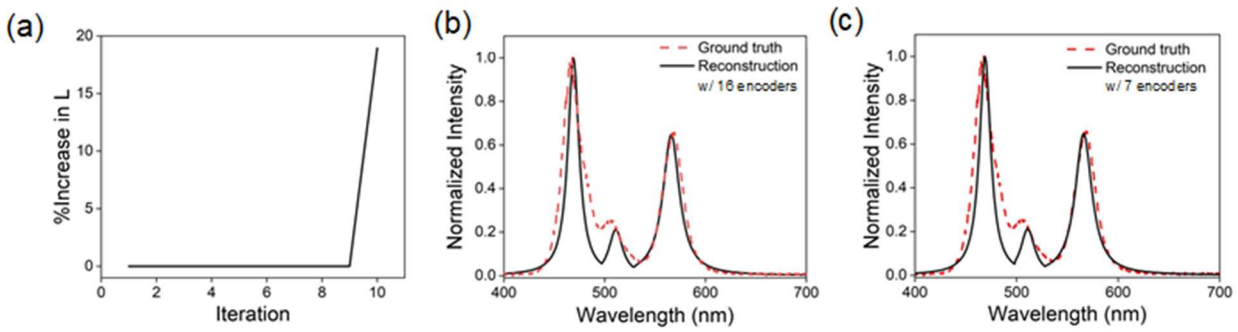

Figure 5-14: Determination of the spectral reconstruction performance using a subset of spectral encoders for the 3-LED spectrum. For each iteration, the encoder that minimizes the loss function, which evaluates the difference between the reconstructed spectrum and ground truth based on the position and magnitude of the spectral peaks, is removed. This process continues until the increase of L for the new iteration exceeds 1%. (a) The percentage increase of the loss function L after each iteration. The increase is negligible up to nine encoders removed, suggesting seven encoders will be sufficient for an accurate reconstruction of the 3-LED spectrum. (b) and (c): The comparison of the spectral reconstruction performance for the entire set of 16 encoders and with only 7 encoders. No noticeable differences can be observed.

where $\{(x_i, p_i)\}_{\{i=1\}}^{N}$ are the pairs of peak locations and magnitudes of the ground truth spectrum (ordered such that $p_1 \geq p_2 \geq \cdots \geq p_N$), $\{(\hat{x}_i, \hat{p}_i)\}_{\{i=1\}}^{N}$ are the largest N pairs of peak locations and magnitudes of the reconstructed spectrum using detectors (ordered such that $\hat{p}_1 \geq \hat{p}_2 \geq \cdots \geq \hat{p}_N$), and N is the number of peaks in the ground truth spectrum. If there are less than N peaks in the reconstructed spectrum, we let $L(S) = \infty$. We then remove $\hat{s}$ from our candidate subset, setting $S_{t+1} = S_t \setminus \{\hat{s}\}$. If the percent increase in L is larger than some threshold (e.g. 1%), then S_t is the final subset, otherwise, we continue to the next iteration.

We applied this procedure to our $M = 16$ detectors on the same test light source with three 5 mm LEDs of different colors. Results are shown in Figure 5-14. We found that we could remove 9 consecutive detectors until there is any loss in reconstruction, and we stopped on iteration 10,

the final minimal subset consists of detectors 10-16. While we had more than halved the number of detectors used, the reconstruction results shown were nearly identical to the spectrum recovered using all 16 detectors.

5.10 Specific Detectivity D^*-Figure of Merit

Specific detectivity $D^*$is an important figure of merit for a photodetector based on which the sensitivity of a photodetector is quantified [239–242]. Numerically, it is given by,

$$D^* = R\sqrt{\frac{1}{2eJ_d}}, \tag{5-5}$$

where R is responsivity, J_d is dark current density, and e is the electronic charge.

According to Equation (5-5), specific detectivity D^* is related to the dark current for a photodetector. This makes the dark current an important factor. High dark currents yield high noise levels due to which D^* decreases. In this work, GaN-based photodiodes comprising of an array of nanopillars having a diameter of 1000 nm, 600 nm, and 100 nm showed a maximum responsivity of 4.82×10^{-4} A/W, 2.57×10^{-5} A/W, 3.24×10^{-6} A/W and $D^*$of 2.98×10^{10} Jones, 6.07× 10^8 Jones, 2.23×10^7 Jones, respectively. The thin film showed a maximum responsivity of 3.7×10^{-4} A/W and $D^*$of 1.17×10^{10} Jones. Figure 5-15 illustrates the results for D^* as a function of wavelength for different photodiodes.

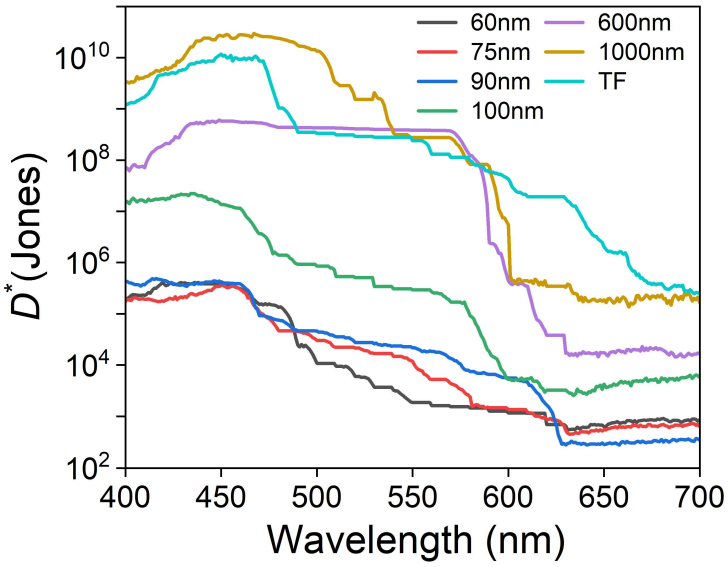

Figure 5-15: The D^* of the photodetectors measured from the responsivity and dark current. The legend shows the diameter of the nanopillar in each photodetector, ranging from 60 nm to thin film (TF).

5.11 Conclusion

A wafer-thin chip-scale portable spectrometer system based on the NNLS spectral reconstruction algorithm was proposed and demonstrated. A total of 16 spectral encoders which simultaneously functioned as photodetectors were monolithically integrated with a chip area of 0.16 mm^2 using the principle of local strain engineering in compressively strained InGaN/GaN MQW structures. When the InGaN MQW active region is shaped into an array of nanopillars, the strain is relaxed from the edge of the nanopillar which modifies the absorption cutoff wavelength and the spectral response. Using different nanopillar diameters, the absorption properties were programmed and tuned across the visible spectrum. The built-in GaN pn junction enabled photocurrent measurements at a zero bias. The sensitivity of the absorption was suppressed for an incident angle

of light up to 30º using a cone-shaped back-reflector fabricated at the underside of the sapphire substrate. As a result, no external optics such as collimation optics and apertures were used or necessary in the experimental demonstration. A non-negative least square (NNLS) algorithm with total-variation (TV) regularization and a choice of Lorentzian kernel function was shown to deliver a decent spectral reconstruction performance in the wavelength range of 400 – 650 nm. The accuracies of spectral peak positions and intensity ratios between peaks were found to be 1.08% and 11.3%, respectively. The small chip area together with a computationally efficient spectral reconstruction algorithm makes the proposed spectrometer especially suitable for wearable applications.

Chapter 6 Conclusion

6.1 Summary

In summary, we proposed and demonstrated a reconstructive optical spectrometer concept based on GaN semiconductors. Local strain engineering in GaN DIW nanopillar structures enabled the control of the absorptive and emission properties of each diode. Spectroscopic functionality was demonstrated using advanced machine-learning methods. The ultrathin profile of the proposed spectrometer chip enables miniaturize spectroscopic techniques, including UV-VIS, fluorescence, chemi-, and electro-luminescence, and diffuse reflectance spectroscopy to open new opportunities for biosensing, neuro- and endoscopic probes, internet-of-things, and environmental monitoring

First, an array of monolithically integrated GaN-based photodiodes with built-in spectral filtering responses was demonstrated. The comparison to the emission wavelength variation from the same set of devices confirmed the strain relaxation was the major cause for the blue shift of the absorption cutoff wavelength with a decreasing nanopillar diameter. Spectroscopic function was also demonstrated using only 14 photodiodes in combination with a spectral reconstruction algorithm. The spectral filtering is intrinsic to the DIW nanopillars and has negligible dependence on the incident angle of light, enabling an optics-free spectrometer chip and simplifying integration in a lab-on-a-chip layout.

Second, we designed, fabricated, and demonstrated the feasibility of an optics-free spectrometer chip with a monolithically integrated LED light source. With 13 photodetectors, we successfully achieved spectroscopic functionalities in the wavelength range between 450 nm and 540 nm. We also demonstrated the feasibility of reflection spectroscopy using the on-chip LED source and photodetectors simultaneously. The optical blocking structure successfully suppressed the direct capture of the LED emission by the photodetectors, which were as close as 0.3 mm from the LED. We showed that the spectrometer chip in this work did not require any external optics for its functionality. Therefore, the proposed spectrometer design can potentially enable a miniaturized spectroscopic system in an ultrathin film platform which can enable new opportunities, e.g., a wearable spectrometer chip to monitor physiological conditions in real-time.

Third, we have demonstrated an absorption-based on-chip optical spectrometer design based on a standard LED epitaxial stack. Using local strain engineering, the detector's absorption cut-off wavelength can be tuned geometrically by various lithographically defined arrays of nanopillars with different diameters. In spite of InGaN's high absorption coefficient, the lattice mismatch between InGaN and GaN limits the LHE of an InGaN/GaN MQWs to a few percentage points. To this end, we introduced a simple cone-shaped, Ag-coated back-reflector at the bottom side of the sapphire substrate to enhance the absorption. The interplay between the light scattering from the nanopillar array and the deflection from the cone shape significantly increases the absorption length through the active region. The LHE can be further enhanced with the addition of a thin TiO_2 film dotted with a two-dimensional TiO_2 periodic structure. Using a photodetector design previously demonstrated by experiments, LHEs of 20–60% can be obtained in the wavelength range of 450 nm–590 nm, which represents a 10-fold improvement on the prior results.

Not only can the Ag-coated cone-shape back-reflector be readily fabricated using mature patterned sapphire substrate processes, but the enhanced LHEs can lead to improved accuracy of spectral reconstruction in the situation when the number of photodetectors is smaller than the degree of freedom or the number of independent wavelengths. Moreover, the LHE enhancement to the cone-shaped back-reflector and the top TiO_2 layer exhibit weak dependence on the incident angle of light, reducing the requirement to include collimation optics as is often needed for most spectrometers. Therefore, our spectrometer design can enable an ultrathin form factor for an array of spectrometers on the chip, which can be attractive for many mobile applications

Lastly, a wafer-thin chip-scale portable spectrometer system based on the NNLS spectral reconstruction algorithm was proposed and demonstrated. A total of 16 spectral encoders, which simultaneously functioned as photodetectors, were monolithically integrated on a chip area of 0.16 mm^2 using the principle of local strain engineering in compressively strained InGaN/GaN MQW structures. When the InGaN MQW active region is shaped into an array of nanopillars, the strain is relaxed from the edge of the nanopillar, which modifies the absorption cutoff wavelength and the spectral response. The absorption properties were programmed and tuned across the visible spectrum using different nanopillar diameters. The built-in GaN pn junction enabled photocurrent measurements at a zero bias. The absorption sensitivity was suppressed for an incident angle of light up to 30º using a cone-shaped back reflector fabricated on the underside of the sapphire substrate. As a result, no external optics such as collimation optics and apertures were used or necessary in the experimental demonstration. A non-negative least square (NNLS) algorithm with total-variation (TV) regularization and a choice of Lorentzian kernel function was shown to deliver a decent spectral reconstruction performance in the wavelength range of 400 – 650 nm. The

accuracies of spectral peak positions and intensity ratios between peaks were found to be 1.08% and 11.3%, respectively. Spectral reconstruction for an under-determined system is a topic in a rapidly developed field: compressive sensing. A more suitable algorithm may be identified to work with the nature of our absorber spectral properties.

6.2 Future Perspective

The future vision of this research lays in creating a highly portable and versatile sensing platform for various spectroscopic techniques. Spectroscopy is a system. Miniaturizing it involves a combination of multiple inventing schemes to conceive a mature multifunctional version. This study has a great potential to envision new avenues for which multilateral research can accelerate convergence. In this section, a few prospects for future work are unveiled.

6.2.1 Automation of Data Acquisition

The first step in the pipeline is to replace the current experimental setup with a fully automated system for better, faster, and more reliable data acquisition. The electrical characterization of the spectroscopic chip was currently done by using micropositioners that manually positioned the probes on one pixel at a time to measure photocurrents, which was a time-consuming and arduous job. To sidestep this issue and accelerate the testing, wire bonding can be used. The sample can be mounted on a leadless chip carrier (LCC), which provides an easy and direct insertion on a circuit board. Electrical interconnects between the sample and LCC can be made via wire bonding as shown in Figure 6-1. Electrical testing can be conducted with circuit boards driven by executable code using computer programs.

Automated chip testing will also facilitate a faster and more accurate spectrum recovery with a limited number of photodetectors. With this, a massive amount of training data points can be collected to design effective optimization methods. Moreover, instead of manually modeling the data acquisition, a network can be formed to automatically sequence the whole data model.

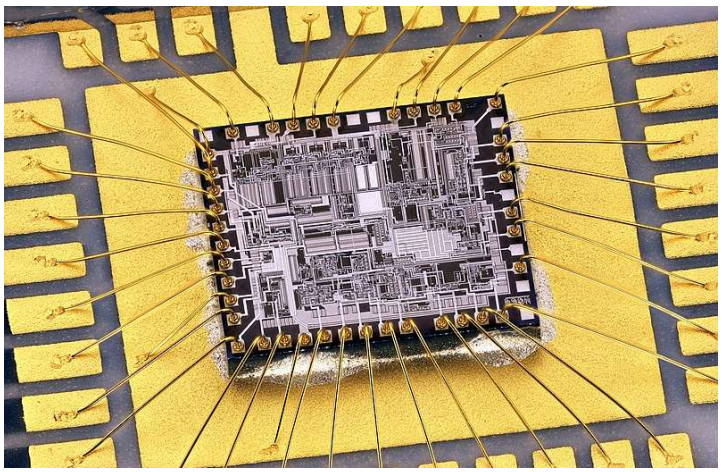

Figure 6-1: Optical image of a silicon die, which is wire bonded on LCC [243]. The purpose is to give an illustration of conceiving the automated mode of testing using our own device.

6.2.2 Entirely Integrated Hybrid Architecture

In future, research can be focused on the seamless integration and scaling of multiple dissimilar functional components, including reference/excitation light sources, spectral encoders, photodetectors, and measurement circuits in an ultralow profile. A conceptual illustration of the

strategies is shown in Figure 6-2. In this dissertation, we showed a very weak dependence of GaN photodetectors on the incident angle of light due to their inherent spectral filtering property. Taking advantage of this, there is no need to condition the optical signal's angle distribution with collimation optics or an aperture enabling a direct integration on a lab-on-a-chip platform. The proof-of-concept chip has a total thickness of <1 mm and a lateral dimension of ~0.1 mm. In future, the chip's thickness can be further reduced to <50 µm for flexible and wearable applications with the removal of sapphire substrate or by using ultrathin silicon substrates

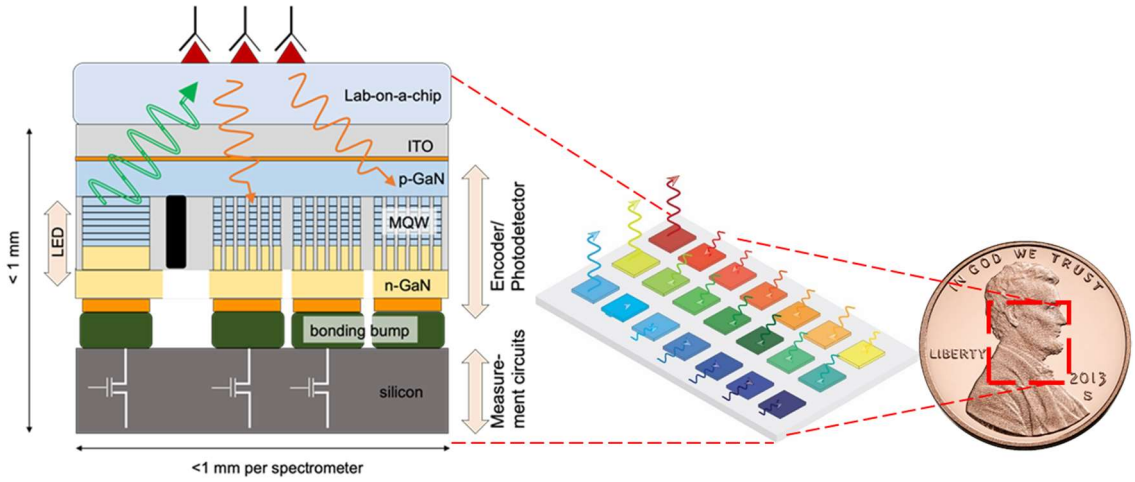

Figure 6-2: Schematic of the proposed miniaturized spectrometer integrating all necessary functional components including LED light sources, spectral encoders, photodetectors, and measurement IC on a chip-scale platform in an ultralow profile (~<1mm or 40µm with sapphire removal and ultrathin silicon). Optical blocking (black rectangle) suppresses interference between on-chip LED and detectors. As shown is the monolithic integration of the GaN reference or excitation LED (one or more) and spectral encoders, which double as photodetectors.

6.2.3 Developments with Machine-Learning

Spectral reconstruction for an under-determined system is a topic in a rapidly developed field: compressive sensing. The reconstructive spectrometer has attracted intense research interest due to its ability to offer miniaturization in the true sense. With machine learning and optimization advances, the spectrum can be efficiently reconstructed even with only a small number of encoders/photodetectors. Hence, in the future, new methods with more precise models are needed to develop for better spectrum reconstruction. Finetune network architectures, hyperparameters, deep learning methods, and their effectiveness are fast-growing challenging areas worth working on.

6.2.4 Wearable Optical Spectrometer for Chemical Sensing

The photodetector's size is currently 100 μmx100 μm with a photocurrent output from 0.1 nA up to ~1 μA at a zero bias. To continue shrinking the detector's size while improving the signal-to-noise ratio, an optimization is required for both detector's electrical property and light-harvesting efficiency. This can be achieved by continuing improvements in the device fabrication (e.g., the uniformity of the planarization process before metallization) and design. With these optimizations and improvements, the number of detectors can be increased while decreasing the chip area, which is suitable for sensor arrays. Figure 6-4 shows an illustration of a wearable senor for noninvasive and multiplexed sweat monitoring. There are several powerful techniques, with which the GaN nanostructures can be easily detached from their primary substrate and transferred to another flexible substrate. This opens up a novel approach that can potentially enable the

realization of foldable, flexible, deformable, and personal wearable optical spectrometers for disposable chip application in a fully hybrid architecture.

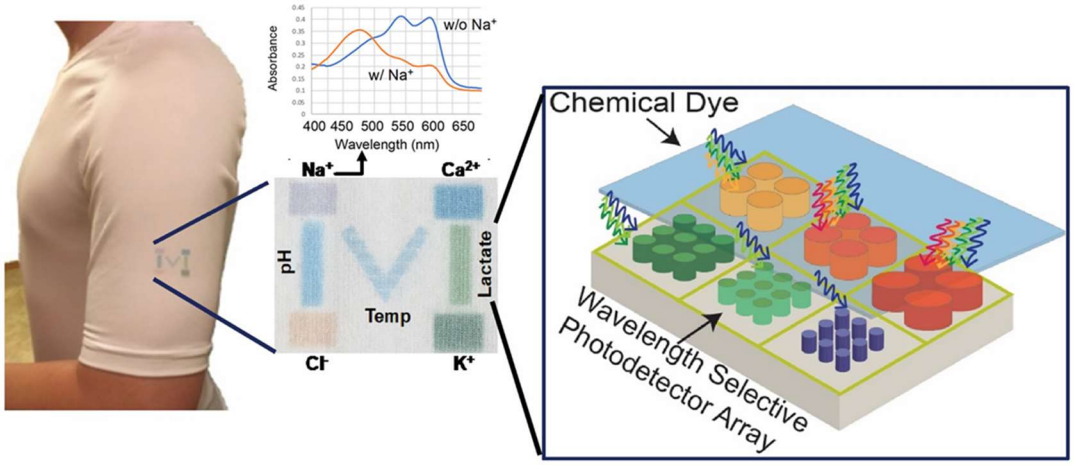

Figure 6-3: The illustration of the future integration of a wearable chemical sensor. The cross-section of the proposed optical chemical sensor is also shown.

6.2.5 Optical Spectroscopy in UV/VIS Wavelength Extended to Infrared

As a part of this research, we have shown a decent spectroscopic functionality of our chip in the wavelength range of 400 – 650 nm. Local strain engineering was used to tune the bandgap of the nanostructures monolithically integrated on the chip. Group-III nitride semiconductors exhibit direct bandgaps across a wide spectral range from 190 nm through 1.9 μm. Strain

engineering in III-nitride disk-in-wire (DIW) polar nanostructures can be extended from the aforementioned spectral range. Upon the formation of quantum dots with a nanopillar diameter up to a few tens of nanometers, III-nitride quantum dots can cover a wavelength range from 260 nm through 1300 nm. Figure 6-4(a) shows this geometric tuning using Nextnano[3] by simulating a nanopillar structure with 1 nm of InN QW embedded in a 12 nm GaN barrier. Hence, III-nitride quantum dots can potentially provide an ideal platform to realize continuous and arbitrary tuning across the UV, visible, and near-infrared spectra with heterogeneous integration of InN/GaN and GaN/AlN heterostructures using for example the transfer printing technique.

Moreover, in the future efforts can be made on an all-semiconductor platforms with the heterogeneous integration of silicon and GaN, the two most popular semiconductors. For example, InN/GaN DIW nanostructures can be integrated with silicon photodetectors as passive spectral filters. A possible design scenario is shown in Figure 6-4(b).

6.2.6 Hyperspectral Imaging

Finally, the theoretical and experimental analysis of the current study suggests that a GaN-based optical spectrometer can be used for hyperspectral imaging. The main challenge of miniaturizing a spectrometer is the difficulty of shrinking multiple dissimilar system components while simultaneously addressing their integration and performance. On the hardware end, the focus in future studies will continue to address three areas of need: 1. Chip-scale integration of reconfigurable (narrowband, broadband) light sources with broadband spectral encoders with an ultralow profile. 2. Further reducing the number of detectors by adopting new machine learning methods that lead to faster and more accurate spectrum recovery. 3. Continuing shrinkage of the

spectrometer's chip area. Significant research in all these areas can eventually enable a large sensor array or hyperspectral imaging with a high spatial resolution

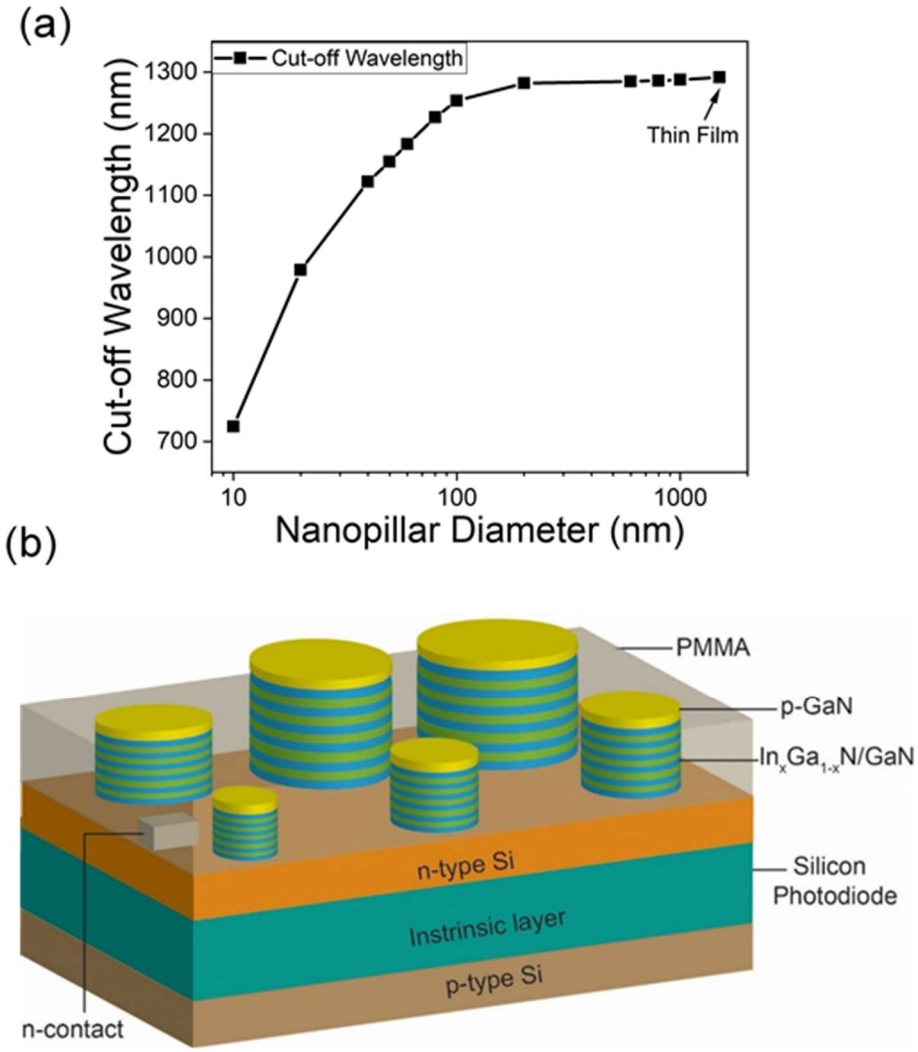

Figure 6-4: (a) Cut-off wavelength tuning of InN/GaN DIW nanopillar structures with different diameters. Nextnano simulation tool was used to simulate a nanopillar with InN (1 nm)/GaN (12nm). Strain-induced III-nitride quantum dots can cover a wavelength from 300 nm through 900 nm by properly choosing the composition, thickness, diameter, and barrier material. (b) Conceptual design of heterogeneous integration of GaN semiconductors with silicon. It uses an all-semiconductor construction where the integration takes place via tight-pitch SLID bonding.

Appendix A

Code Flow Scheme of Nextnano [3] Software

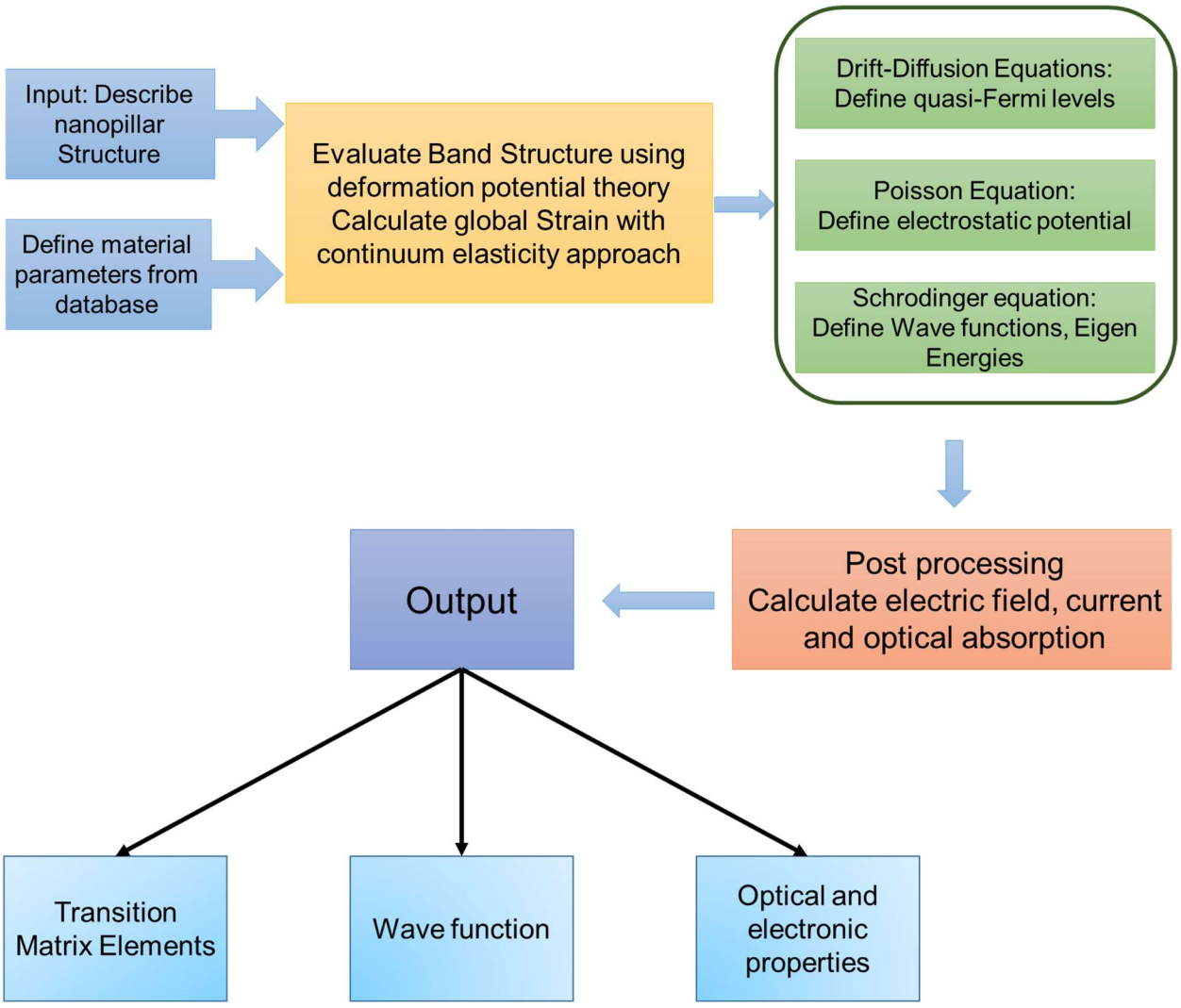

Figure A-1: Simulation flow scheme of Nextnano[3] software. The program was used to calculate the band structure and Eigen state energies of the 3D nanopillar structure. GaN nanopillar was comprised of a single InGaN quantum well with 2.5 nm thickness.

Appendix B

MATLAB Program for Calculating Absorption in Nanopillar Structures

```
clear all;
close all;

%%%%%%%%%%%%%%%%%%%%%%%%%%%%%%%%%%%%%%%%%%%%%%%%%%%%%%%%%%%%%%%%%%%%%%%
%%%%%%%%%%%%%%%%%%%%READ LH textfile%%%%%%%%%%%%%%%%%%%%

data1 = tdfread('10nmLH.txt', '\t');
% data1 = cell2mat(struct2cell(data));
data2 = dlmread('10nmLH.txt','\t');
A=data2;
    indices1 = find(A(:,2)==0);
   A(indices1,:) = [];
    Enm_LH = A(:,1);
   Inm_LH = A(:,2);
    figure(1)
  stem(Enm_LH,Inm_LH)


title('Overlap Integral_LH');
xlabel('Transition Energy(eV)');
ylabel('Overlap Integral_LH');

%%%%%%%%%%%%%%%%%%%%%%%%%%%%%%%%%%%%%%%%%%%%%%%%%%%%%%%%%%%%%%%%%%%%%%%
%%%%%%%%%%%%%%%%%%%%%%READ HH textfile%%%%%%%%%%%%%%%%%%%%

data3 = tdfread('10nmHH.txt', '\t');
data4 = dlmread('10nmHH.txt','\t');
B=data4;
    indices2 = find(B(:,2)==0);
  B(indices2,:) = [];
    Enm_HH =B(:,1);
   Inm_HH = B(:,2);
```

```
        figure(2)
      stem(Enm_HH,Inm_HH)
    title('Overlap Integral_HH');
    xlabel('Transition Energy(eV)');
    ylabel('Overlap Integral_HH');

%%%%%%%%%%%%%%%%%%%%%%%%%%%%%%%%%%%%%%%%%%%%%%%%%%%%%%%%%%%%%%%%%%%%%%%%
%%% Structure Details%%%%%%%%%%%%%%%%%%%%%%%%%%%%%%%%%%%%%%%%%%%%%%%%%%%

    % indium composition of InGaN QW
    indium_composition = 0.32;
    % quantum well thickness in m
    Lz=2.5e-9;
    % Nano-pillar Diameter in m

    D = 10e-9;
    % barrier thickness in m
     Lb= 20e-9;

%%%%%%%%%%%%%%%%%%%%%%%%%%%%%%%%%%%%%%%%%%%%%%%%%%%%%%%%%%%%%%%%%%%%%%%%
%%%%%% Physical constants%%%%%%%%%%%%%%%%%%%%%%%%%%%%%%%%%%%%%%%%%%%%%%

    m0= 9.1e-31; % mass of electron
    h_bar=1.054571817e-34;
    e=1.6e-19;
    c=3e8;
    epsilon=8.8541878128e-12;

%%%%%%%%%%%%%%%%%%%%%%%%%%%%%%%%%%%%%%%%%%%%%%%%%%%%%%%%%%%%%%%%%%%%%%%%
% %%% Database for wurtzite GaN, InN%%%%%%%%%%%%%%%%%%%%

    n_r=2.6;            %%%% Refractive Index for InGaN
    E_px_GaN=16.265;    %%%%Parameter Epx for GaN
    E_px_InN=8.809;     %%%%Parameter Epx for InN
    me_GaN=0.2;         % effective mass of electron  in GaN
    me_InN=0.12;        % effective mass of electron  in InN
    mhh_GaN=1.4;         % effective mass of heavy hole  in
GaN
    mlh_GaN=0.259;       % effective mass of Heavy hole  in
GaN
    mhh_InN=1.63;        % effective mass of Light hole  in
InN
    mlh_InN=0.27;        % effective mass of light hole  in
InN
```

```
    D1=-3.7;            %in eV same for both GaN & InN
    D2=4.5;             %in eV same for both GaN & InN

  %%%%%%%%%%%%%%%%%%%%%%%%%%%%%%%%%%%%%%%%%%%%%%%%%%%%%%%%%%%%%%%%
  %%% NextNano Input vary w.r.t nanopillar diameter%%%%%

  %Taken at the center of Nanopillar x=0.125nm, y=0.125nm &
z= 10.125nm

    epsilon_xx= -0.019;

    %Taken at the center of Nanopillar x=0.125nm, y=0.125nm
& z= 10.125nm

    epsilon_yy= -0.019 ;

    %Taken at the center of Nanopillar x=0.125nm, y=0.125nm
& z= 10.125nm

    epsilon_zz= 0.0056 ;
    E_2=-1.91 ;
    E_3=-2.13 ;

  %%%%%%%%%%%%%%%%%%%%%%%%%%%%%%%%%%%%%%%%%%%%%%%%%%%%%%%%%%%%%%%%
  %%%%%%%%%%%%%%%%%%%%%%%%%%%%%%%%%%%%%%%%%%%%%%%%%%%%%%%%%%%%%%%%

    % effective mass of electron in InGaN

    me_well=(inv(((1-
indium_composition)/(me_GaN))+((indium_composition)/(me_InN
))));

    % effective mass of heavy hole in InGaN

    mhh_well=(inv(((1-
indium_composition)/(mhh_GaN))+((indium_composition)/(mhh_I
nN))));

     % effective mass of light hole in InGaN

    mlh_well=(inv(((1-
indium_composition)/(mlh_GaN))+((indium_composition)/(mlh_I
nN))));
```

```
    %Reduced mass heavy hole and electron

    mr_hh=(inv((1/me_well)+(1/mhh_well)))*m0;

      %Reduced mass heavy hole and electron

    mr_lh=(inv((1/me_well)+(1/mlh_well)))*m0;

    % bandgap of InGaN

    Egqw            =            indium_composition*0.64+(1-
indium_composition)*3.44;
    delta_Ec   =   (3.4-Egqw)*0.6;     %   we   assume   0.6/0.4
bandoffsets
    delta_Ev = (3.4-Egqw)*0.4;

  %%%%%%%%%%%%%%%%%%%%%%%%%%%%%%%%%%%%%%%%%%%%%%%%%%%%%%%%%%%%%%%%
  %%%%%%%%%%%%%%%%%%%%%%%%%%%%%%%%%%%%%%%%%%%%%%%%%%%%%%%%%%%%%%%%

    pre_factor = ((pi*(e)^2*h_bar)/((m0)^2*c*n_r*epsilon));

    %TE-Polarization from HH-C

    E_p_HH=((1-
indium_composition)*E_px_GaN)+((indium_composition)*E_px_In
N);
    matrix_moment_HH=(1/4)*m0*E_p_HH;
    lambda=(D1*epsilon_zz)+(D2*(epsilon_xx+epsilon_yy));
    p_square=  1;    %%(E_2-lambda)/(E_2-E_3);%%ASSUMPTION

    %TE-Polarization from LH-C
    matrix_moment_LH=p_square*(1/4)*m0*E_p_HH;
     f_c=0;
       f_v=1;

  %%%%%%%%%%%%%%%%%%%%%%%%%%%%%%%%%%%%%%%%%%%%%%%%%%%%%%%%%%%%%%%%
  %%%%%%%%%%%%%%%%%%%%%%%%Integral Overlap LH%%%%%%%%%%%%

       i = 1;
     I_LH = 0;
    fs = [];
     for E_LH = 1:0.001:3.4
        for n = 1 : length(A)
       Enm_LH = A(n,1);
```

```
    Inm_LH = A(n,2);
         if(E_LH > Enm_LH)
         I_LH = I_LH + Inm_LH;
    end
end
matrix_value(i, 1) = E_LH;
matrix_value(i, 2) = I_LH;

% Final_sum = sum; % final one value for whole text file
 hold on;
figure(3)
plot(E_LH, I_LH, '.')
title('Overlap Integral_LH');
xlabel('Photon Energy(eV)');
ylabel('Overlap Integral_LH');
I_LH = 0;
 i = i + 1;
end

%%%%%%%%%%%%%%%%%%%%%%%%%%%%%%%%%%%%%%%%%%%%%%%%%%%%%%%%%%%%%%%%%%%%%%%
%%%%%%%%%%%%%%%%%%%%%%%%Integral Overlap LH%%%%%%%%%%%%

enm_LH=A(:,1);
inm_LH=A(:,2);
% e_start=min(enm);
% e_end=max(enm);
e_start_LH=1;
e_end_LH=3.4;
stepsize_LH=0.001;
e_LH=e_start_LH:stepsize_LH:e_end_LH;
inew_LH=[];
for l=1:length(e_LH)
    xe_LH=e_LH(l);
    xl_LH=0;
    for j=1:length(enm_LH)
       if enm_LH(j)<xe_LH
           xl_LH=xl_LH+inm_LH(j);
       end
    end
    inew_LH=[inew_LH, xl_LH];
end
```

```
figure(4)
plot(e_LH,inew_LH);
grid on;
title('Overlap Integral_LH');
xlabel('$E_LH$','Interpreter','Latex');
ylabel('$I_LH$','Interpreter','Latex');

%%%%%%%%%%%%%%%%%%%%%%%%%%%%%%%%%%%%%%%%%%%%%%%%%%%%%%%%%%%%%%%%%%%%%%%%
%%%%%%%%%%%%%%%%%%%%%%%%%%%%%%%%%%%%%%%%%%%%%%%%%%%%%%%%%%%%%%%%%%%%%%%%


for g=1:length(e_LH)
    wavelength(g)=1240/(e_LH(g));
end


figure(11)
plot(wavelength,inew_LH);
grid on;
title('Overlap Integral_LH');
xlabel('$wavelength$','Interpreter','Latex');
ylabel('$I_LH$','Interpreter','Latex');

%%%%%%%%%%%%%%%%%%%%%%%%%Integral Overlap HH%%%%%%%%%%%%%
%%%%%%%%%%%%%%%%%%%%%%%%%%%%%%%%%%%%%%%%%%%%%%%%%%%%%%%%%%%%%%%%%%%%%%%%

    k = 1;
 I_HH = 0;
fs = [];
for E_HH = 1:0.001:3.4
    for m = 1 : length(B)
   Enm_HH = B(m,1);
   Inm_HH = B(m,2);
         if(E_HH > Enm_HH)
        I_HH = I_HH + Inm_HH;
   end
end
matrix_value(k, 1) = E_HH;
matrix_value(k, 2) = I_HH;

% Final_sum = sum; % final one value for whole text file

 hold on;
figure(5)
```

```
plot(E_HH, I_HH, '.')
title('Overlap Integral_HH');
xlabel('Photon Energy(eV)');
ylabel('Overlap Integral_HH');
I_HH = 0;
 k = k + 1;
end

%%%%%%%%%%%%%%%%%%%%%%%%%%%%%%%%%%%%%%%%%%%%%%%%%%%%%%%%%%%%%%%%%%%%%%%%
%%%%%%%%%%%%%%%%%%%%%%%%Integral Overlap LH%%%%%%%%%%%%%

enm_HH=B(:,1);
inm_HH=B(:,2);
% e_start=min(enm);
% e_end=max(enm);
e_start_HH=1;
e_end_HH=3.4;
stepsize_HH=0.001;
e_HH=e_start_HH:stepsize_HH:e_end_HH;
inew_HH=[];
for t=1:length(e_HH)
    xe_HH=e_HH(t);
    xt_HH=0;
    for p=1:length(enm_HH)
       if enm_HH(p)<xe_HH
           xt_HH=xt_HH+inm_HH(p);
       end
    end
    inew_HH=[inew_HH, xt_HH];
end


figure(6)
plot(e_HH,inew_HH);
grid on;
title('Overlap Integral_HH');
xlabel('$E_HH$','Interpreter','Latex');
ylabel('$I_HH$','Interpreter','Latex');


figure(12)
plot(wavelength,inew_HH);
grid on;
title('Overlap Integral_HH');
```

```
    xlabel('$wavelength$','Interpreter','Latex');
    ylabel('$I_HH$','Interpreter','Latex');

  %%%%%%%%%%%%%%%%%%%%%%%%%%%%%%%%%%%%%%%%%%%%%%%%%%%%%%%%%%%%%%%%%%%%
  %%%%%%%%%%%%%%%%%%%%%%%%ABSORPTION COEFFICIENT HH%%%%%%

       for s=1:length(e_HH)
    absorp_HH(s)=
(1/e_HH(s))*pre_factor*matrix_moment_HH*(f_v-
f_c)*(mr_hh/(pi*(h_bar^2)*Lz))*inew_HH(s)*(1/100);
       end


    figure(7)
    plot(e_HH,absorp_HH);
    grid on;
    title('Absorption Coefficient_HH');
    xlabel('$E$','Interpreter','Latex');
    ylabel('$Absorption
Coefficient_HH$','Interpreter','Latex');


    figure(13)
    plot(wavelength,absorp_HH);
    grid on;
    title('Absorption Coefficient_HH');
    xlabel('$wavelength$','Interpreter','Latex');
    ylabel('$Absorption
Coefficient_HH$','Interpreter','Latex');

  %%%%%%%%%%%%%%%%%%%%%%%%%%%%%%%%%%%%%%%%%%%%%%%%%%%%%%%%%%%%%%%%%%%%
  %%%%%%%%%%%%%%%%%%%%%%%%ABSORPTION COEFFICIENT lH%%%%%%%

    for z=1:length(e_LH)
    absorp_LH(z)=
(1/e_LH(z))*pre_factor*matrix_moment_LH*(f_v-
f_c)*(mr_lh/(pi*(h_bar^2)*Lz))*inew_LH(z)*(1/100);
    end


    figure(8)
    plot(e_LH,absorp_LH);
    grid on;
    title('Absorption Coefficient_LH');
```

```
    xlabel('$E$','Interpreter','Latex');
    ylabel('$Absorption
Coefficient_LH$','Interpreter','Latex');


    figure(14)
    plot(wavelength,absorp_LH);
    grid on;
    title('Absorption Coefficient_LH');
    xlabel('$wavelength$','Interpreter','Latex');
    ylabel('$Absorption
Coefficient_LH$','Interpreter','Latex');

  %%%%%%%%%%%%%%%%%%%%%%%%%%%%%%%%%%%%%%%%%%%%%%%%%%%%%%%%%%%%%%%%%%%%%%%
  %%%%%%%%%%%%%%%%%%%%%%%%ABSORPTION COEFFICIENT TOTAL%%%

    for y=1:length(e_LH)
    absorp(y)= absorp_HH(y)+absorp_LH(y);
    end
    figure(9)
    plot(e_LH,absorp);
    grid on;
    title('Total Absorption Coefficient');
    xlabel('$E$','Interpreter','Latex');
    ylabel('$Absorption Coefficient Total $ ',' Interpreter
',' Latex');

    figure(15)
    plot(wavelength,absorp);
    grid on;
    title('Total Absorption Coefficient');
    xlabel('$Wavelength$','Interpreter','Latex');
    ylabel('$Absorption                          Coefficient
Total$','Interpreter','Latex');

  %%%%%%%%%%%%%%%%%%%%%%%%%%%%%%%%%%%%%%%%%%%%%%%%%%%%%%%%%%%%%%%%%%%%%%%
  %%%%%%%%%%%%%%%%%%%%%%%%Responsivity%%%%%%%%%%%%%%%%%%%%%%%%

    k_B= 1.38e-23;
    T= 300;
    u_n=200 ;
    u_p= 20;
    t_n= 6.5e-9;
    t_p= 6.5e-9;
```

```
P=2.5e-3;
Ref=0;
A=pi*((D/2)^2);
V=pi*((D/2)^2)*Lz;
D_n=((k_B*T)/e)*u_n;
D_p=((k_B*T)/e)*u_p;
L_n=sqrt(D_n*t_n);
L_p=sqrt(D_p*t_p);
for f=1:length(e_LH)
Res(f)=(A*(e*((P*(1-Ref))/(V*e_LH(f)*1.6e-19))*(1-exp(-
absorp(f)*Lz))*(L_n*1e-2+Lz+L_p*1e-2)))/P;
End


figure(10)
plot(e_LH,Res);
grid on;
title('Responsivity');
xlabel('$E$','Interpreter','Latex');
ylabel('$Responsivity$','Interpreter','Latex');


figure(16)
plot(wavelength,Res);
grid on;
title('Responsivity');
xlabel('$Wavelength$','Interpreter','Latex');
ylabel('$Responsivity$','Interpreter','Latex');
```

Appendix C

MATLAB Program for Solving the Shockley Diode Equation

```
 clear all;
close all;

%%%%%%%%%%%%%%%%%%%%%%%%%%%%%%%%%%%%%%%%%%%%%%%%%%%%%%%%%%%%%%%%%%%%%%%
%%%%%%%%%%%%%%%%%%%%%READ IV Curve %%%%%%%%%%%%%%%%%%%%%%%%%%%%%%%%%%%%


IV='B11J.xlsx';
A = xlsread(IV);
V=A(:,1);
B = A(:,2);


%%%%%%%%%%%%%%%%%%%%%%%%%%%%%%%%%%%%%%%%%%%%%%%%%%%%%%%%%%%%%%%%%%%%%%%
%%%%%%%%%%%%%%%%%%%%%%%%%%%%%%%%%%%%%%%%%%%%%%%%%%%%%%%%%%%%%%%%%%%%%%%


Is = 9e-7;    %%%%%%% Saturation Current%%%%%
Rs=0.01;      %%%%%%% Series Resistance%%%%%
Rp=220;       %%%%%%% Parallel Resistance%%%%%
Vt=0.026;     %%%%%%% Boltzmann Constant*T(300K)%%%%
n=15;


%%%%%%%%%%%%%%%%%%%%%%%%%%%%%%%%%%%%%%%%%%%%%%%%%%%%%%%%%%%%%%%%%%%%%%%
%%%%%%%%%%%%%%%%%%%%%%%%%%%%%%%%%%%%%%%%%%%%%%%%%%%%%%%%%%%%%%%%%%%%%%%


Is_error=[];
res=[];
%V=-5.4;
for j=1:size(Is,2)
    for i=1:size(V)
        problem.objective  =  @(I)  (I-((V(i)-I*Rs)/Rp)-
(Is(j)*(exp((V(i)-I*Rs)/(n*Vt)))));
```

```
%               problem.objective = @(I) (I-((V(i)/Rp)-
((I*Rs)/Rp)+(V(i)/Rc)-((I*Rs)/Rc))-(Is(j)*(exp((V(i)-
I*Rs)/(n*Vt)))));


        problem.x0 = 1.0;
        problem.solver = 'fzero'; % a required part of
the structure

        problem.options = optimset(@fzero); % default
options

        x = fzero(problem);
        res(i)= x ;
    end
    Is_error(j)=mean((B-res').^2)


    figure (1)
    plot(V,log(res),'LineWidth',2)
    hold on;
    plot(V,log(B),'-g','LineWidth',2)


     figure (2)
    plot(V,res,'LineWidth',2)
    hold on;
    plot(V,B,'-g','LineWidth',2)
    end


fprintf('The final result is ');
res'

%%%%%%%%%%%%%%%%%%%%%%%%%%%%%%%%%%%%%%%%%%%%%%%%%%%%%%%%%%%%%%%%%%%%%%%
%%%%%%%%%%%%%%%%%%%%%%%%%%%%%%%%%%%%%%%%%%%%%%%%%%%%%%%%%%%%%%%%%%%%%%%


% Error analysis for V using formula

err= abs((B-res'));
abs_diff=sum(abs(B-res'));
err_sq=err.^2;
t_no=numel(err);
sum_err_sq=sum(err_sq);
```

```
mse=sum_err_sq/t_no;
mae=abs_diff/numel(err);


%%%%%%%%%%%%%%%%%%%%%%%%%%%%%%%%%%%%%%%%%%%%%%%%%%%%%%%%%%%%%%%%%%%%%%%
%%%%%%%%%%%%%%%%%%%%%%%%%%%%%%%%%%%%%%%%%%%%%%%%%%%%%%%%%%%%%%%%%%%%%%%


% matlab built-in function
%mean square error
msee=mean((B-res').^2)
rmse=sqrt(msee)
%mean absolute error
maee=mean(abs(B-res'))
figure(3)
plot(Is,Is_error)
```

Appendix D

Spectrum Reconstruction Results Using NNLS and TV-Regularized NNLS Algorithms for 1-LED, 2-LED, and 3-LED Test Light Sources

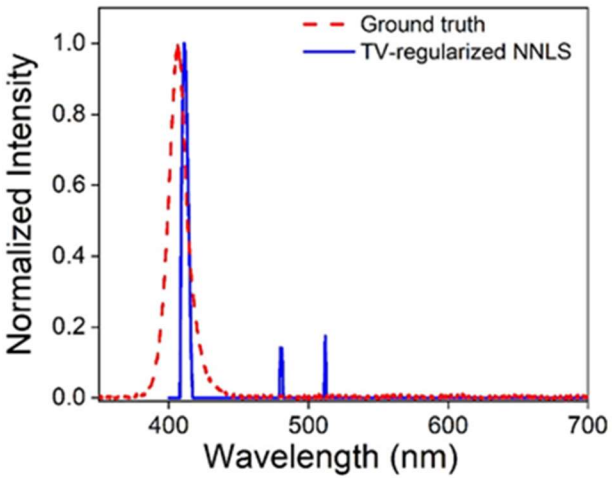

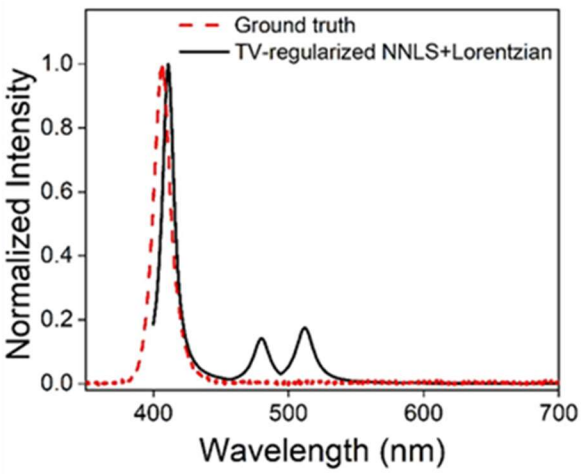

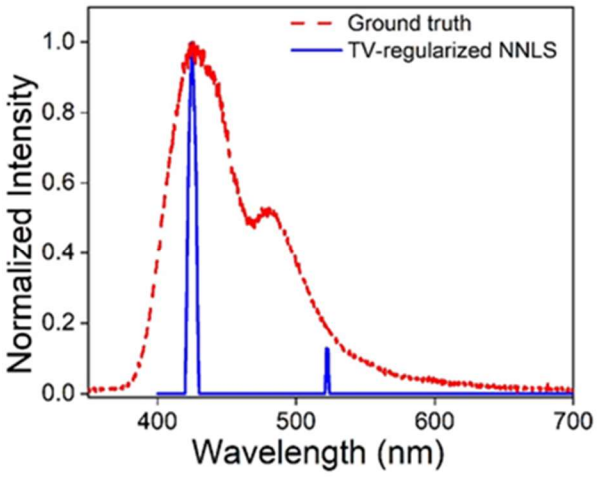

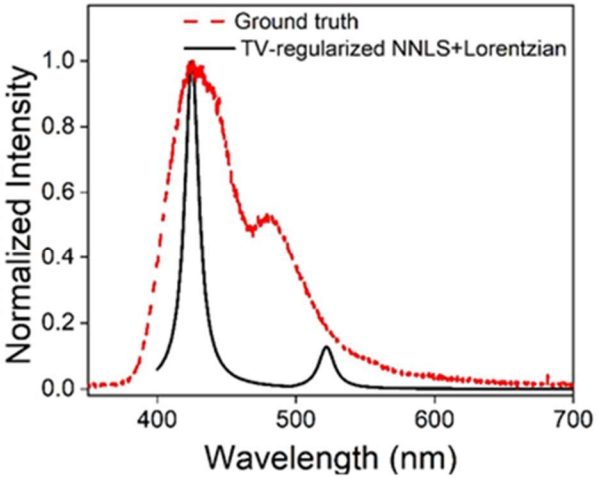

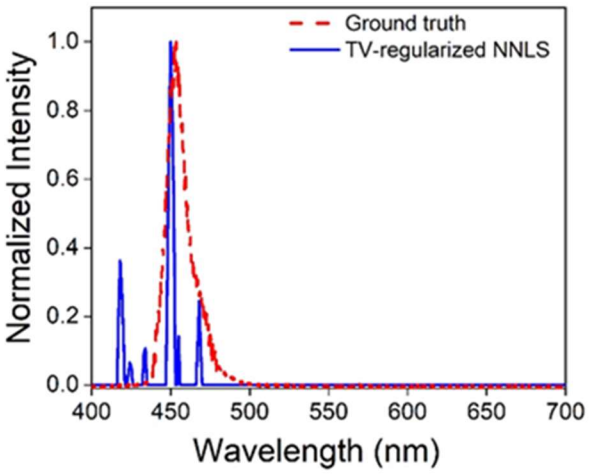
Ground truth
TV-regularized NNLS
Normalized Intensity
Wavelength (nm)

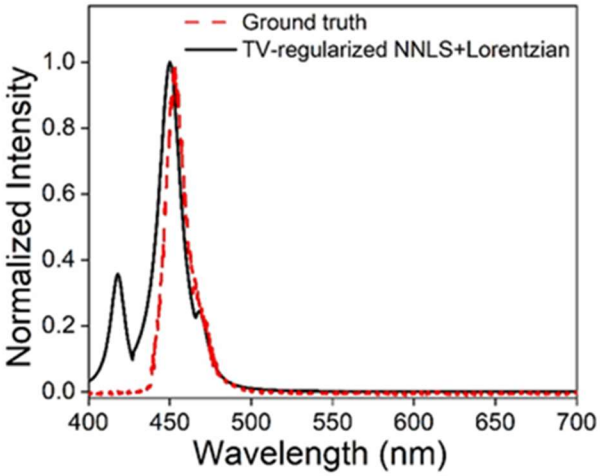
Ground truth
TV-regularized NNLS+Lorentzian
Normalized Intensity
Wavelength (nm)

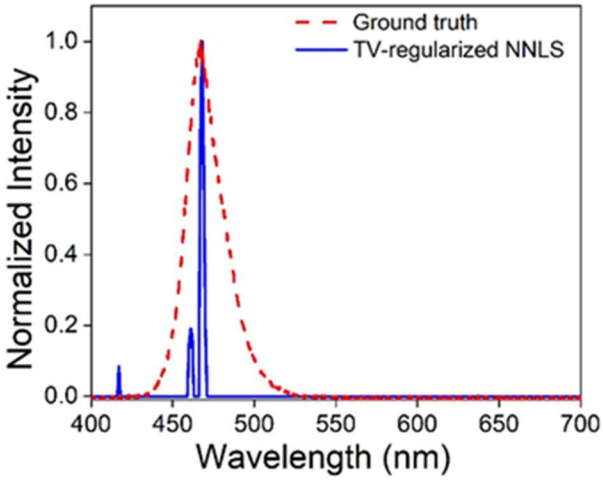
Ground truth
TV-regularized NNLS
Normalized Intensity
Wavelength (nm)

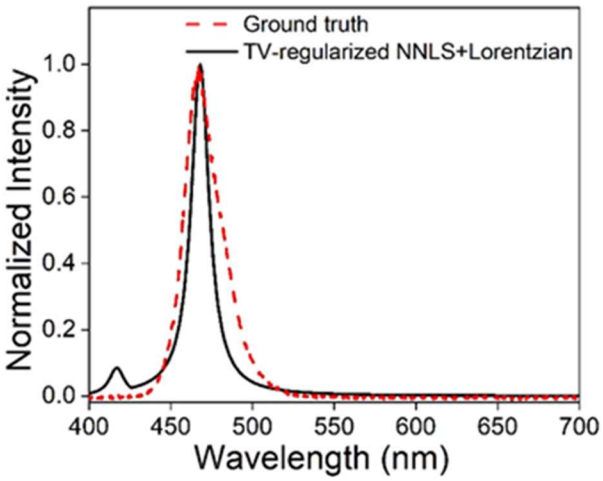
Ground truth
TV-regularized NNLS+Lorentzian
Normalized Intensity
Wavelength (nm)

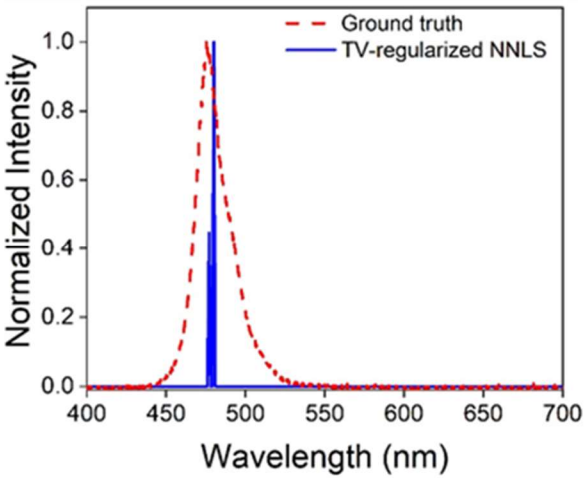
Ground truth
TV-regularized NNLS
Normalized Intensity
Wavelength (nm)

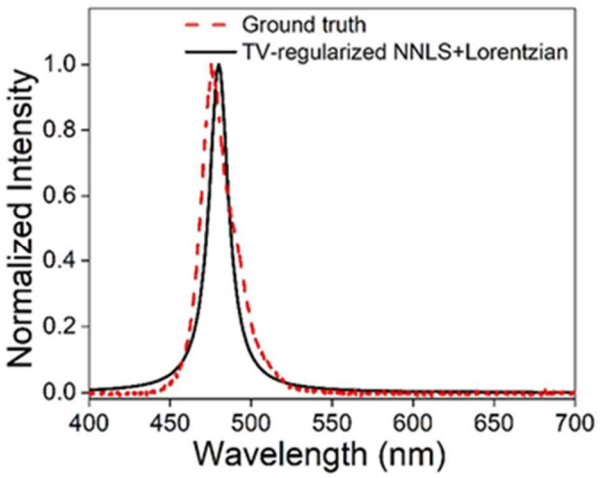
Ground truth
TV-regularized NNLS+Lorentzian
Normalized Intensity
Wavelength (nm)

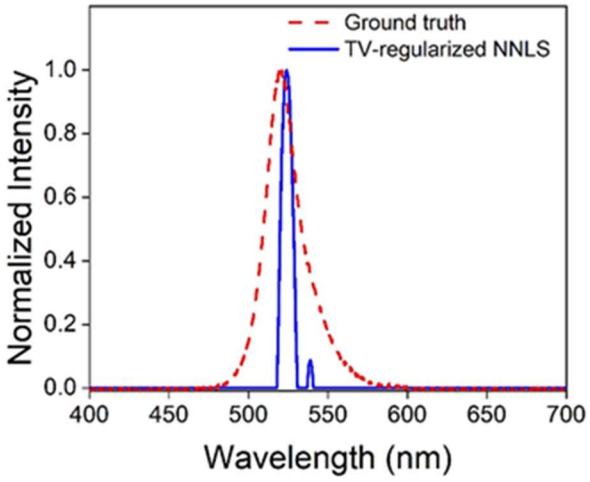
Ground truth
TV-regularized NNLS
Normalized Intensity
Wavelength (nm)

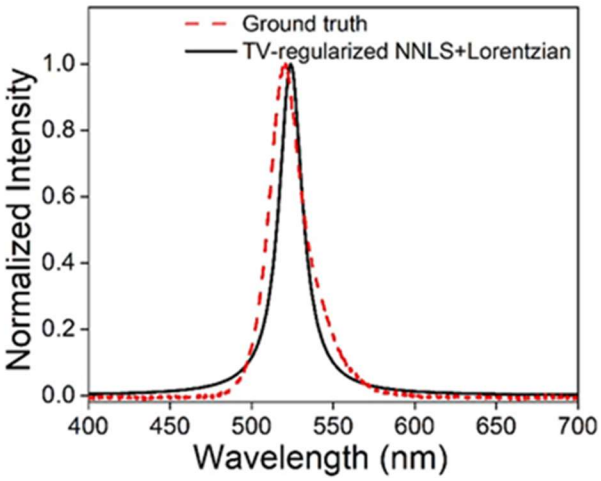
Ground truth
TV-regularized NNLS+Lorentzian
Normalized Intensity
Wavelength (nm)

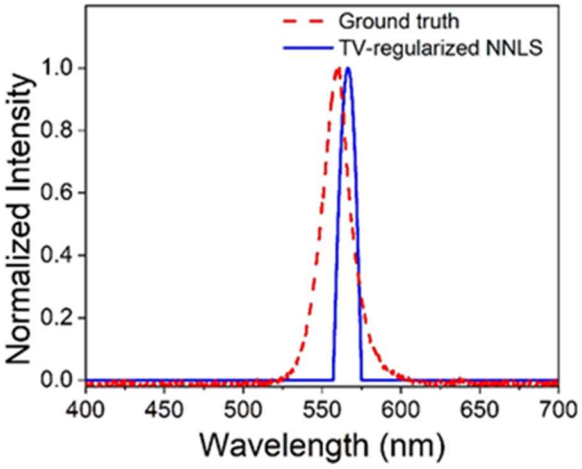
Ground truth
TV-regularized NNLS
Normalized Intensity
Wavelength (nm)

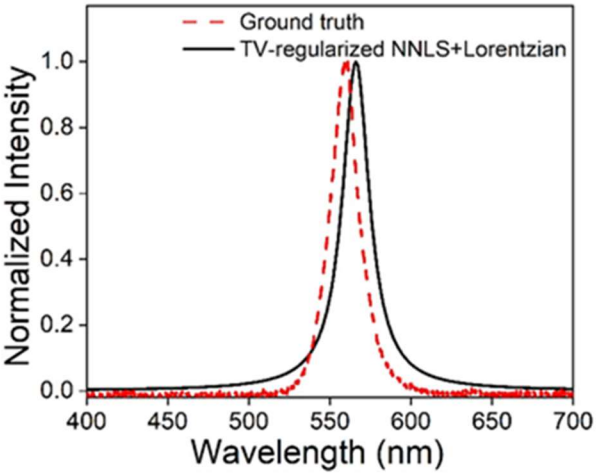
Ground truth
TV-regularized NNLS+Lorentzian
Normalized Intensity
Wavelength (nm)

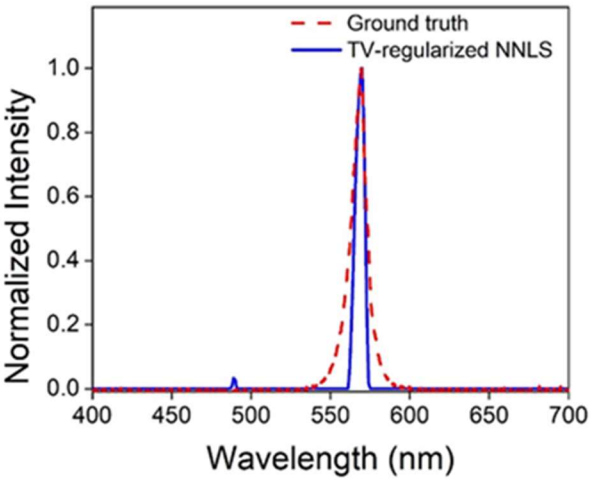
Ground truth
TV-regularized NNLS
Normalized Intensity
Wavelength (nm)

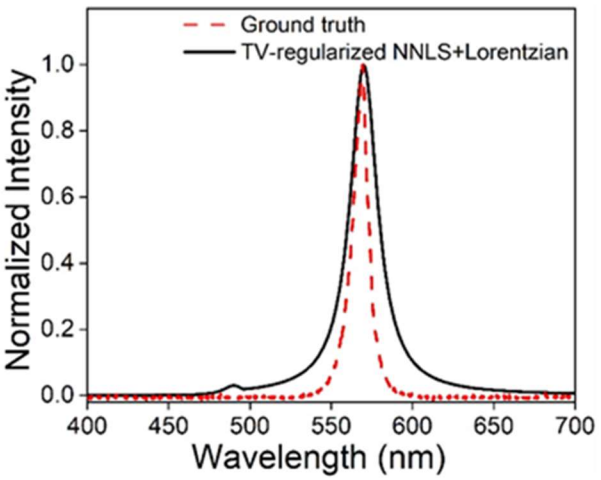
Ground truth
TV-regularized NNLS+Lorentzian
Normalized Intensity
Wavelength (nm)

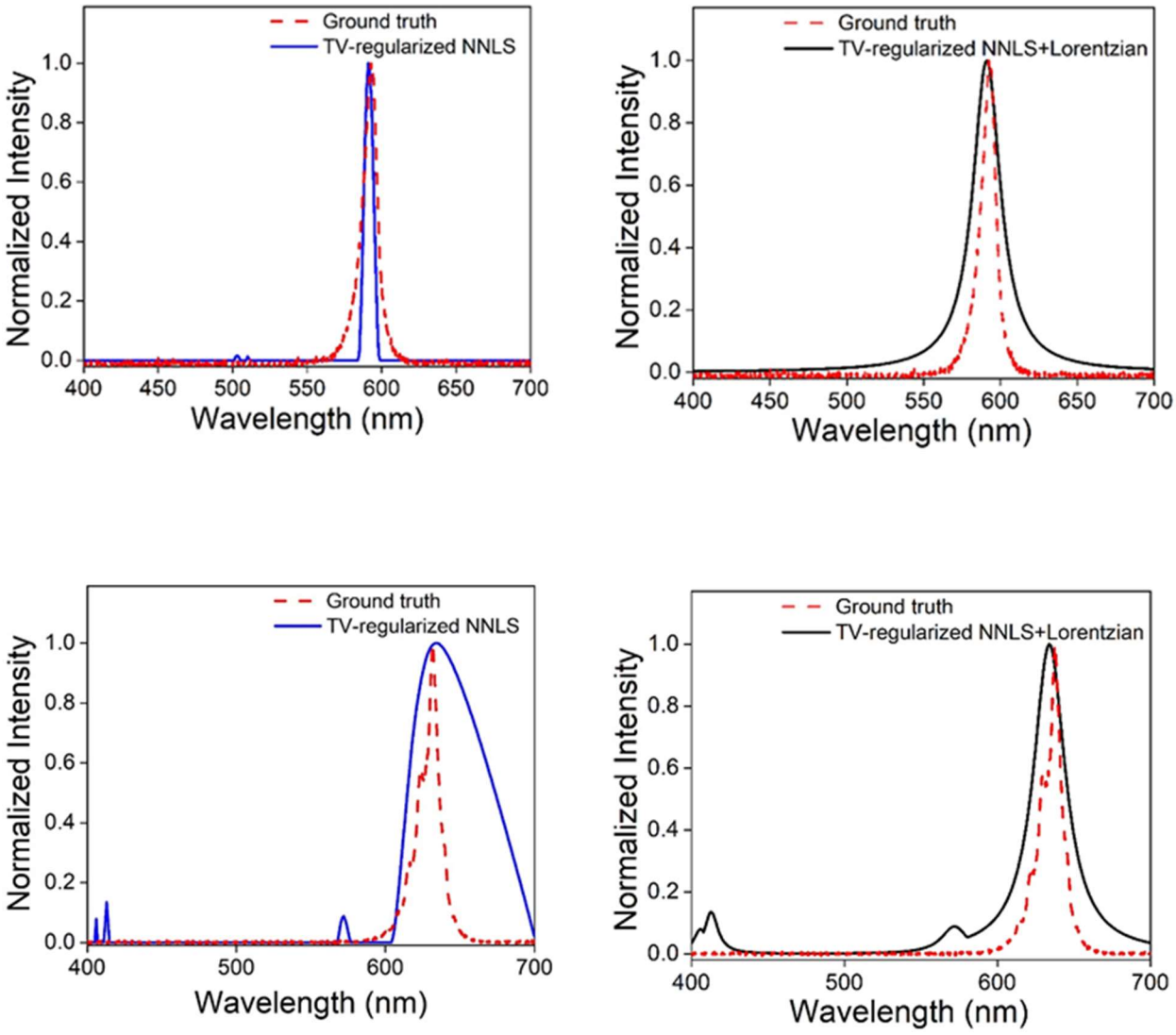

Figure D-1: Spectral reconstruction from the measured photocurrents of 16 photodiodes under the illumination of a 5mm single color LED. In total of 10 different LEDs were used. The spectrum recorded from a commercial spectrometer is also shown as a red dashed line for comparison. The spectra reconstructed via (A-J) TV-regularized NNLS algorithm (solid blue curves) and (K-T) with the addition of an inhomogeneously broadened Lorentzian lineshape with linewidth of $\Delta E = 6kT$ (solid red curves).

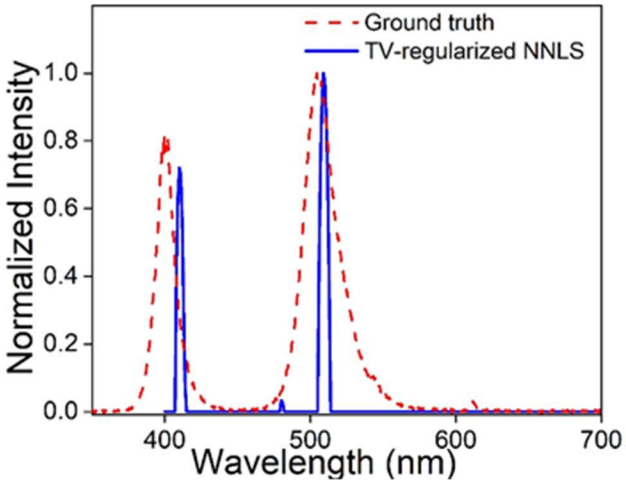
Ground truth
TV-regularized NNLS
Normalized Intensity
Wavelength (nm)

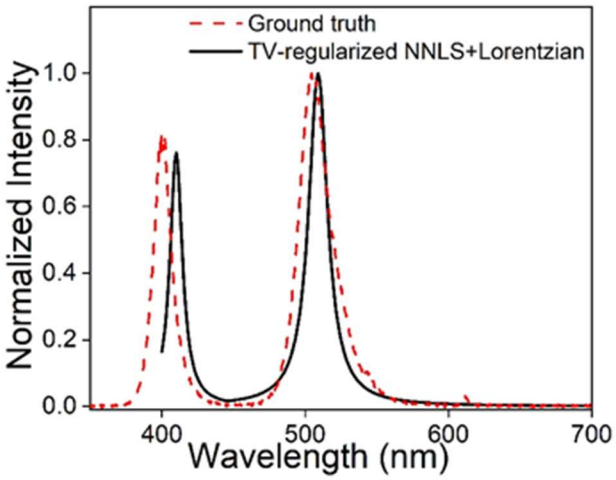
Ground truth
TV-regularized NNLS+Lorentzian
Normalized Intensity
Wavelength (nm)

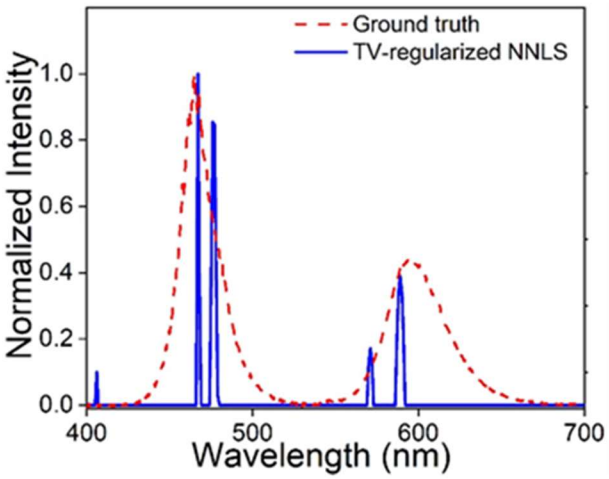
Ground truth
TV-regularized NNLS
Normalized Intensity
Wavelength (nm)

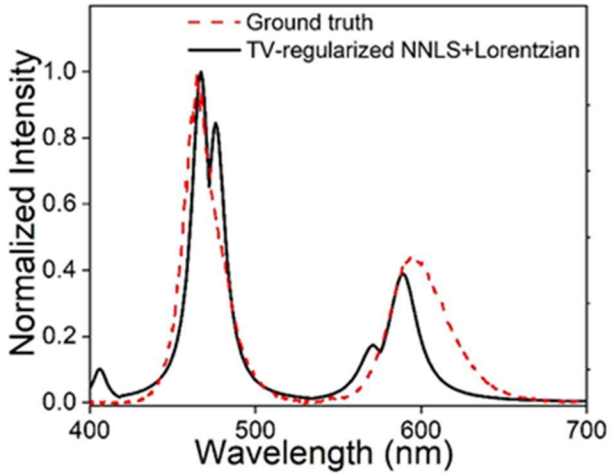
Ground truth
TV-regularized NNLS+Lorentzian
Normalized Intensity
Wavelength (nm)

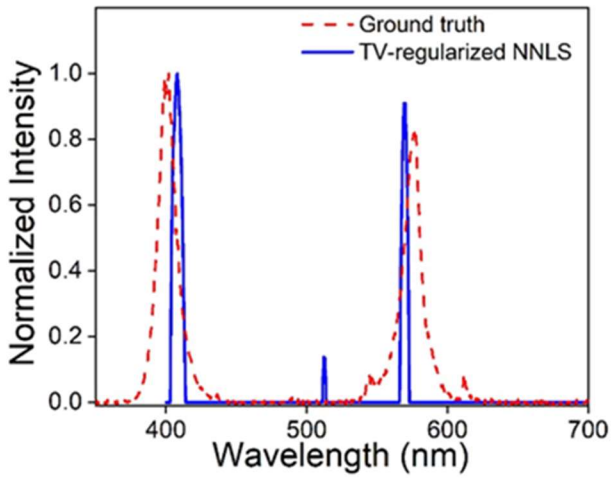
Ground truth
TV-regularized NNLS
Normalized Intensity
Wavelength (nm)

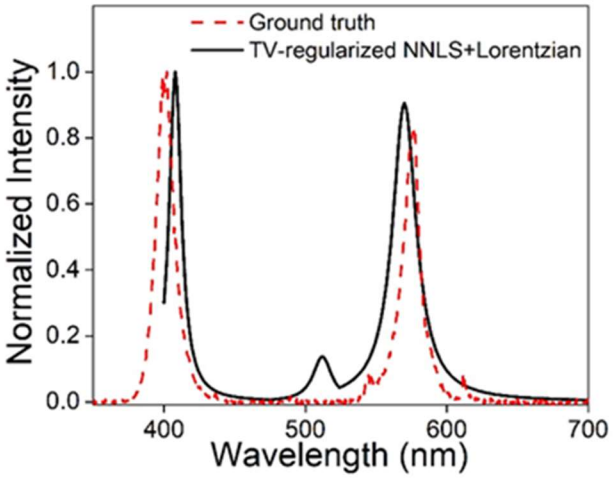
Ground truth
TV-regularized NNLS+Lorentzian
Normalized Intensity
Wavelength (nm)

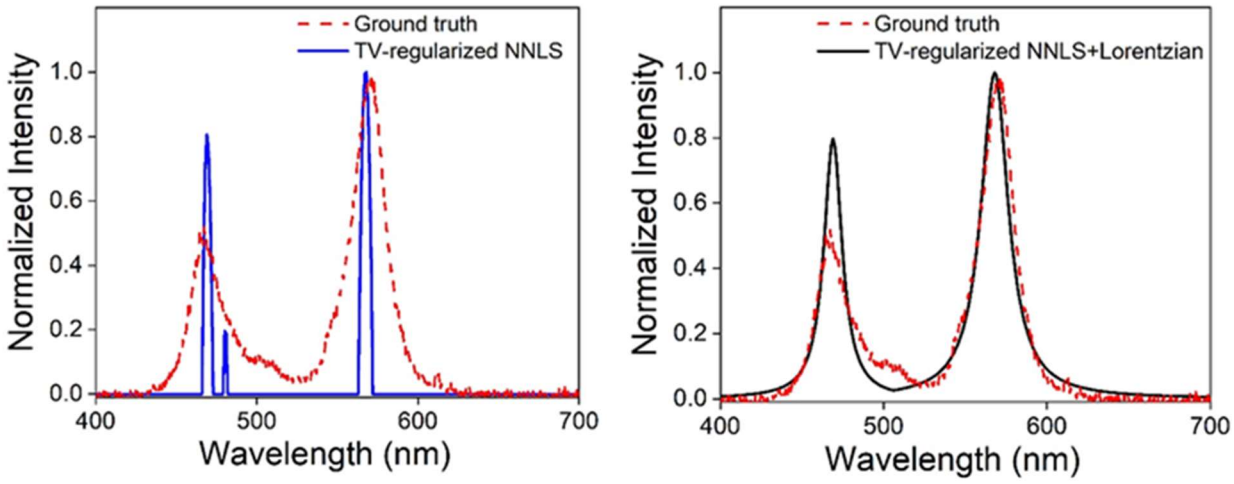

Figure D-2: Spectral reconstruction from the measured photocurrents of 16 photodiodes under the illumination of a test light source comprising of two 5mm LEDs with different peak wavelengths. The spectrum recorded from a commercial spectrometer is also shown as a red dashed line for comparison. The spectra reconstructed via (A-D) TV-regularized NNLS algorithm (solid blue curves) and (E-H) with the addition of an inhomogeneously broadened Lorentzian lineshape with linewidth of $\Delta E = 6kT$ (solid red curves).

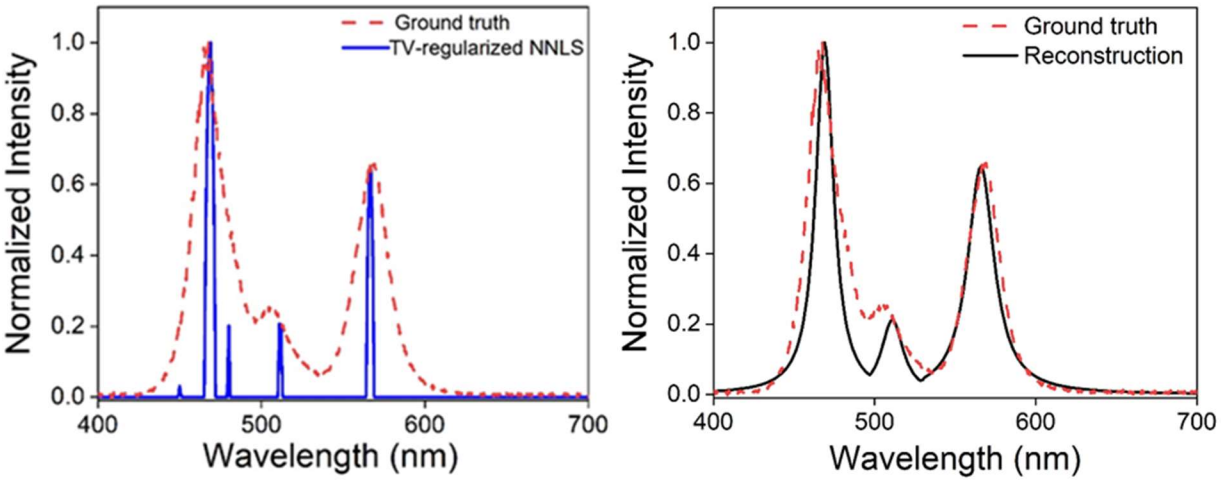

Figure D-3 Spectral reconstruction from the measured photocurrents of 16 photodiodes under the illumination of a test light source comprising of three 5mm LEDs with different peak wavelengths. The spectrum recorded from a commercial spectrometer is also shown as a red dashed line for comparison. The spectra reconstructed via (A) TV-regularized NNLS algorithm (solid blue curves) and (B) with the addition of an inhomogeneously broadened Lorentzian lineshape with linewidth of $\Delta E = 6kT$ (solid red curves).

Bibliography

1. O. T., "Fundamentals of modern UV-visible spectroscopy," Hewlett-Packard Co. 38–61 (1996).

2. B. H. Stuart, *Infrared Spectroscopy: Fundamentals and Applications* (2005).

3. V. P. Iordanov, G. W. Lubking, R. Ishihara, R. F. Wolffenbuttel, P. M. Sarro, and M. J. Vellekoop, "Silicon thin-film UV filter for NADH fluorescence analysis," Sensors Actuators, A Phys. **97**–**98**, 161–166 (2002).

4. R. F. Wolffenbuttel, "State-of-the-art in integrated optical microspectrometers," IEEE Trans. Instrum. Meas. **53**(1), 197–202 (2004).

5. M. B. Wallace, A. Wax, D. N. Roberts, and R. N. Graf, "Reflectance Spectroscopy," Gastrointest. Endosc. Clin. N. Am. **19**(2), 233–242 (2009).

6. R. F. Wolffenbuttel, "State-of-the-Art in Integrated Optical Microspectrometers," IEEE Trans. Instrum. Meas. **53**(1), 197–202 (2004).

7. K. P. Min, J. Kim, K. D. Song, and G. W. Kim, "A G-fresnel optical device and image processing based miniature spectrometer for mechanoluminescence sensor applications," Sensors (Switzerland) **19**(16), (2019).

8. L. Hong, H. Li, H. Yang, and K. Sengupta, "Fully Integrated Fluorescence Biosensors On-Chip Employing Multi-Functional Nanoplasmonic Optical Structures in CMOS," IEEE J. Solid-State Circuits **52**(9), 2388–2406 (2017).

9. L. Bush, *Spectroscopy Solutions for Materials Analysis* (2020).

10. S.-W. Wang, C. Xia, X. Chen, W. Lu, M. Li, H. Wang, W. Zheng, and T. Zhang, "Concept of a high-resolution miniature spectrometer using an integrated filter array," Opt. Lett. **32**(6), 632 (2007).

11. A. Li, C. Yao, J. Xia, H. Wang, Q. Cheng, R. Penty, Y. Fainman, and S. Pan, "Advances in cost-effective integrated spectrometers," Light Sci. Appl. **11**(1), 1–18 (2022).

12. R. A. Crocombe, "Portable Spectroscopy," Appl. Spectrosc. **72**(12), 1701–1751 (2018).

13. I. Avrutsky, K. Chaganti, I. Salakhutdinov, and G. Auner, "Concept of a miniature optical

spectrometer using integrated optical and micro-optical components," Appl. Opt. **45**(30), 7811–7817 (2006).

14. A. Bayram, N. Horzum, A. U. Metin, V. Kilic, and M. E. Solmaz, "Colorimetric Bisphenol-A Detection With a Portable Smartphone-Based Spectrometer," IEEE Sens. J. **18**(14), 5948–5955 (2018).

15. A. Atvars, S. Khudaverdyan, M. Lapkis, and S. Rudenko, "Miniature diode spectrometer design," **11180**(October 2018), 235 (2019).

16. A. B. Shafer, L. R. Megill, and L. Droppleman, "Optimization of the Czerny–Turner Spectrometer*," J. Opt. Soc. Am. **54**(7), 879–887 (1964).

17. L. Gao, Y. Qu, L. Wang, and Z. Yu, "Computational spectrometers enabled by nanophotonics and deep learning," Nanophotonics **11**(11), 2507–2529 (2022).

18. J. J. Cadusch, J. Meng, and K. B. Crozier, "Nanostructured Fishnet Silicon Photodetector Pixels as a Fully-Contained Microspectrometer Chip," 2018 Conf. Lasers Electro-Optics, CLEO 2018 - Proc. 2–3 (2018).

19. C. P. Bacon, Y. Mattley, and R. DeFrece, "Miniature spectroscopic instrumentation: Applications to biology and chemistry," Rev. Sci. Instrum. **75**(1), 1–16 (2004).

20. P. S. Thenkabail and J. G. Lyon, *Hyperspectral Remote Sensing of Vegetation* (CRC Press, 2016).

21. L.-J. Wang, N. Naudé, Y.-C. Chang, A. Crivaro, M. Kamoun, P. Wang, and L. Li, "An ultra-low-cost smartphone octochannel spectrometer for mobile health diagnostics," J. Biophotonics **11**(8), e201700382 (2018).

22. F. Cai, W. Lu, W. Shi, and S. He, "A mobile device-based imaging spectrometer for environmental monitoring by attaching a lightweight small module to a commercial digital camera," Sci. Rep. (2017).

23. K. Hardie, S. Agne, K. B. Kuntz, and T. Jennewein, "Inexpensive LED-Based Optical Coating Sensor," IEEE Sens. J. **17**(19), 6224–6231 (2017).

24. K. M. G. de Lima, "A portable photometer based on LED for the determination of aromatic hydrocarbons in water," Microchem. J. **103**, 62–67 (2012).

25. F. A. A. Nugroho, I. Darmadi, L. Cusinato, A. Susarrey-Arce, H. Schreuders, L. J. Bannenberg, A. B. da Silva Fanta, S. Kadkhodazadeh, J. B. Wagner, T. J. Antosiewicz, A. Hellman, V. P. Zhdanov, B. Dam, and C. Langhammer, "Metal–polymer hybrid nanomaterials for plasmonic ultrafast hydrogen detection," Nat. Mater. **18**(5), 489–495 (2019).

26. OceanOptics, "Water Quality Monitoring: Chlorophyll a and Suspended Solids," https://oceanoptics.com/wp-content/uploads/OceanView_Water-Quality-Monitoring.pdf.

27. R. Cheng, C.-L. Zou, X. Guo, S. Wang, X. Han, and H. X. Tang, "Broadband on-chip single-photon spectrometer," Nat. Commun. **10**(1), 4104 (2019).

28. H. Tan, J. J. Cadusch, B. Li, and K. B. Crozier, "Smartphone-based Optical Fiber Speckle Spectrometer," SM2L.2 (2020).

29. J. Kim, S. Cheekati, T. Sarwar, and P. Ku, "Designing an Ultrathin Film Spectrometer Based on III-Nitride Light-Absorbing Nanostructures," Micromachines **12**(7), 760 (2021).

30. T. Sarwar, S. Cheekati, K. Chung, and P. C. Ku, "On-chip optical spectrometer based on GaN wavelength-selective nanostructural absorbers," Appl. Phys. Lett. **116**(8), (2020).

31. J. Bao and M. G. Bawendi, "A colloidal quantum dot spectrometer," Nature **523**(7558), 67–70 (2015).

32. D. M. Kita, B. Miranda, D. Favela, D. Bono, J. Michon, H. Lin, T. Gu, and J. Hu, "High-performance and scalable on-chip digital Fourier transform spectroscopy," Nat. Commun. **9**(1), 1–7 (2018).

33. J. Meng, J. J. Cadusch, and K. B. Crozier, "Plasmonic Mid-Infrared Filter Array-Detector Array Chemical Classifier Based on Machine Learning," ACS Photonics **8**(2), 648–657 (2021).

34. K. Seo, M. Wober, P. Steinvurzel, E. Schonbrun, Y. Dan, T. Ellenbogen, and K. B. Crozier, "Multicolored vertical silicon nanowires," Nano Lett. **11**(4), 1851–1856 (2011).

35. B. J. Craig, J. Meng, V. R. Shrestha, J. J. Cadusch, and K. B. Crozier, "Mid- to long-wave infrared computational spectroscopy using a subwavelength coaxial aperture array," Sci. Rep. **9**(1), 1–11 (2019).

36. L. Hong, X. Lu, and K. Sengupta, "Nano-optical systems in CMOS," in *Midwest Symposium on Circuits and Systems* (Institute of Electrical and Electronics Engineers Inc., 2017), **2017-Augus**, pp. 906–909.

37. T. Li and Y. Shi, "A Spectrometer as Simple as a CCD Detector," (2017).

38. F. A. A. Nugroho, I. Darmadi, L. Cusinato, A. Susarrey-Arce, H. Schreuders, L. J. Bannenberg, A. B. da Silva Fanta, S. Kadkhodazadeh, J. B. Wagner, T. J. Antosiewicz, A. Hellman, V. P. Zhdanov, B. Dam, and C. Langhammer, "Metal–polymer hybrid nanomaterials for plasmonic ultrafast hydrogen detection," Nat. Mater. **18**(5), 489–495 (2019).

39. C. Z. N. Peidong Yang, L. Dou, and P. Yang, "Bandgap engineering in semiconductor alloy nanomaterials with widely tunable compositions," Nat. Rev. Mater. **2**, (2017).

40. E. Laux, C. Genet, T. Skauli, and T. W. Ebbesen, "Plasmonic photon sorters for spectral and polarimetric imaging," Nat. Photonics **2**(3), 161–164 (2008).

41. P. Guyot-Sionnest, M. M. Ackerman, and X. Tang, "Colloidal quantum dots for infrared detection beyond silicon," J. Chem. Phys. **151**(6), 060901 (2019).

42. Z. Wang, S. Yi, A. Chen, M. Zhou, T. S. Luk, A. James, J. Nogan, W. Ross, G. Joe, A. Shahsafi, K. X. Wang, M. A. Kats, and Z. Yu, "Single-shot on-chip spectral sensors based on photonic crystal slabs," Nat. Commun. **10**(1), 1020 (2019).

43. Z. Yang, T. Albrow-owen, H. Cui, J. Alexander-webber, F. Gu, X. Wang, T. Wu, M. Zhuge, C. Williams, P. Wang, A. V Zayats, W. Cai, L. Dai, S. Hofmann, M. Overend, L. Tong, Q. Yang, Z. Sun, and T. Hasan, "Single-nanowire spectrometers," **1020**(September), 1017–1020 (2019).

44. U. Kurokawa, B. Il Choi, and C. C. Chang, "Filter-based miniature spectrometers: Spectrum reconstruction using adaptive regularization," IEEE Sens. J. **11**(7), 1556–1563 (2011).

45. E. Huang, Q. Ma, and Z. Liu, "Spectrum Engineering for Reconstructive Spectrometry," in (The Optical Society, 2016), p. AM1J.7.

46. T. Sarwar, C. Yaras, X. Li, Q. Qu, and P.-C. Ku, "Miniaturizing a Chip-Scale Spectrometer Using Local Strain Engineering and Total-Variation Regularized Reconstruction," Nano Lett. **22**(20), 8174–8180 (2022).

47. T. Sarwar, J. Kim, and P.-C. Ku, "Optics-Free Optical Spectrometer Chip for the Visible Wavelengths," in *Conference on Lasers and Electro-Optics*, Technical Digest Series (Optica Publishing Group, 2022), p. AW4C.4.

48. T. Sarwar, J. Kim, S. Cheekati, and P.-C. Ku, "Ultracompact Optics-Free Chip-Scale Spectrometer with Integrated LEDs," in *Conference on Lasers and Electro-Optics*, J. Kang Tomasulo, S., Ilev, I., Müller, D., Litchinitser, N., Polyakov, S., Podolskiy, V., Nunn, J., Dorrer, C., Fortier, T., Gan, Q., and Saraceno, C., ed., OSA Technical Digest (Optica Publishing Group, 2021), p. STh1H.4.

49. U. Kurokawa, B. Il Choi, and C. C. Chang, "Filter-based miniature spectrometers: Spectrum reconstruction using adaptive regularization," IEEE Sens. J. **11**(7), 1556–1563 (2011).

50. B. I. Akca, "Design of a compact and ultrahigh-resolution Fourier-transform spectrometer," Opt. Express **25**(2), 1487 (2017).

51. H. Podmore, A. Scott, P. Cheben, A. V. Velasco, J. H. Schmid, M. Vachon, and R. Lee, "A compressive-sensing Fourier-transform spectrometer chip using subwavelength grating waveguides," Opt. Lett. 1–4 (2017).

52. W. Hartmann, P. Varytis, H. Gehring, N. Walter, F. Beutel, K. Busch, and W. Pernice, "Waveguide-Integrated Broadband Spectrometer Based on Tailored Disorder," Adv. Opt. Mater. **8**(6), (2020).

53. A. Emadi, H. Wu, G. de Graaf, and R. Wolffenbuttel, "Design and implementation of a sub-nm resolution microspectrometer based on a Linear-Variable Optical Filter," Opt. Express

20(1), 489 (2012).

54. J. P. Carmo, R. P. Rocha, M. Bartek, G. De Graaf, R. F. Wolffenbuttel, and J. H. Correia, "A review of visible-range Fabry-Perot microspectrometers in silicon for the industry," Opt. Laser Technol. **44**(7), 2312–2320 (2012).

55. C. Kim, W.-B. Lee, S. K. Lee, Y. T. Lee, and H.-N. Lee, "Fabrication of 2D thin-film filter-array for compressive sensing spectroscopy," Opt. Lasers Eng. **115**(October 2018), 53–58 (2019).

56. Z. Xia, A. A. Eftekhar, M. Soltani, B. Momeni, Q. Li, M. Chamanzar, S. Yegnanarayanan, and A. Adibi, "High resolution on-chip spectroscopy based on miniaturized microdonut resonators," Opt. Express **19**(13), 12356 (2011).

57. X. Gan, N. Pervez, I. Kymissis, F. Hatami, and D. Englund, "A high-resolution spectrometer based on a compact planar two dimensional photonic crystal cavity array," Appl. Phys. Lett. **100**(23), (2012).

58. E. Heidari, X. Xu, C.-J. Chung, and R. T. Chen, "On-chip Fourier transform spectrometer on silicon-on-sapphire," Opt. Lett. **44**(11), 2883 (2019).

59. B. Redding, S. M. Popoff, and H. Cao, "All-fiber spectrometer based on speckle pattern reconstruction," Opt. Express **21**(5), 6584 (2013).

60. B. Redding, S. F. Liew, R. Sarma, and H. Cao, "Compact spectrometer based on a disordered photonic chip," Nat. Photonics **7**(9), 746–751 (2013).

61. J. Bao and M. G. Bawendi, "A colloidal quantum dot spectrometer," Nature **523**(7558), 67–70 (2015).

62. Z. Wang and Z. Yu, "Spectral analysis based on compressive sensing in nanophotonic structures," Opt. Express **22**(21), 25608 (2014).

63. X. Hu, H. Liu, X. Wang, X. Zhang, Z. Shan, W. Zheng, H. Li, X. Wang, X. Zhu, Y. Jiang, Q. Zhang, X. Zhuang, and A. Pan, "Wavelength Selective Photodetectors Integrated on a Single Composition-Graded Semiconductor Nanowire," Adv. Opt. Mater. **6**(12), 1–8 (2018).

64. Z. Yang, T. Albrow-Owen, H. Cui, J. Alexander-Webber, F. Gu, X. Wang, T. C. Wu, M. Zhuge, C. Williams, P. Wang, A. V. Zayats, W. Cai, L. Dai, S. Hofmann, M. Overend, L. Tong, Q. Yang, Z. Sun, and T. Hasan, "Single-nanowire spectrometers," Science (80-.). **365**(6457), 1017–1020 (2019).

65. H. Park, Y. Dan, K. Seo, Y. J. Yu, P. K. Duane, M. Wober, and K. B. Crozier, "Filter-Free Image Sensor Pixels Comprising Silicon Nanowires with Selective Color Absorption," Nano Lett. **14**(4), 1804–1809 (2014).

66. C. Brown, A. Goncharov, Z. S. Ballard, M. Fordham, A. Clemens, Y. Qiu, Y. Rivenson,

and A. Ozcan, "Neural Network-Based On-Chip Spectroscopy Using a Scalable Plasmonic Encoder," ACS Nano **15**(4), 6305–6315 (2021).

67. S. Zhang, Y. Dong, H. Fu, S.-L. Huang, and L. Zhang, "A Spectral Reconstruction Algorithm of Miniature Spectrometer Based on Sparse Optimization and Dictionary Learning," Sensors **18**(2), 644 (2018).

68. H. Chun, P. Manousiadis, S. Rajbhandari, D. A. Vithanage, G. Faulkner, D. Tsonev, J. J. D. McKendry, S. Videv, E. Xie, E. Gu, M. D. Dawson, H. Haas, G. A. Turnbull, I. D. W. Samuel, and D. C. O'Brien, "Visible light communication using a blue GaN μ LED and fluorescent polymer color converter," IEEE Photonics Technol. Lett. **26**(20), 2035–2038 (2014).

69. H. Le Minh, D. O'Brien, G. Faulkner, L. Zeng, K. Lee, D. Jung, Y. Oh, and E. T. Won, "100-Mb/s NRZ visible light communications using a postequalized white LED," IEEE Photonics Technol. Lett. **21**(15), 1063–1065 (2009).

70. Institute of Electrical and Electronics Engineers., *2016 IEEE International Solid-State Circuits Conference : Digest of Technical Papers : ISSCC : January 2016.* (n.d.).

71. C. C. Chang and H. Y. Lin, "Spectrum reconstruction for on-chip spectrum sensor array using a novel blind nonuniformity correction method," IEEE Sens. J. **12**(8), 2586–2592 (2012).

72. L. Hong and K. Sengupta, "Fully Integrated Optical Spectrometer in Visible and Near-IR in CMOS," IEEE Trans. Biomed. Circuits Syst. **11**(6), 1176–1191 (2017).

73. H. Mukundan, A. S. Anderson, W. K. Grace, K. M. Grace, N. Hartman, J. S. Martinez, and B. I. Swanson, "Waveguide-based biosensors for pathogen detection," Sensors **9**(7), 5783–5809 (2009).

74. N. H. Wan, F. Meng, T. Schröder, R.-J. Shiue, E. H. Chen, and D. Englund, "High-resolution optical spectroscopy using multimode interference in a compact tapered fibre," Nat. Commun. **6**(1), 7762 (2015).

75. A. Li and Y. Fainman, "On-chip spectrometers using stratified waveguide filters," Nat. Commun. **12**(1), 2704 (2021).

76. T. A. Kwa and R. F. Wolffenbuttel, "Integrated grating/detector array fabricated in silicon using micromachining techniques," Sensors Actuators A Phys. **31**(1), 259–266 (1992).

77. T. Yokino, K. Kato, A. Ui, S. Nakata, T. Suzuki, R. Abe, S. Suzuki, Y. Warashina, K. Shibayama, and K. Yamamoto, "Grating-based ultra-compact SWNIR spectral sensor head developed through MOEMS technology," in *Proc.SPIE* (2019), **10931**, p. 1093108.

78. A. Y. Zhu, W.-T. Chen, M. Khorasaninejad, J. Oh, A. Zaidi, I. Mishra, R. C. Devlin, and F. Capasso, "Ultra-compact visible chiral spectrometer with meta-lenses," APL Photonics **2**(3), 36103 (2017).

79. C. Yang, K. Shi, P. Edwards, and Z. Liu, "Demonstration of a PDMS based hybrid grating and Fresnel lens (G-Fresnel) device," Opt. Express **18**(23), 23529–23534 (2010).

80. P. Edwards, C. Zhang, B. Zhang, X. Hong, V. K. Nagarajan, B. Yu, and Z. Liu, "Smartphone based optical spectrometer for diffusive reflectance spectroscopic measurement of hemoglobin.," Sci. Rep. **7**(1), 12224 (2017).

81. C. Zhang, G. Cheng, P. Edwards, M.-D. Zhou, S. Zheng, and Z. Liu, "G-Fresnel smartphone spectrometer.," Lab Chip **16**(2), 246–250 (2016).

82. Y. Wang, G. Zhu, W. Cai, X. Gao, Y. Yang, J. Yuan, Z. Shi, and H. Zhu, "On-chip photonic system using suspended p-n junction InGaN/GaN multiple quantum wells device and multiple waveguides," Appl. Phys. Lett. **108**(16), (2016).

83. S. Khan, D. Newport, and S. Le Calvé, "Gas Detection Using Portable Deep-UV Absorption," Sensors **19**(23), 5210 (2019).

84. S. K. Selvaraja, A. Z. Subramanian, N. Yebo, R. Baets, G. Roelkens, E. Ryckeboer, F. Peyskens, N. Le Thomas, A. Dhakal, and K. Komorowska, "Spectroscopy-on-chip applications of silicon photonics," in *Integrated Optics: Devices, Materials, and Technologies XVII* (2013).

85. Z. Yang, T. Albrow-Owen, W. Cai, and T. Hasan, "Miniaturization of optical spectrometers," Science (80-.). **371**(6528), (2021).

86. J. J. Cadusch, J. Meng, B. J. Craig, V. R. Shrestha, and K. B. Crozier, "Visible to long-wave infrared chip-scale spectrometers based on photodetectors with tailored responsivities and multispectral filters," Nanophotonics **9**(10), 3197–3208 (2020).

87. W. Wang, S. R. Samuelson, J. Chen, and H. Xie, "Miniaturizing Fourier Transform Spectrometer With an Electrothermal Micromirror," IEEE Photonics Technol. Lett. **27**(13), 1418–1421 (2015).

88. K. Wang, J. Li, D. Lu, and Z. Qi, "Algorithmic Enhancement of Spectral Resolution of a Lithium Niobate (LiNbO3) Waveguide-Based Miniature Fourier Transform Spectrometer," Appl. Spectrosc. **70**(10), 1685–1691 (2016).

89. J. Li, D. Lu, and Z. Qi, "Miniature Fourier transform spectrometer based on wavelength dependence of half-wave voltage of a LiNbO3 waveguide interferometer," Opt. Lett. **39**(13), 3923–3926 (2014).

90. S. N. Zheng, J. Zou, H. Cai, J. F. Song, L. K. Chin, P. Y. Liu, Z. P. Lin, D. L. Kwong, and A. Q. Liu, "Microring resonator-assisted Fourier transform spectrometer with enhanced resolution and large bandwidth in single chip solution," Nat. Commun. **10**(1), 2349 (2019).

91. E. le Coarer, S. Blaize, P. Benech, I. Stefanon, A. Morand, G. Lérondel, G. Leblond, P. Kern, J. M. Fedeli, and P. Royer, "Wavelength-scale stationary-wave integrated Fourier-transform spectrometry," Nat. Photonics **1**(8), 473–478 (2007).

92. X. Nie, E. Ryckeboer, G. Roelkens, and R. Baets, "CMOS-compatible broadband co-propagative stationary Fourier transform spectrometer integrated on a silicon nitride photonics platform," Opt. Express **25**(8), A409–A418 (2017).

93. Y. M. Eltagoury, Y. M. Sabry, and D. A. Khalil, "All-Silicon Double-Cavity Fourier-Transform Infrared Spectrometer On-Chip," Adv. Mater. Technol. **4**(10), 1900441 (2019).

94. A. Herrero-Bermello, A. V Velasco, H. Podmore, P. Cheben, J. H. Schmid, S. Janz, M. L. Calvo, D.-X. Xu, A. Scott, and P. Corredera, "Temperature dependence mitigation in stationary Fourier-transform on-chip spectrometers," Opt. Lett. **42**(11), 2239–2242 (2017).

95. O. Manzardo, H. P. Herzig, C. R. Marxer, and N. F. de Rooij, "Miniaturized time-scanning Fourier transform spectrometer based on silicon technology," Opt. Lett. **24**(23), 1705–1707 (1999).

96. T. Sandner, A. Kenda, C. Drabe, H. Schenk, and W. Scherf, "Miniaturized FTIR-spectrometer based on an optical MEMS translatory actuator," in *Proc.SPIE* (2007), **6466**, p. 646602.

97. U. Wallrabe, C. Solf, J. Mohr, and J. G. Korvink, "Miniaturized Fourier Transform Spectrometer for the near infrared wavelength regime incorporating an electromagnetic linear actuator," Sensors Actuators A Phys. **123**–**124**, 459–467 (2005).

98. M. Erfan, Y. M. Sabry, M. Sakr, B. Mortada, M. Medhat, and D. Khalil, "On-Chip Micro–Electro–Mechanical System Fourier Transform Infrared (MEMS FT-IR) Spectrometer-Based Gas Sensing," Appl. Spectrosc. **70**(5), 897–904 (2016).

99. M. Florjańczyk, P. Cheben, S. Janz, A. Scott, B. Solheim, and D.-X. Xu, "Multiaperture planar waveguide spectrometer formed by arrayed Mach-Zehnder interferometers," Opt. Express **15**(26), 18176–18189 (2007).

100. H. Podmore, A. Scott, P. Cheben, A. V Velasco, J. H. Schmid, M. Vachon, and R. Lee, "Demonstration of a compressive-sensing Fourier-transform on-chip spectrometer," Opt. Lett. **42**(7), 1440–1443 (2017).

101. A. V Velasco, P. Cheben, P. J. Bock, A. Delâge, J. H. Schmid, J. Lapointe, S. Janz, M. L. Calvo, D.-X. Xu, M. Florjańczyk, and M. Vachon, "High-resolution Fourier-transform spectrometer chip with microphotonic silicon spiral waveguides," Opt. Lett. **38**(5), 706–708 (2013).

102. J. P. Carmo, R. P. Rocha, M. Bartek, G. de Graaf, R. F. Wolffenbuttel, and J. H. Correia, "A review of visible-range Fabry–Perot microspectrometers in silicon for the industry," Opt. Laser Technol. **44**(7), 2312–2320 (2012).

103. J. Antila, A. Miranto, J. Mäkynen, M. Laamanen, A. Rissanen, M. Blomberg, H. Saari, and J. Malinen, "MEMS and piezo actuator-based Fabry-Perot interferometer technologies and applications at VTT," in *Proc.SPIE* (2010), **7680**, p. 76800U.

104. J. H. Jerman, D. J. Clift, and S. R. Mallinson, "A miniature Fabry-Perot interferometer with a corrugated silicon diaphragm support," Sensors Actuators A Phys. **29**(2), 151–158 (1991).

105. P. M. Zavracky and E. Hennenberg, "Miniature Fabry Perot spectrometers using micromachining technology," in *Proceedings of WESCON'95* (1995), p. 325.

106. A. Nitkowski, L. Chen, and M. Lipson, "Cavity-enhanced on-chip absorption spectroscopy using microring resonators," Opt. Express **16**(16), 11930–11936 (2008).

107. S. R. Mallinson and J. H. Jerman, "Miniature micromachined Fabry-Perot interferometers in silicon," Electron. Lett. **23**(20), 1041–1043 (1987).

108. A. Ingman, "The Head Up Display Concept," Lund Univ. Sch. Aviat. Maret (2005).

109. H. S. Wasisto, J. D. Prades, J. Gülink, and A. Waag, "Beyond solid-state lighting: Miniaturization, hybrid integration, and applications of GaN nano-and micro-LEDs," Appl. Phys. Rev. **6**(4), (2019).

110. D. Tsonev, H. Chun, S. Rajbhandari, J. J. D. McKendry, S. Videv, E. Gu, M. Haji, S. Watson, A. E. Kelly, G. Faulkner, M. D. Dawson, H. Haas, and D. O'Brien, "A 3-Gb/s single-LED OFDM-based wireless VLC link using a gallium nitride μ LED," IEEE Photonics Technol. Lett. **26**(7), 637–640 (2014).

111. J. J. D. McKendry, R. P. Green, A. E. Kelly, Z. Gong, B. Guilhabert, D. Massoubre, E. Gu, and M. D. Dawson, "High-speed visible light communications using individual pixels in a micro light-emitting diode array," IEEE Photonics Technol. Lett. **22**(18), 1346–1348 (2010).

112. A. L. Washburn and R. C. Bailey, "Photonics-on-a-chip: Recent advances in integrated waveguides as enabling detection elements for real-world, lab-on-a-chip biosensing applications," Analyst **136**(2), 227–236 (2011).

113. Q. Pian, R. Yao, N. Sinsuebphon, and X. Intes, "Compressive hyperspectral time-resolved wide-field fluorescence lifetime imaging," Nat. Photonics **11**(7), 411–414 (2017).

114. K. Chung, J. Sui, B. Demory, and P. C. Ku, "Color mixing from monolithically integrated InGaN-based light-emitting diodes by local strain engineering," Appl. Phys. Lett. (2017).

115. K. Chung, J. Sui, T. Sarwar, and P.-C. Ku, "Feasibility study of nanopillar LED array for color-tunable lighting and beyond," Opt. Express **27**(26), 38229 (2019).

116. L. Zhang, L. K. Lee, C.-H. Teng, T. Hill, P.-C. Ku, and H. Deng, "How much better are InGaN/GaN nanodisks than quantum wells - oscillator strength enhancement and changes in optical properties," Appl. Phys. Lett. **104**(5), 51116 (2014).

117. C. Böcklin, R. G. Veprek, S. Steiger, and B. Witzigmann, "Computational study of an InGaN/GaN nanocolumn light-emitting diode," Phys. Rev. B - Condens. Matter Mater. Phys. **81**(15), 1–9 (2010).

118. Y.-J. J. Lu, H.-W. W. Lin, H.-Y. Y. Chen, Y.-C. C. Yang, and S. Gwo, "Single InGaN nanodisk light emitting diodes as full-color subwavelength light sources," Appl. Phys. Lett. **98**(23), 96–99 (2011).

119. C.-H. Teng, L. Zhang, H. Deng, and P.-C. Ku, "Strain-induced red-green-blue wavelength tuning in InGaN quantum wells," Appl. Phys. Lett. **108**(7), 071104 (2016).

120. K. Chung, J. Sui, B. Demory, and P.-C. Ku, "Color mixing from monolithically integrated InGaN-based light-emitting diodes by local strain engineering," Appl. Phys. Lett. **111**(4), 041101 (2017).

121. K. Chung, J. Sui, B. Demory, C. H. Teng, and P. C. Ku, "Monolithic integration of individually addressable light-emitting diode color pixels," Appl. Phys. Lett. (2017).

122. V. Ramesh, A. Kikuchi, K. Kishino, M. Funato, and Y. Kawakami, "Strain relaxation effect by nanotexturing InGaN/GaN multiple quantum well," J. Appl. Phys. **107**(11), 114303 (2010).

123. J. Meng, J. J. Cadusch, and K. B. Crozier, "Vertically stacked silicon nanowire photodetectors for spectral reconstruction," in *Conference of Laser and Electro-Optics* (2019).

124. S. H. Kong, D. D. L. Wijngaards, and R. F. Wolffenbuttel, "Infrared micro-spectrometer based on a diffraction grating," Sensors Actuators, A Phys. **92**(1–3), 88–95 (2001).

125. E. Ç. Seymour, D. S. Freedman, M. Gökkavas, E. Özbay, M. Sahin, and M. Selim Ünlü, "Improved selectivity from a wavelength addressable device for wireless stimulation of neural tissue," Front. Neuroeng. **7**(FEB), 1–12 (2014).

126. C. P. Bacon, Y. Mattley, and R. DeFrece, "Miniature spectroscopic instrumentation: Applications to biology and chemistry," Rev. Sci. Instrum. **75**(1), 1–16 (2004).

127. C. De Santi, M. Meneghini, A. Tibaldi, M. Vallone, M. Goano, F. Bertazzi, G. Verzellesi, G. Meneghesso, and E. Zanoni, *Physical Mechanisms Limiting the Performance and the Reliability of GaN-Based LEDs* (Elsevier Ltd, 2018).

128. R. A. Miller, H. So, T. A. Heuser, and D. G. Senesky, "High-temperature Ultraviolet Photodetectors: A Review.," arXiv Appl. Phys. 1–41 (2018).

129. P. Ray and A. J. Steckl, "Label-Free Optical Detection of Multiple Biomarkers in Sweat, Plasma, Urine, and Saliva," ACS Sensors **4**(5), 1346–1357 (2019).

130. F. Pena-Pereira, I. Costas-Mora, V. Romero, I. Lavilla, and C. Bendicho, "Advances in miniaturized UV-Vis spectrometric systems," TrAC Trends Anal. Chem. **30**(10), 1637–1648 (2011).

131. J. Torrent and V. Barrón, *Diffuse Reflectance Spectroscopy* (2008).

132. T. Adão, J. Hruška, L. Pádua, J. Bessa, E. Peres, R. Morais, and J. J. Sousa, "Hyperspectral imaging: A review on UAV-based sensors, data processing and applications for agriculture and forestry," Remote Sens. (2017).

133. J. Wizenty, T. Schumann, D. Theil, M. Stockmann, J. Pratschke, F. Tacke, F. Aigner, and T. Wuensch, "Recent advances and the potential for clinical use of autofluorescence detection of extra-ophthalmic tissues," Molecules **25**(9), 1–33 (2020).

134. G. Lu and B. Fei, "Medical hyperspectral imaging: a review," J. Biomed. Opt. **19**(1), 010901 (2014).

135. C. M. Lochner, Y. Khan, A. Pierre, and A. C. Arias, "All-organic optoelectronic sensor for pulse oximetry," Nat. Commun. **5**, 1–7 (2014).

136. Y. Khan, D. Han, A. Pierre, J. Ting, X. Wang, C. M. Lochner, G. Bovo, N. Yaacobi-Gross, C. Newsome, R. Wilson, and A. C. Arias, "A flexible organic reflectance oximeter array," Proc. Natl. Acad. Sci. **115**(47), E11015–E11024 (2018).

137. K. R. Koh, T. C. Wood, R. D. Goldin, G.-Z. Yang, D. S. Elson, K. J. Zuzak, S. C. Naik, G. Alexandrakis, D. Hawkins, K. Behbehani, and E. H. Livingston, "Characterization of a near-infrared laparoscopic hyperspectral imaging system for minimally invasive surgery," Anal. Chem. **79**(February 2009), 71691E (2009).

138. J. M. Benavides, S. Chang, S. Y. Park, R. Richards-kortum, and M. Follen, "detection of cervical cancer," **11**(10), 270–277 (2003).

139. S. G. Kong, M. E. Martin, and T. Vo-Dinh, "Hyperspectral fluorescence imaging for mouse skin tumor detection," ETRI J. **28**(6), 770–776 (2006).

140. K. J. Zuzak, S. C. Naik, G. Alexandrakis, D. Hawkins, K. Behbehani, and E. H. Livingston, "Characterization of a near-infrared laparoscopic hyperspectral imaging system for minimally invasive surgery," Anal. Chem. **79**(12), 4709–4715 (2007).

141. R. Pu, P. Gong, D. M. Sherman, T. D. Waite, T. Adão, J. Hruška, L. Pádua, J. Bessa, E. Peres, R. Morais, J. J. Sousa, A. C. Scheinost, and U. Schwertmann, "Color Identification of Iron Oxides and Hydroxysulfates," Am. Mineral. **70**(5), 1463–1471 (1985).

142. J. E. Kreutz, A. Shukhaev, W. Du, S. Druskin, O. Daugulis, and R. F. Ismagilov, "Evolution of catalysts directed by genetic algorithms in a plug-based microfluidic device tested with oxidation of methane by oxygen," J. Am. Chem. Soc. **132**(9), 3128–3132 (2010).

143. Z. Hu, A. Glidle, C. N. Ironside, M. Sorel, M. J. Strain, J. Cooper, and H. Yin, "Integrated microspectrometer for fluorescence based analysis in a microfluidic format," Lab Chip **12**(16), 2850 (2012).

144. A. C. Scheinost and U. Schwertmann, "Color Identification of Iron Oxides and Hydroxysulfates," Soil Sci. Soc. Am. J. **63**(5), 1463–1471 (1999).

145. D. M. Sherman and T. D. Waite, "Electronic spectra of Fe3+ oxides and oxide hydroxides in the near IR to near UV.," Am. Mineral. **70**(11–12), 1262–1269 (1985).

146. A. Aydogan, R. E. Bangle, A. Cadranel, M. D. Turlington, D. T. Conroy, E. Cauët, M. L. Singleton, G. J. Meyer, R. N. Sampaio, B. Elias, and L. Troian-Gautier, "Accessing Photoredox Transformations with an Iron(III) Photosensitizer and Green Light," J. Am. Chem. Soc. **143**(38), 15661–15673 (2021).

147. R. G. J. Strens and B. J. Wood, "Diffuse reflectance spectra and optical properties of some iron and titanium oxides and oxyhydroxides," Mineral. Mag. **43**(327), 347–354 (1979).

148. J. F. Bell, H. Y. Mcsween, J. A. Crisp, R. V. Morris, S. L. Murchie, N. T. Bridges, J. R. Johnson, D. T. Britt, M. P. Golombek, H. J. Moore, A. Ghosh, J. L. Bishop, R. C. Anderson, J. Brückner, T. Economou, J. P. Greenwood, H. P. Gunnlaugsson, R. M. Hargraves, S. Hviid, J. M. Knudsen, M. B. Madsen, R. Reid, R. Rieder, and L. Soderblom, "Mineralogic and compositional properties of Martian soil and dust: Results from Mars Pathfinder," J. Geophys. Res. Planets **105**(E1), 1721–1755 (2000).

149. R. B. Singer, T. B. McCord, R. N. Clark, J. B. Adams, and R. L. Huguenin, "Mars surface composition from reflectance spectroscopy: a summary.," J. Geophys. Res. **84**(B14), 8415–8426 (1979).

150. G. Polder, G. W. A. M. Van Der Heijden, and I. T. Young, "Spectral image analysis for measuring ripeness of tomatoes," Trans. Am. Soc. Agric. Eng. **45**(4), 1155–1161 (2002).

151. J. Xing, C. Bravo, P. T. Jancsók, H. Ramon, and J. De Baerdemaeker, "Detecting bruises on “Golden Delicious” apples using hyperspectral imaging with multiple wavebands," Biosyst. Eng. **90**(1), 27–36 (2005).

152. K. R. Koh, T. C. Wood, R. D. Goldin, G.-Z. Yang, D. S. Elson, K. J. Zuzak, S. C. Naik, G. Alexandrakis, D. Hawkins, K. Behbehani, E. H. Livingston, S. G. Kong, M. E. Martin, T. Vo-Dinh, J. Wizenty, T. Schumann, D. Theil, M. Stockmann, J. Pratschke, F. Tacke, F. Aigner, T. Wuensch, J. Brier, lia dwi jayanti, R. Lu, Y. Peng, J. Xing, C. Bravo, P. T. Jancsók, H. Ramon, J. De Baerdemaeker, G. Polder, G. W. A. M. Van Der Heijden, and I. T. Young, "Hyperspectral scattering for assessing peach fruit firmness," Biosyst. Eng. **45**(1), 1155–1161 (2006).

153. A. A. Gowen, C. P. O’Donnell, P. J. Cullen, G. Downey, and J. M. Frias, "Hyperspectral imaging - an emerging process analytical tool for food quality and safety control," Trends Food Sci. Technol. (2007).

154. Y. Khan, D. Han, A. Pierre, J. Ting, X. Wang, C. M. Lochner, G. Bovo, N. Yaacobi-Gross, C. Newsome, R. Wilson, and A. C. Arias, "A flexible organic reflectance oximeter array," Proc. Natl. Acad. Sci. **115**(47), E11015–E11024 (2018).

155. B. R. Rae, C. Griffin, J. McKendry, J. M. Girkin, H. X. Zhang, E. Gu, D. Renshaw, E. Charbon, M. D. Dawson, and R. K. Henderson, "CMOS driven micro-pixel LEDs integrated

with single photon avalanche diodes for time resolved fluorescence measurements," J. Phys. D. Appl. Phys. **41**(9), 094011 (2008).

156. C. Huang, H. Zhang, and H. Sun, "Ultraviolet optoelectronic devices based on AlGaN-SiC platform: Towards monolithic photonics integration system," Nano Energy **77**, (2020).

157. H. Zhang, C. Huang, K. Song, H. Yu, C. Xing, D. Wang, Z. Liu, and H. Sun, "Compositionally graded III-nitride alloys: Building blocks for efficient ultraviolet optoelectronics and power electronics," Reports Prog. Phys. **84**(4), (2021).

158. Q. Lyu, H. Jiang, and K. M. Lau, "Monolithic integration of ultraviolet light emitting diodes and photodetectors on a p-GaN/AlGaN/GaN/Si platform," Opt. Express **29**(6), 8358 (2021).

159. J. Wei, Z. Ren, and C. Lee, "Metamaterial technologies for miniaturized infrared spectroscopy: Light sources, sensors, filters, detectors, and integration," J. Appl. Phys. **128**(24), 240901 (2020).

160. L. Bi, J. Hu, P. Jiang, D. H. Kim, G. F. Dionne, L. C. Kimerling, and C. A. Ross, "On-chip optical isolation in monolithically integrated non-reciprocal optical resonators," Nat. Photonics **5**(12), 758–762 (2011).

161. T. Sarwar and P. C. Ku, "Ultrathin Optics-Free Spectrometer with Monolithically Integrated LED Excitation," Micromachines **13**(3), 382 (2022).

162. L. Zhang, C. H. Teng, T. A. Hill, L. K. Lee, P. C. Ku, and H. Deng, "Single photon emission from site-controlled InGaN/GaN quantum dots," Appl. Phys. Lett. **103**(19), 1–6 (2013).

163. S. W. Wang, K. Bin Hong, Y. L. Tsai, C. H. Teng, A. J. Tzou, Y. C. Chu, P. T. Lee, P. C. Ku, C. C. Lin, and H. C. Kuo, "Wavelength tunable InGaN/GaN nano-ring LEDs via nano-sphere lithography," Sci. Rep. **7**(January), 1–7 (2017).

164. L. Zhang, T. A. Hill, C.-H. Teng, B. Demory, P.-C. Ku, and H. Deng, "Carrier dynamics in site- and structure-controlled InGaN/GaN quantum dots," 1–32 (2013).

165. C. M. Jones, C. H. Teng, Q. Yan, P. C. Ku, and E. Kioupakis, "Impact of carrier localization on recombination in InGaN quantum wells and the efficiency of nitride light-emitting diodes: Insights from theory and numerical simulations," Appl. Phys. Lett. **111**(11), 1–14 (2017).

166. L. K. Lee, L. Zhang, H. Deng, and P. C. Ku, "Room-temperature quantum-dot-like luminescence from site-controlled InGaN quantum disks," Appl. Phys. Lett. **99**(26), 1–5 (2011).

167. J. Wang and B. Shim, "Exact Recovery of Sparse Signals Using Orthogonal Matching Pursuit: How Many Iterations Do We Need?," IEEE Trans. Signal Process. **64**(16), 4194–4202 (2016).

168. T. T. Cai and L. Wang, "Orthogonal matching pursuit for sparse signal recovery with noise,"

IEEE Trans. Inf. Theory **57**(7), 4680–4688 (2011).

169. S. K. Sahoo and A. Makur, "Signal recovery from random measurements via extended orthogonal matching pursuit," IEEE Trans. Signal Process. **63**(10), 2572–2581 (2015).

170. *Solving Least Squares Problems - Classics in Applied Mathematics* (Society for Industrial and Applied Mathematics, n.d.).

171. J. Oliver, W. Lee, S. Park, and H.-N. Lee, "Improving resolution of miniature spectrometers by exploiting sparse nature of signals," Opt. Express **20**(3), 2613 (2012).

172. Z. Ren, Z. Zhang, J. Wei, B. Dong, and C. Lee, "Wavelength-multiplexed hook nanoantennas for machine learning enabled mid-infrared spectroscopy," Nat. Commun. **13**(1), 3859 (2022).

173. B. Kim, J. Hwang, J. Yi, D. R. Kim, A. Urbas, Z. Ku, and C. H. Lee, "Replicable Quasi-Three-Dimensional Plasmonic Nanoantennas for Infrared Bandpass Filtering," ACS Appl. Mater. Interfaces **13**(20), 24024–24031 (2021).

174. Y. Ye, J. Zhang, D. Liu, and Y. Yang, "Research on a Spectral Reconstruction Method with Noise Tolerance," Curr. Opt. Photonics **5**(5), 562–575 (2021).

175. M. K. Chen, X. Liu, Y. Sun, and D. P. Tsai, "Artificial Intelligence in Meta-optics," Chem. Rev. **122**(19), 15356–15413 (2022).

176. "Artificial Intelligence Algorithm for Flexible Sensors," in *Flexible Piezoelectric Energy Harvesters and Sensors* (2022), pp. 217–265.

177. H. Zhou, L. Xu, Z. Ren, J. Zhu, and C. Lee, "Machine learning-augmented surface-enhanced spectroscopy toward next-generation molecular diagnostics," Nanoscale Adv. **5**(3), 538–570 (2023).

178. J. J. Cadusch, J. Meng, D. Wen, V. R. Shrestha, and K. B. Crozier, "Compact, Lightweight, and Filter-Free: An All-Si Microspectrometer Chip for Visible Light Spectroscopy," ACS Photonics **9**(2), 474–481 (2022).

179. J. Oliver, W.-B. Lee, and H.-N. Lee, "Filters with random transmittance for improving resolution in filter-array-based spectrometers," Opt. Express **21**(4), 3969–3989 (2013).

180. A. Li, C. Yao, J. Xia, H. Wang, Q. Cheng, R. Penty, Y. Fainman, and S. Pan, "Advances in cost-effective integrated spectrometers," Light Sci. Appl. **11**(1), 174 (2022).

181. R. Stojanovic and D. Karadaglic, "Design of an oximeter based on LED-LED configuration and FPGA technology," Sensors (Switzerland) **13**(1), 574–586 (2013).

182. B. R. Rae, J. Yang, J. McKendry, Z. Gong, D. Renshaw, J. M. Girkin, E. Gu, M. D. Dawson, and R. K. Henderson, "A vertically integrated CMOS microsystem for time-Resolved fluorescence analysis," IEEE Trans. Biomed. Circuits Syst. **4**(6 PART 2), 437–444 (2010).

183. V. Srinivasan, V. K. Pamula, and R. B. Fair, "An integrated digital microfluidic lab-on-a-chip for clinical diagnostics on human physiological fluidsThe Science and Application of Droplets in Microfluidic Devices.Electronic supplementary information (ESI) available: five video clips showing: high-spe," Lab Chip **4**(4), 310 (2004).

184. K. Chung, A. Pandey, T. Sarwar, A. Aiello, Z. Mi, P. Bhattacharya, and P.-C. Ku, "Design Chip-Scale Integration of Tunable Short-Wavelength Photonic Devices," SF1O.4 (2020).

185. K. Chung, A. Pandey, T. Sarwar, A. Aiello, Z. Mi, P. Bhattacharya, and P.-C. Ku, "Design Chip-Scale Integration of Tunable Short-Wavelength Photonic Devices," in *Conference on Lasers and Electro-Optics*, OSA Technical Digest (Optica Publishing Group, 2020), p. SF1O.4.

186. K. Chung, J. Sui, and P.-C. Ku, "Transparent Displays Using Strain-Engineered Nanopillar Light-Emitting Diodes," in *Conference on Lasers and Electro-Optics*, OSA Technical Digest (Optica Publishing Group, 2019), p. STh4O.1.

187. J. Kim, S. Cheekati, T. Sarwar, and P.-C. Ku, "Optics-free ultrathin-film spectrometers based on GaN light absorbers," in *Proc.SPIE* (2021), **11686**, p. 116862O.

188. G. Gamez, "Compressed sensing in spectroscopy for chemical analysis," J. Anal. At. Spectrom. **31**(11), 2165–2174 (2016).

189. S. Ioussoufovitch, D. J. F. Cohen, D. Milej, and M. Diop, "Compressed sensing time-resolved spectrometer for quantification of light absorbers in turbid media.," Biomed. Opt. Express **12**(10), 6442–6460 (2021).

190. A. Asensio Ramos and A. López Ariste, "Compressive sensing for spectroscopy and polarimetry," A&A **509**, (2010).

191. D. J. Starling, I. Storer, and G. A. Howland, "Compressive sensing spectroscopy with a single pixel camera," Appl. Opt. **55**(19), 5198–5202 (2016).

192. V. Nardino, D. Guzzi, C. Lastri, L. Palombi, G. Coluccia, E. Magli, D. Labate, and V. Raimondi, "Compressive Sensing Imaging Spectrometer for UV-Vis Stellar Spectroscopy: Instrumental Concept and Performance Analysis," Sensors **23**(4), (2023).

193. Z. Xing, J. Zhou, Z. Ge, G. Huang, and M. Hu, "Recovery of High Order Statistics of PSK Signals Based on Low-Rank Matrix Completion," IEEE Access **11**, 12973–12986 (2023).

194. H. Gan, M. Shen, Y. Hua, C. Ma, and T. Zhang, "From Patch to Pixel: A Transformer-Based Hierarchical Framework for Compressive Image Sensing," IEEE Trans. Comput. Imaging **9**, 133–146 (2023).

195. H. Li, F. Dai, Q. Zhao, Y. Ma, J. Cao, and Y. Zhang, "Non-uniform Compressive Sensing Imaging Based on Image Saliency," Chinese J. Electron. **32**(1), 159–165 (2023).

196. B. Shi, Y. Wang, and D. Li, "Provable General Bounded Denoisers for Snapshot

Compressive Imaging With Convergence Guarantee," IEEE Trans. Comput. Imaging **9**, 55–69 (2023).

197. T. Sato, "United States Patent : 5861366 United States Patent : 5861366," New York **2**(19), 1–29 (2020).

198. P.-C. Ku, "Chip-scale Integration of RGB LED Pixels for Microdisplay, Lighting and Biophotonics Applications," in *Imaging and Applied Optics 2017 (3D, AIO, COSI, IS, MATH, PcAOP)*, OSA Technical Digest (Online) (Optica Publishing Group, 2017), p. AM3A.2.

199. P.-C. Ku, T. Sarwar, B. Demory, and C.-H. Teng, "Chapter One - Toward scalable III-nitride quantum dot structures for quantum photonics," in *Semiconductor Quantum Science and Technology*, S. T. Cundiff and M. B. T.-S. and S. Kira, eds. (Elsevier, 2020), **105**, pp. 1–27.

200. P. Ku, "(Invited) GaN Optoelectronic Devices Based on Local Strain Engineering," ECS Trans. **98**(5), 415 (2020).

201. T. Sarwar, S. Cheekati, K. Chung, and P.-C. Ku, "On-Chip Optical Spectrometer Based on InGaN/GaN Wavelength-Selective Nanostructural Absorbers," in *Conference on Lasers and Electro-Optics*, OSA Technical Digest (Optica Publishing Group, 2020), p. SM4R.3.

202. S. Birner, T. Zibold, T. Andlauer, T. Kubis, M. Sabathil, A. Trellakis, and P. Vogl, "Nextnano: General purpose 3-D simulations," IEEE Trans. Electron Devices **54**(9), 2137–2142 (2007).

203. S. Birner, T. Zibold, T. Andlauer, T. Kubis, M. Sabathil, A. Trellakis, and P. Vogl, "nextnano: General Purpose 3-D Simulations," Electron Devices, IEEE Trans. **54**, 2137–2142 (2007).

204. M. Refaei, "Modeling and Simulation of III-Nitride-Based Solar Cells using Nextnano ®," (2017).

205. D. J. Paul, "8-band k·p modelling of mid-infrared intersubband absorption in Ge quantum wells," J. Appl. Phys. **120**(4), (2016).

206. G. Giannoccaro, F. de Leonardis, and V. M. N. Passaro, "Modeling of the interminiband absorption coefficient in InGaN quantum dot superlattices," Photonics **3**(1), (2016).

207. S. Naceur, M. Choubani, and H. Maaref, "Linear and nonlinear optical absorption coefficients in wurtzite InGaN/GaN quantum dots switching at 1.55 μm wavelength: Indium segregation and pressure effects," Int. J. Recent Trends Eng. Res. **3**(11), 143–155 (2017).

208. J. Kvietkova, L. Siozade, P. Disseix, A. Vasson, J. Leymarie, B. Damilano, N. Grandjean, and J. Massies, "Optical investigations and absorption coefficient determination of InGaN/GaN quantum wells," Phys. Status Solidi Appl. Res. **190**(1), 135–140 (2002).

209. O. Ambacher, D. Brunner, R. Dimitrov, M. Stutzmann, A. Sohmer, and F. Scholz, "Absorption of InGaN Single Quantum Wells Determined by Photothermal Deflection Spectroscopy," Jpn. J. Appl. Phys. **37**(Part 1, No. 3A), 745–752 (1998).

210. C.-H. Teng, L. Zhang, T. Hill, B. Demory, H. Deng, and P. C. Ku, "Effects of Strain Relaxation on Luminescent Properties of InGaN/GaN Nanorods from 2D to 0D Transition," in *CLEO: 2013*, OSA Technical Digest (Online) (Optica Publishing Group, 2013), p. CF2E.1.

211. C.-H. Teng, L. Zhang, Y.-L. Tsai, C.-C. Lin, H.-C. Kuo, H. Deng, and P. C. Ku, "Monolithically integrated multi-color InGaN/GaN nanopillar light emitting diodes," in *2015 73rd Annual Device Research Conference (DRC)* (2015), p. 161.

212. C.-H. Teng, L. Zhang, T. Hill, B. Demory, H. Deng, and P. C. Ku, "Semiconductor Single-Photon Emitters with Tunable Polarization Output," in *CLEO: 2014*, OSA Technical Digest (Online) (Optica Publishing Group, 2014), p. JTu4A.97.

213. C. Teng, L. Zhang, H. Deng, and P. Ku, "InGaN quantum dots by surface passivation," (March 2013), (2023).

214. G. Li, W. Wang, W. Yang, and Y. Lin, "GaN-based light-emitting diodes on various substrates : a critical review," (2016).

215. X. Yu, Z. Che, J. Zhang, M. Xie, J. Yu, H. Lu, Y. Luo, and Z. Chen, "Double-sided pattern design on patterned sapphire substrate of GaN-based LEDs," in *Numerical Simulation of Optoelectronic Devices, 2014* (2014), pp. 25–26.

216. S.-H. Chao, L.-H. Yeh, R. T. Wu, K. Kawagishi, and S.-C. Hsu, "Novel patterned sapphire substrates for enhancing the efficiency of GaN-based light-emitting diodes," RSC Adv. **10**(28), 16284–16290 (2020).

217. H. Guo, X. Zhang, H. Chen, P. Zhang, H. Liu, H. Chang, W. Zhao, Q. Liao, and Y. Cui, "High performance GaN-based LEDs on patterned sapphire substrate with patterned composite SiO2/Al2O3 passivation layers and TiO2/Al2O3 DBR backside reflector," Opt. Express **21**(18), 21456–21465 (2013).

218. B. Zhang, C. Luo, and Y. Li, "Damage-Free Transfer of GaN-Based Light-Emitting Devices and Reuse of Sapphire Substrate Damage-Free Transfer of GaN-Based Light-Emitting Devices and Reuse of Sapphire Substrate," (2020).

219. C.-H. Teng, L. Zhang, H. Deng, and P.-C. Ku, "Linewidth reduction of site-controlled InGaN quantum dots by surface passivation," in *Proc.SPIE* (2013), **8625**, p. 86252C.

220. J. He, Y. Tao, C. Yang, M. Feng, B. Li, W. Bian, and Y. Chen, *An Approximate Explicit Solution to General Diode Equation* (n.d.).

221. A. Ortiz-Conde, F. J. García Sánchez, and J. Muci, "Exact analytical solutions of the forward non-ideal diode equation with series and shunt parasitic resistances," Solid. State.

Electron. (2000).

222. F. Ghani and M. Duke, "Numerical determination of parasitic resistances of a solar cell using the Lambert W-function," Sol. Energy (2011).

223. F. J. García-Sánchez, D. Lugo-Muñoz, M. A. Pavanello, A. Ortiz-Conde, M. de Souza, and J. Muci, "An explicit multi-exponential model for semiconductor junctions with series and shunt resistances," Microelectron. Reliab. (2011).

224. S. Alialy, H. Tecimer, H. Uslu, and Aa. AltAAndal, "A Comparative Study on Electrical Characteristics of Au/N-Si Schottky Diodes, with and Without Bi-Doped PVA Interfacial Layer in Dark and Under Illumination at Room Temperature," J. Nanomed. Nanotechnol. (2013).

225. X. A. Cao, S. J. Pearton, G. Dang, A. P. Zhang, F. Ren, and J. M. Hove, "GaN N- and P-type Schottky diodes: Effect of dry etch damage," Electron Devices, IEEE Trans. **47**, 1320–1324 (2000).

226. J.-M. Lee, K.-S. Lee, and S.-J. Park, "Removal of dry etch damage in p-type GaN by wet etching of sacrificial oxide layer," J. Vac. Sci. Technol. B Microelectron. Nanom. Struct. **22**(2), 479 (2004).

227. X. A. Cao, A. P. Zhang, G. T. Dang, F. Ren, S. J. Pearton, J. M. van Hove, R. A. Hickman, R. J. Shul, and L. Zhang, "Plasma damage in p-GaN," J. Electron. Mater. **29**(3), 256–261 (2000).

228. H. Sun, M. K. Shakfa, M. M. Muhammed, B. Janjua, K.-H. Li, R. Lin, T. K. Ng, I. S. Roqan, B. S. Ooi, and X. Li, "Surface-Passivated AlGaN Nanowires for Enhanced Luminescence of Ultraviolet Light Emitting Diodes," ACS Photonics **5**(3), 964–970 (2018).

229. M. Biswas, V. Chavan, S. Zhao, Z. Mi, and S. Chakrabarti, "Passivation of Surface States of AlGaN Nanowires Using H3PO4 Treatment To Enhance the Performance of UV-LEDs and Photoanodes," ACS Appl. Nano Mater. **1**(4), 1968–1975 (2018).

230. E. J. Candès, J. Romberg, and T. Tao, "Robust uncertainty principles: Exact signal reconstruction from highly incomplete frequency information," IEEE Trans. Inf. Theory **52**(2), 489–509 (2006).

231. P. Padmanabhan, B. Hancock, S. Nikzad, L. D. Bell, K. Kroep, and E. Charbon, "A hybrid readout solution for GaN-based detectors using CMOS technology," Sensors (Switzerland) **18**(2), 449 (2018).

232. V. K. Pandey and C. M. Tan, "Application of Gallium Nitride Technology in Particle Therapy Imaging," IEEE Trans. Nucl. Sci. **68**(6), 1319–1324 (2021).

233. L. I. Rudin, S. Osher, and E. Fatemi, "Nonlinear total variation based noise removal algorithms," Phys. D Nonlinear Phenom. **60**(1–4), 259–268 (1992).

234. A. N. Tikhonov and V. Y. Arsenin, "Solutions of Ill-Posed Problems," SIAM Rev. **21**(2), 266–267 (1979).

235. D. Bertsimas and M. S. Copenhaver, "Characterization of the equivalence of robustification and regularization in linear and matrix regression," Eur. J. Oper. Res. **270**(3), 931–942 (2018).

236. Q. Zhang, X. Wang, V. Decker, and M. E. Meyerhoff, "Plasticizer-Free Thin-Film Sodium-Selective Optodes Inkjet-Printed on Transparent Plastic for Sweat Analysis," ACS Appl. Mater. Interfaces **12**(23), 25616–25624 (2020).

237. J. Choi, A. J. Bandodkar, J. T. Reeder, T. R. Ray, A. Turnquist, S. B. Kim, N. Nyberg, A. Hourlier-Fargette, J. B. Model, A. J. Aranyosi, S. Xu, R. Ghaffari, and J. A. Rogers, "Soft, skin-integrated multifunctional microfluidic systems for accurate colorimetric analysis of sweat biomarkers and temperature," ACS Sensors **4**(2), 379–388 (2019).

238. J. Choi, R. Ghaffari, L. B. Baker, and J. A. Rogers, "Skin-interfaced systems for sweat collection and analytics," Sci. Adv. **4**(2), eaar3921 (2018).

239. Y. Kim, J. Kim, H. M. Kim, and J. Jang, "Quantum-Dots Photosensor with Wide Bandgap P-Type and N-Type Oxide Semiconductors for High Detectivity and Responsivity," Adv. Mater. Technol. **5**(1), (2020).

240. B.-W. Liang, C.-C. Huang, S.-P. Chao, K.-J. Kao, K. B. Simbulan, Y.-W. Lan, and C.-H. Kuan, "Responsivity and detectivity enhancements by graphene overlay on normal-incident multicolor quantum grid infrared photodetectors," Opt. Express **28**(2), 2456 (2020).

241. S. Veeralingam, L. Durai, P. Yadav, and S. Badhulika, "Record-High Responsivity and Detectivity of a Flexible Deep-Ultraviolet Photodetector Based on Solid State-Assisted Synthesized hBN Nanosheets," ACS Appl. Electron. Mater. **3**(3), 1162–1169 (2021).

242. J. Bullock, W. Yan, V. R. Shresha, Q. Jeangros, N. S. Azar, S. Balendhran, C. Ballif, and K. Crozier, "Spectrally selective mid-wave infrared detection using fabry-pérot cavity enhanced black phosphorus 2d photodiodes," ACS Nano **14**(10), 13645–13651 (2020).

243. Mister rf, "07R01 IF Amplifier/Demodulator Integrated Circuit Motorola GM350 transceiver," https://en.wikipedia.org/wiki/File:071R01.jpg.